

GROWTH AND CHARACTERIZATIONS OF COMPLEX OXIDE THIN FILM
HETEROSTRUCTURES VIA PULSED LASER DEPOSITION

By

KYEONG-WON KIM

A DISSERTATION PRESENTED TO THE GRADUATE SCHOOL
OF THE UNIVERSITY OF FLORIDA IN PARTIAL FULFILLMENT
OF THE REQUIREMENTS FOR THE DEGREE OF
DOCTOR OF PHILOSOPHY

UNIVERSITY OF FLORIDA

2012

© 2012 Kyeong-Won Kim

To my parents

ACKNOWLEDGMENTS

I could not have achieved this accomplishment without help, guidance and love from people around me and I would like to acknowledge their support.

First and foremost, I thank my advisor Dr. David Norton. I am amazed by his range of knowledge and hard work. I just cannot thank him enough for his help and attention. I would like to thank my committee members, Dr. Stephen Pearton, Dr. Brent Gila, Dr. Valentin Craciun, and Dr. Fan Ren, who have helped me with invaluable advice throughout the doctoral research. Also, I would like to thank Dr. Arthur Hebard and his students, Siddhatha Ghosh and Sanal Buvaev, for their helps with the collaboration.

I thank my fellow group members, specifically Dr. Mat Ivill, Dr. Patrick Sadik, Dr. Fernando Lugo, Dr. Joe Cianfrone, Dr. Seonhoo Kim, for their helps in and out of the lab.

I thank my friends, Dr. Inkook Jun, Dr. Myounghwan Oh, and Dr. Sanghyun Eom. Without their support and presence, it should have been much tougher for me to get through all the processes during my doctoral studies. I also thank my colleagues in the department, specifically Sungwook Mhin, Jinhyung Lee, and Hyuksu Han for their help and support.

I thank friends in UF Korean Buddhist group whom I can share the way to live and think. Also I would like to thank the members in UF Korean baseball league whom I have played with.

Finally, I express the most sincere appreciation to my parents and my brother for giving their infinite love and support.

TABLE OF CONTENTS

| | <u>Page</u> |
|---|-------------|
| ACKNOWLEDGMENTS..... | 4 |
| LIST OF TABLES..... | 7 |
| LIST OF FIGURES..... | 8 |
| ABSTRACT | 10 |
| CHAPTER | |
| 1 INTRODUCTION | 12 |
| Double Perovskite Ba ₂ FeMoO ₆ and Superlattices | 12 |
| ZnO for Optoelectronics..... | 13 |
| 2 LITERATURE REVIEW | 15 |
| A ₂ FeMoO ₆ Double Perovskites | 15 |
| Ferroelectric Ba _{1-x} Sr _x TiO ₃ | 17 |
| Multiferroics and Superlattice Approach | 17 |
| p-type Doping in ZnO..... | 19 |
| 3 EXPERIMENTAL DETAILS AND CHARACTERIZATIONS | 27 |
| Target Synthesis..... | 27 |
| Ba ₂ FeMoO ₆ | 27 |
| Ba _{1-x} Sr _x TiO ₃ (x=0, 0.5)..... | 28 |
| Phosphorus Doped ZnO..... | 28 |
| Thin Film Deposition | 28 |
| Substrate Preparation | 29 |
| Ba ₂ FeMoO ₆ , Ba _{1-x} Sr _x TiO ₃ (x=0, 0.5) Thin Films and Hetero-Structures | 30 |
| Phosphorus Doped ZnO Thin Films | 30 |
| Characterization Techniques | 30 |
| X-ray Diffraction (XRD)..... | 30 |
| Atomic Force Microscopy (AFM) and Scanning Electron Microscopy (SEM) ... | 31 |
| Auger Electron Spectroscopy (AES) | 31 |
| Hall Effect and Magnetoresistance..... | 32 |
| Superconducting Quantum Interference Device (SQUID) | 33 |
| 4 MAGNETIC AND MAGNETOTRANSPORT PROPERTIES OF BA ₂ FEMOO ₆ PULSED LASER DEPOSITED THIN FILMS | 41 |
| Introductory Remarks..... | 41 |
| Experimental..... | 42 |

| | |
|--|------------|
| Results and Discussion..... | 43 |
| Summary and Conclusions | 48 |
| 5 THE EFFECTS OF OXYGEN PRESSURE ON THE PROPERTIES OF BA₂FEMOO₆ THIN FILMS GROWN VIA PULSED LASER DEPOSITION | 57 |
| Introductory Remarks..... | 57 |
| Experimental..... | 58 |
| Results and Discussion..... | 59 |
| Summary and Conclusions | 63 |
| 6 STRAIN INDUCED ENHANCEMENT OF MAGNETIZATION IN BA₂FEMOO₆ BASED HETEROSTRUCTURES WITH (BA,SR)TIO₃..... | 72 |
| Introductory Remarks..... | 72 |
| Experimental..... | 73 |
| Results and Discussion..... | 74 |
| Summary and Conclusions | 77 |
| 7 THE EFFECT OF STRUCTUE ON THE PROPERTIES OF BA₂FEMOO₆/BA_{0.5}SR_{0.5}TIO₃ SUPERLATTICES | 85 |
| Introductory Remarks..... | 85 |
| Experimental..... | 86 |
| Results and Discussion..... | 86 |
| Summary and Conclusions | 90 |
| 8 THE EFFECTS OF ZNO BUFFER LAYERS ON THE PROPERTIES OF PHOSPHORUS DOPED ZNO THIN FILMS GROWN ON SAPPHIRE BY PULSED LASER DEPOSITION..... | 99 |
| Introductory Remarks..... | 99 |
| Experimental..... | 100 |
| Results and Discussion..... | 101 |
| Summary and Conclusions | 103 |
| 9 CONCLUSIONS | 110 |
| Ba ₂ FeMoO ₆ Thin Film and Hetero-structures..... | 110 |
| p-type Doping in ZnO Thin Films | 111 |
| LIST OF REFERENCES | 113 |
| BIOGRAPHICAL SKETCH..... | 121 |

LIST OF TABLES

| <u>Table</u> | | <u>Page</u> |
|--------------|--|-------------|
| 2-1 | Saturation magnetization (M_S) at 5K and 295K, Curie temperature (T_C), and room-temperature crystallographic structure as determined from x-ray diffraction of the double perovskite $AA'FeMoO_6$ ($AA' = Ba_2, BaSr, Sr_2, Ca_2$)..... | 23 |
| 5-1 | Compositions of Ba_2FeMoO_6 thin films grown at 700°C under 0.1 and 10 mTorr by Auger Electron Spectroscopy..... | 65 |
| 6-1 | Periodicities of the superlattices calculated from positions of the satellite peaks around (002) peak of Ba_2FeMoO_6 in Figure 6-1E | 79 |
| 7-1 | Periodicities of the superlattices calculated from positions of the satellite peaks around (002) peak of Ba_2FeMoO_6 in Figure 7-1B | 92 |
| 8-1 | Hall transport properties of as-grown and rapid thermal annealed $ZnO:P_{0.001}$ thin films | 105 |

LIST OF FIGURES

| <u>Figure</u> | | <u>Page</u> |
|---------------|--|-------------|
| 2-1 | The crystal structure of YMnO_3 in the paraelectric and ferroelectric phases and schematic of a MnO_5 polyhedron with Y layers above and below. | 24 |
| 2-2 | Multiferroic properties induced by strain from substrate | 25 |
| 2-3 | Stick and ball representation of ZnO crystal structures | 26 |
| 3-1 | XRD patterns of $\text{Ba}_2\text{FeMoO}_6$ powders calcined and sintered..... | 35 |
| 3-2 | Rietveld results of the diffraction data of $\text{Ba}_2\text{FeMoO}_6$ powders from synchrotron source | 36 |
| 3-3 | Crystal structure of $\text{Ba}_2\text{FeMoO}_6$ from (100) direction generated by CrystalMaker using the refinement data | 37 |
| 3-4 | Schematic description of pulsed laser deposition (PLD) deposition | 38 |
| 3-5 | Bragg diffraction | 39 |
| 3-6 | The geometry for a high resolution X-ray diffraction (HRXRD)..... | 39 |
| 3-7 | Schematic description of transport property measurement | 40 |
| 4-1 | XRD patterns of $\text{Ba}_2\text{FeMoO}_6$ thin films..... | 50 |
| 4-2 | Magnetization curves of $\text{Ba}_2\text{FeMoO}_6$ thin films grown at 700-900°C..... | 52 |
| 4-3 | The temperature dependence of the magnetization of $\text{Ba}_2\text{FeMoO}_6$ thin films grown at temperatures indicated | 53 |
| 4-4 | Magneto-resistance of $\text{Ba}_2\text{FeMoO}_6$ thin films | 54 |
| 4-5 | Transport properties of $\text{Ba}_2\text{FeMoO}_6$ thin films | 55 |
| 4-6 | SEM images of the samples grown at 700 to 900°C..... | 56 |
| 5-1 | XRD patterns of $\text{Ba}_2\text{FeMoO}_6$ thin films grown at 700°C under 0.1 to 10 mTorr O_2/Ar mixture gas | 66 |
| 5-2 | Magnetization curves of $\text{Ba}_2\text{FeMoO}_6$ thin films..... | 68 |
| 5-3 | The temperature dependence of the magnetization of $\text{Ba}_2\text{FeMoO}_6$ thin films | 69 |
| 5-4 | Magneto-resistance of $\text{Ba}_2\text{FeMoO}_6$ thin films grown at the oxygen pressures indicated and measured at 10K..... | 70 |

| | | |
|-----|---|-----|
| 5-5 | Transport properties of $\text{Ba}_2\text{FeMoO}_6$ thin films grown at 700°C under varying oxygen pressure indicated and measured at 300K..... | 71 |
| 6-1 | XRD patterns of $\text{Ba}_2\text{FeMoO}_6$ thin film and heterostructures..... | 80 |
| 6-2 | Magnetization curves of $\text{Ba}_2\text{FeMoO}_6$ thin films and hetero-structures measured at temperatures indicated..... | 82 |
| 6-3 | The temperature dependence of the magnetization $\text{Ba}_2\text{FeMoO}_6$ thin film and heterostructures..... | 83 |
| 6-4 | Magneto-resistance of $\text{Ba}_2\text{FeMoO}_6$ thin film and superlattices..... | 84 |
| 7-1 | XRD pattern of $\text{Ba}_2\text{FeMoO}_6/\text{Ba}_{0.5}\text{Sr}_{0.5}\text{TiO}_3$ (5xN) superlattices..... | 93 |
| 7-2 | Lattice parameters and periodicities of $\text{Ba}_2\text{FeMoO}_6/\text{Ba}_{0.5}\text{Sr}_{0.5}\text{TiO}_3$ (5xN) superlattices..... | 94 |
| 7-3 | Magnetization curves of $\text{Ba}_2\text{FeMoO}_6$ thin film and superlattices measured at temperatures indicated..... | 95 |
| 7-4 | Temperature dependence of the magnetization of $\text{Ba}_2\text{FeMoO}_6$ thin film and superlattices..... | 96 |
| 7-5 | Magneto-resistance of $\text{Ba}_2\text{FeMoO}_6$ thin film and superlattices measured at 10K..... | 97 |
| 7-6 | Transport properties of $\text{Ba}_2\text{FeMoO}_6/\text{Ba}_{0.5}\text{Sr}_{0.5}\text{TiO}_3$ (5xN) superlattices..... | 98 |
| 8-1 | Rocking curves of (002) peaks of $\text{ZnO:P}_{0.005}$ thin films grown on the buffer layers under oxygen pressures indicated..... | 106 |
| 8-2 | AFM images of $\text{ZnO:P}_{0.005}$ thin films grown on the buffer layers under oxygen pressures indicated..... | 107 |
| 8-3 | SEM images of $\text{ZnO:P}_{0.005}$ films grown on the buffer layers under oxygen pressures indicated..... | 108 |
| 8-4 | Cross section images of $\text{ZnO:P}_{0.001}$ thin films and buffer layers grown at 700°C under 10 mTorr O_2 | 109 |

Abstract of Dissertation Presented to the Graduate School
of the University of Florida in Partial Fulfillment of the
Requirements for the Degree of Doctor of Philosophy

GROWTH AND CHARACTERIZATIONS OF COMPLEX OXIDE THIN FILM
HETEROSTRUCTURES VIA PULSED LASER DEPOSITION

By

Kyeong-Won Kim

August 2012

Chair: David P. Norton

Major: Materials Science and Engineering

Artificially synthesized oxide thin films and hetero-structures have shown the novel properties that can be utilized in the next generation electronics. This dissertation investigates magneto-electric properties of half-metallic double perovskite $\text{Ba}_2\text{FeMoO}_6$ thin films and hetero-structures and p-type doping mechanism in ZnO thin films for the potential application in novel memory device and electronics.

Double perovskite $\text{Ba}_2\text{FeMoO}_6$ thin films and hetero-structures with $\text{Ba}_{1-x}\text{Sr}_x\text{TiO}_3$ have been prepared by pulsed laser deposition and the structural, magnetic and magneto-transport properties were investigated. Phase pure $\text{Ba}_2\text{FeMoO}_6$ thin films were epitaxially grown on SrTiO_3 substrates at temperatures ranging from 700-900°C under high vacuum. The magnetic properties of samples improved with high growth temperatures. $\text{Ba}_2\text{FeMoO}_6$ thin films showed anomalous Hall effect with hole-like behavior under low magnetic field and showed an ordinary electron-like transport property under high magnetic field. When thin films were grown under low oxygen partial pressure, the magnetic properties were degraded but the Curie temperature increased. Also unusual positive magneto-resistance observed in films grown under high vacuum disappeared, which suggests that it is associated with the oxygen related

defects. The $\text{Ba}_2\text{FeMoO}_6/\text{Ba}_{1-x}\text{Sr}_x\text{TiO}_3$ superlattices were synthesized and their structures were confirmed by X-ray diffraction analysis. The superlattices showed the strain induced enhancement of magnetization and the Curie temperature of superlattices were lowered substantially with increasing strain.

Phosphorus doped ZnO thin films were deposited on ZnO buffer grown under different growth conditions and the properties of thin films were examined, focusing on the role of buffer layers. Phosphorus doped ZnO thin films on buffer layer grown at low temperature were less conductive as grown state and showed a drastic change in the transport properties upon the rapid thermal annealing. This suggests that poor crystalline quality of the buffer layer grown at low temperature lead to the more incorporation of phosphorus dopants in following films. A high resolution X-ray diffraction study confirmed the poor crystalline quality of phosphorus doped thin films on low temperature deposited buffer layer by broader peaks of omega rocking curves. Also it was observed that the microstructures of the phosphorus doped ZnO thin film significantly depended on the buffer layer.

CHAPTER 1 INTRODUCTION

Developments and advances in the electronic industry have been fueled by Si-related semiconductor research, demands for miniaturization, and circuit speed. Also, technologies for display, photovoltaic and energy require material properties that cannot be achieved by the Si. These circumstances drive research in oxide materials. With the advances in thin film growth techniques like pulsed laser deposition (PLD)¹ and molecular beam epitaxy (MBE),² high quality oxide thin films can be deposited with an atomic control.^{3,4} Complex oxide hetero-structures with abrupt interfaces can often provide for properties that are not achievable in original parent materials such as extremely high mobility,⁵ conducting interface between insulating materials,⁶⁻⁸ and novel magnetic properties.⁹ Also, the strain induced by substrates or in superlattice structures has been a remarkable tool that can modulate material properties in unprecedented ways.^{10,11} These new phenomena and proposed devices based on the materials will be able to provide a path to new physics and applications for future generation electronics.

Double Perovskite $\text{Ba}_2\text{FeMoO}_6$ and Superlattices

The huge magneto-resistance observed in perovskite manganites, so called colossal magneto-resistance (CMR), has attracted significant interest for its potential applications for new types of memory devices. As early theoretical models of double-exchange couldn't completely explain observed properties, there have been various theoretical and experimental efforts to elucidate the phenomenon. Among them, a half-metallic ferromagnetic model which was developed based on spin-polarized band structure calculations has been widely used to explain related phenomena. Many non-

manganite oxide materials have been found to be half metallic and show large magneto-resistance. $A_2\text{FeMoO}_6$ ($A=\text{Ca, Sr, Ba}$) double perovskite is one of the materials that shows the half-metal like property with a huge magneto-resistance. Since $\text{Sr}_2\text{FeMoO}_6$ was reported to have a high spin-polarized state above room temperature, significant research has followed to study various aspects of the material.¹²

$\text{Ba}_2\text{FeMoO}_6$ has been less studied as $\text{Sr}_2\text{FeMoO}_6$ has attracted most of the interest largely due to the higher Curie temperature of 420K. Even with limited research, there have been promising reports of interesting magnetic and magneto-electric properties in $\text{Ba}_2\text{FeMoO}_6$. However, there lacks significant studies in thin film $\text{Ba}_2\text{FeMoO}_6$ system. This dissertation investigates the synthesis of $\text{Ba}_2\text{FeMoO}_6$ thin films by pulsed laser deposition (PLD) method and corresponding structural, magnetic and magneto-transport properties of the thin films. Also, complex hetero-structures with $\text{Ba}_{1-x}\text{Sr}_x\text{TiO}_3$ are synthesized and examined specifically focusing on the effect of strain on the magnetic and magneto-electric properties.

ZnO for Optoelectronics

ZnO has been intensely studied due to its potential for wide bandgap semiconductors electronics and optoelectronics. In particular, ZnO is considered a good candidate to replace GaN based III-V semiconductors due to some advantageous material properties such as large exciton binding energy, availability of single crystal substrate, and easy device processing. However, the absence of a reliable high quality p-type ZnO has been the main bottleneck for fully realizing this potential. Thus, a better understanding of doping mechanisms is required to take advantages of the excellent properties of ZnO. In Chapter 8, the transport properties of phosphorus doped ZnO thin

films are investigated, specifically focusing on the effects of buffer layer synthesis that provides some insight into the doping behavior.

CHAPTER 2 LITERATURE REVIEW

A₂FeMoO₆ Double Perovskites

Double perovskites (DPs) with the general formula A₂BB'O₆ comprise two interpenetrating simple perovskite (ABO₃) structures with a long range ordering of B and B' cations in B-sites. DPs are recognized as a particular type of half metallic oxide with a fully polarized conduction band, which with a Curie temperature (T_C) well above room temperature are of interest for applications that take advantage of the unusual magneto-transport and magnetic properties that are associated with the wide variety of available perovskite materials.¹³ DPs are remarkable materials with localized and itinerant ferromagnetism existing separately on the B and B' sublattices respectively.¹⁴ With the absence of both Jahn-Teller effects and antiferromagnetic superexchange due to increased separation of B-site cations, DPs also have higher T_C compared to manganites.¹⁴

Since the half metallic property of Sr₂FeMoO₆ was predicted and demonstrated, A₂FeMoO₆ (A=Ca, Sr, Ba) double perovskites have attracted significant interest for spin-transport related research.¹² Unlike colossal magneto-resistance (CMR) typically observed in manganites oxides materials,¹⁵⁻¹⁸ a huge magneto-resistance (MR) in the DPs remains at room temperature under low magnetic field.^{12,14,19-24} The crystal structure and Curie temperature of A₂FeMoO₆ DPs depend on the A-site cation and are summarized in Table 2-1.²¹

Sr₂FeMoO₆ is the most studied material due to its high Curie temperature relative to other DPs.^{12,24-35} The stoichiometry and ordering of B and B' cations (Fe and Mo) are known to be important for achieving desired properties. The ratio of Fe:Mo can widely

change various properties such as resistivity, Curie temperature, and saturation magnetization (M_S).³⁶ Sarma *et al.* reported the enhanced magneto-resistance at low temperature in an ordered sample.²⁵ However, ordering is not easy to be evaluated, particularly in thin films and thus inversely the saturation magnetization and magneto-resistance are commonly used to estimate ordering state in B-site cations. In contrast to reports realizing expected magnetic and magneto-electric properties in polycrystalline ceramic materials, it still remains as a challenge to fully reach the expected values, especially for M_S and MR, in thin film materials. The saturation magnetization values have been changing significantly with processing conditions in the reports.^{24,29,30,34,35,37} Thin film studies also revealed interesting features in transport properties such as a change in conduction mechanism, anomalous Hall effect, and unexpected positive magneto-resistance, which were believed to be associated with the spin glass phase induced by the disorder.³⁸⁻⁴⁰ X-ray photoelectron spectroscopy (XPS) studies have shown that the existence of Mo rich phase at the film surface might contribute to the degradation of magnetic property.^{34,35}

Even with a limited number of reports, there have been some interesting results reported in Ba_2FeMoO_6 .^{22,41-43} Lee *et al.* reported the effects of Fe/Mo disorder that leads to degradation of magnetization and magneto-resistance in a similar way as that found in Sr_2FeMoO_6 .⁴³ Grain size and crystalline quality were also reported to induce a large change in the magneto-resistance of the material.^{22,44} Thin film studies of this material have not been reported. A_2FeMoO_6 has a different crystal structures in bulk, but can be grown in a pseudo-cubic structure on properly chosen substrates such as $SrTiO_3$, $LaAlO_3$, and MgO .^{28,30,34}

Ferroelectric $\text{Ba}_{1-x}\text{Sr}_x\text{TiO}_3$

BaTiO_3 is probably the most well-known and studied ferroelectric material. Its Curie temperature is 393K in which it goes through a phase transition from tetragonal to cubic crystal structures and becomes paraelectric due to its centrosymmetry of a high temperature phase. When alloyed with SrTiO_3 , the Curie temperature and crystal structure of $\text{Ba}_{1-x}\text{Sr}_x\text{TiO}_3$ ($0 < x < 1$) are determined by the relative amount of strontium. Polycrystalline $\text{Ba}_{1-x}\text{Sr}_x\text{TiO}_3$ transforms from tetragonal to cubic phases and T_C decreases with increasing Sr content. Similar effects of Sr content on Curie temperature and crystal structure were reported in thin film $\text{Ba}_{1-x}\text{Sr}_x\text{TiO}_3$.⁴⁵ It should be noted that the properties of thin films significantly depends on various factors such as deposition condition, thickness, and strain from the substrates.⁴⁶⁻⁴⁸ $\text{Ba}_{1-x}\text{Sr}_x\text{TiO}_3$ has been combined with magnetic materials to realize multiferroic properties in many studies, which will be discussed later in detail.

Multiferroics and Superlattice Approach

Multiferroic materials are defined as materials that exhibit more than one primary ferroic order parameter simultaneously among four basic primary ferroic order parameters; ferromagnetism, ferroelectricity, ferroelasticity, and ferrotoroidicity.⁴⁹ It can be expanded to include non-primary order parameters such as antiferromagnetism or ferrimagnetism. However, recent interest is mainly focused on magneto-electric multiferroics which show both magnetic order and ferroelectric order at the same time. The search for these materials is driven by the potential for multifunctional devices in which electrical charges can be controlled by applied magnetic fields and vice versa.

Multiferroic property can be generated by different mechanisms. However, it can be categorized by the origin of ferroelectric ordering as the magnetic property is

basically determined by the atomic element. The first type of multiferroics is found in perovskite oxide materials which have lone pair electrons in their center atom. BiFeO_3 falls into this category and is the most studied single phase multiferroic material.⁵⁰⁻⁵² When exposed to an electric field, the lone pair electrons of Bi ions at the center can move by applied field and thus induce the ferroelectric ordering. The magnetic ordering comes from Fe ions at the corner. BiMnO_3 and PbVO_3 also belong to this group.^{53,54} Second, geometrically driven ferroelectricity enables multiferroic properties of materials such as hexagonal manganites, RMnO_3 ($R = \text{Ho-Lu, Y}$). In this group of materials, the symmetry is lowered by the tilting of MnO_5 bipyramids, which thus induces an electric dipole moment (shown in Figure 2-1).⁵⁵ Third, an electric polarization can be induced by a non-symmetric charge ordering in some magnetic insulator such as Fe_3O_4 .⁵⁶ This material undergoes a metal-insulator transition at 125K accompanied by charge ordering of iron ions. $\text{Pr}_{1-x}\text{Ca}_x\text{MnO}_3$ is also in this category.⁵⁷ Fourth, ferroelectricity can be driven by magnetic ordering, an effect that has been observed in orthorhombic rare earth manganites such as Tb(Dy)MnO_3 and $\text{Tb(Dy)Mn}_2\text{O}_5$.⁵⁸⁻⁶⁰ Last, multiferroic properties can be induced by strain. EuTiO_3 is intrinsically antiferromagnetic and paraelectric and turns into a ferroelectric ferromagnet under a specific strain state (shown in Figure 2-2).¹¹

Single phase multiferroic materials are rare due to the mutually exclusive conditions driving ferromagnetism and ferroelectricity, partially filled or empty transition metal orbitals, respectively.⁶¹ Due to the limited number of single phase multiferroic materials and a generally weak correlation in those materials, alternative approaches have been proposed by combining one magnetic material and one ferroelectric material

into horizontal and vertical composites.⁶²⁻⁶⁸ The horizontal hetero-structure called superlattice can be deposited as a few layers of alternating magnetic and ferroelectric materials by means of the atomic control of thin film deposition techniques.^{62,63,67} It is even possible to engineer magnetic ordering through superexchange interactions and compositional ordering that breaks an inversion symmetry to increase polarizations.^{64,69,70} Despite improved properties and interesting phenomena arising from the interface, there still remain challenges as to finding a good combination of those materials because two other materials should have comparable processing conditions.

p-type Doping in ZnO

ZnO generally crystallizes in the hexagonal wurtzite structure with lattice parameters of $a=3.25 \text{ \AA}$, $c=5.21 \text{ \AA}$. The ionic radii are 0.60 \AA for Zn^{2+} cation and 1.38 \AA for O^{2-} anion, respectively. The crystal structures shared by ZnO are hexagonal wurtzite, cubic zinc blende, and rock-salt as shown in Figure 2-3. At ambient conditions the thermodynamically stable structure is wurtzite. The zinc blende can be stabilized only by growth on cubic substrates and the rock-salt structure may be obtained under high pressures.⁷¹

ZnO is an intrinsically n-type direct bandgap semiconductor with the bandgap of 3.2 eV. There are various native defects in ZnO: vacancies (V_{O} and V_{Zn}), interstitials (Zn_i and O_i), and antisite defects (O_{Zn} and Zn_{O}). The formation energy of these defects, which determines their concentration, strongly depends on the growth condition. It is possible to get a high electron concentration of $10^{21} / \text{cm}^3$ even without extrinsic doping.⁷² The intrinsic n-type behavior of ZnO is known to be due to Zn interstitials (Zn_i) and oxygen vacancies (V_{O}), which are known as hole killer defects for intentional p-type

acceptor dopants. Whether Zn_i or V_O is dominant is still controversial. Look *et al.* suggested that Zn_i is dominant shallow donor with the ionization energy of 30-50 meV.⁷³ However, the first-principle study suggested that none of those native defects shows high concentration shallow donor characteristics.⁷⁴ In addition to the intrinsic defects, hydrogen is thought to be another n-type defect that should be taken into consideration. Hydrogen has a very small ionic radius and can be easily incorporated into the films during the synthesis. There have been several reports in which hydrogen acts as a shallow donor with the ionization energy of 30 meV.^{74,75} It is difficult to prevent the incorporation of hydrogen during growth, but hydrogen can be extracted at a high temperature.⁷⁶

N-type doping is relatively easy compared to p-type doping. Group III elements such as Al, Ga, and In and group VII elements such as F and Cl can be used to replace Zn and O sites, respectively. Myong *et al.*⁷⁷ synthesized Al-doped ZnO films by photo-assisted metal-organic chemical vapor deposition (MOCVD) method and obtained highly conductive films with a minimum resistivity of $6.2 \times 10^{-4} \Omega \cdot \text{cm}$. Such films are successfully used in various applications as n-type layers in light emitting diodes as well as transparent Ohmic contacts.

As mentioned already, p-type doping is the most challenging issue for ZnO based junction devices. By far, group V anions such as N, P, As, and Sb are the most studied elements, motivated by the obvious opportunity to hole dope via substituting anions for the -2 oxygen sites. Nitrogen is thought to be an ideal acceptor dopant due to the similar ionic size to oxygen (1.46 \AA for N^{3-} anion).⁷⁸ There have been successful reports of p-type doping with nitrogen by using various growth techniques including MBE and

PLD.^{79,80} However, a high hole concentration is difficult to achieve by N doping due to the difficulty of achieving high concentration incorporation into the films. Successful phosphorus doping has been reported by several groups but the mechanism of p-type conduction by phosphorus doping is not clearly understood.^{81,82} P has much larger ionic radius than that of O and thus it is not favorable energetically to substitute O site due to the large mismatch and strain energy from it (2.12 Å for P³⁻ anion). Theoretical studies predict that phosphorus forms defect complex, P_{Zn}-2V_{Zn}, which results in a shallow acceptor state.^{83,84} It should be noted that p-type conduction with phosphorus doping is achieved by thermal annealing following film deposition. Morhain *et al.*⁸⁵ reported p-type doping with As by PLD without post-deposition annealing.

The unipolar doping behavior of ZnO is commonly observed in many wide bandgap semiconductors.^{86,87} For example, GaN, ZnO, ZnS, and ZnSe are easily doped to n-type while p-type doping is difficult. By contrast, ZnTe is easy to get p-type doping and difficult to get n-type doping. This topic is well summarized by Zunger.⁸⁸ He explains preferential doping behavior in terms of band theory and chemical potential and suggests basic rules for doping based on them.

Due to the difficulty of p-type doping, ZnO has been used as an n-layer for heterostructural LEDs in which other materials such as NiO and GaN were employed as a p-layer.^{89,90} Recently, there have been several promising reports on ZnO homojunction LEDs. Until now most successful ZnO based LEDs were fabricated by using group V elements as a p-type dopant. Tsukazaki *et al.*⁹¹ proposed a repeated temperature modulation (RTM) technique as a reliable and reproducible way to fabricate p-type ZnO. The study used two different temperatures for p-layer growth; a low temperature for high

concentration of nitrogen incorporation and a high temperature for high crystalline quality and hydrogen extraction at the same time. Also, the results showed diodes with good rectification and better signal-to-noise ratio of the electroluminescence spectrum than previous reports. Lim *et al.*⁹² reported ultraviolet electroluminescence by phosphorus doping. Post-deposition rapid thermal annealing was used to activate acceptor dopants in the study. The p-type films show a high hole concentration of $10^{19}/\text{cm}^3$. The intensity of near-band edge emission was further increased and the deep-level emission was greatly suppressed by using $\text{Mg}_{0.1}\text{Zn}_{0.9}\text{O}$ layers as energy barrier layers to confine the carriers to the high-quality n-layer.

Table 2-1. Saturation magnetization (M_S) at 5K and 295K, Curie temperature (T_C), and room-temperature crystallographic structure as determined from x-ray diffraction of the double perovskite $AA'FeMoO_6$ ($AA' = Ba_2, BaSr, Sr_2, Ca_2$). (Adapted from ²¹)

| Nominal composition | M_S (5K) ($\mu_B \text{ fu}^{-1}$) | M_S (295K) ($\mu_B \text{ fu}^{-1}$) | T_C (K) | Cell parameters |
|---------------------|--|--|-----------|---|
| Ba_2FeMoO_6 | 3.53 | 1.33 | 308 | Cubic Fm3m $a = 8.0697(2) \text{ \AA}$ |
| $BaSrFeMoO_6$ | 3.4 | 1.89 | 340 | Cubic Fm3m $a = 7.9798(2) \text{ \AA}$ |
| Sr_2FeMoO_6 | 2.95 | 1.78 | 385 | Tetragonal $P4_2/m$ $a = 5.5724(2) \text{ \AA}$ $c = 7.9006(2) \text{ \AA}$ |
| Ca_2FeMoO_6 | 3.51 | 2.22 | 365 | Monoclinic $P2_1/n$ $a = 5.4131(2) \text{ \AA}$ $b = 5.5209(2) \text{ \AA}$ $c = 7.7065(2) \text{ \AA}$ $\beta = 89.95(5)^\circ$ |

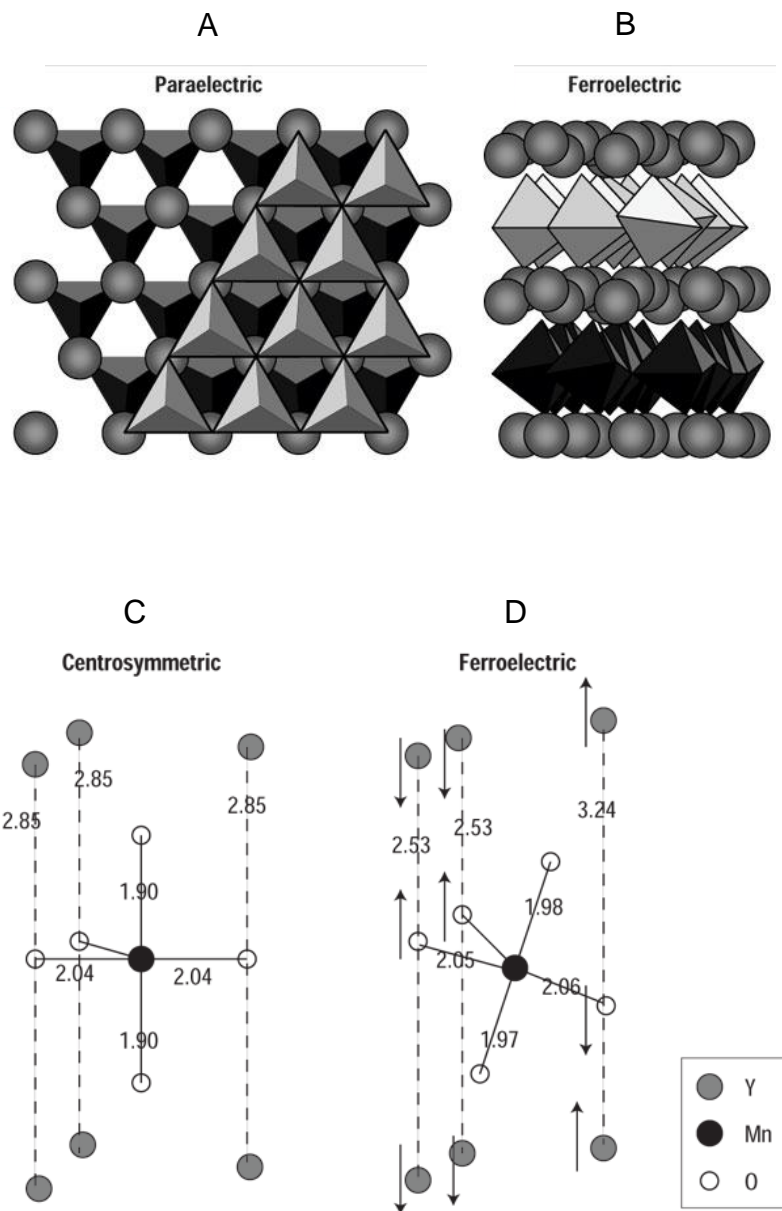


Figure 2-1. The crystal structure of YMnO_3 in the paraelectric and ferroelectric phases and schematic of a MnO_5 polyhedron with Y layers above and below. The trigonal bipyramids depict MnO_5 polyhedra and the spheres represent Y ions. A) The stacking of two consecutive MnO_5 layers and the sandwiched Y layer, looking down the c -axis in the paraelectric phase. B) A view of the ferroelectric phase from perpendicular to the c -axis, showing the layered nature of YMnO_3 . The calculated atomic positions of the C) centrosymmetric and D) ferroelectric structures. The numbers give the bond lengths in Å. The arrows indicate atomic displacements with respect to the centrosymmetric structure. (Adapted from ⁵⁵)

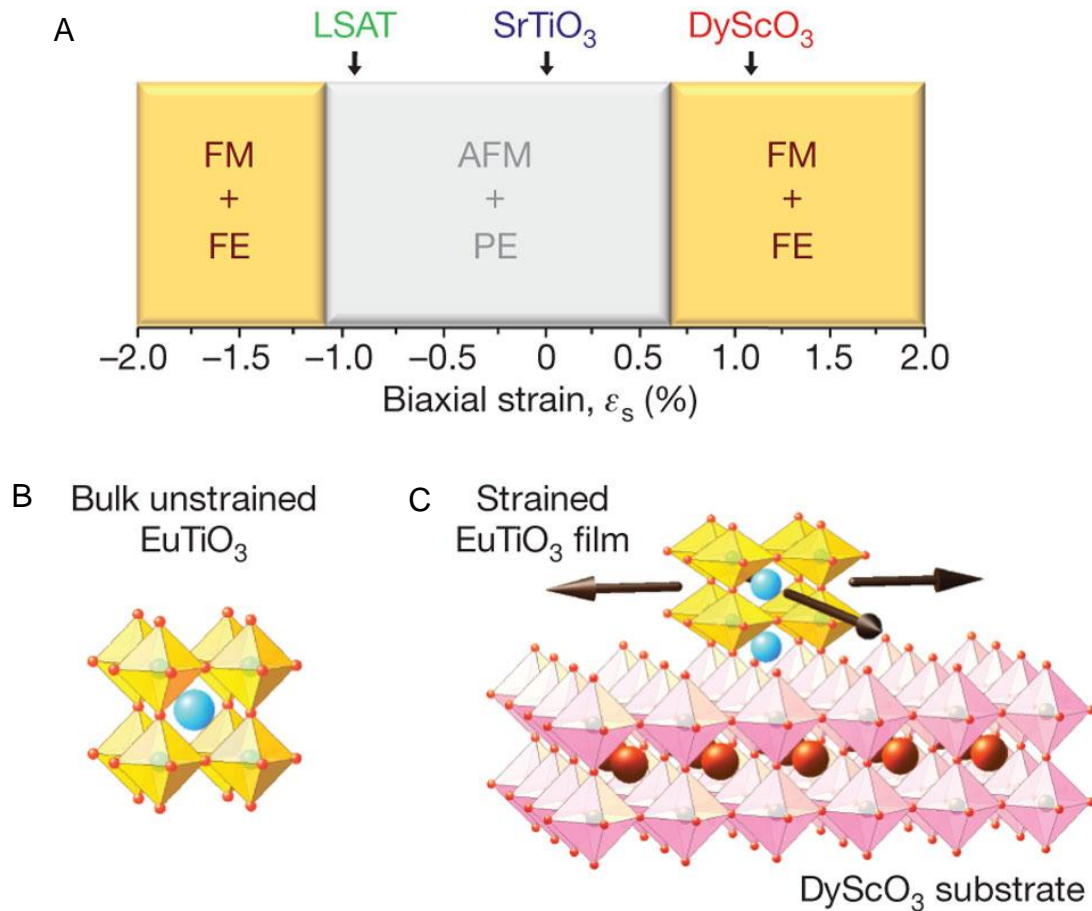


Figure 2-2. Multiferroic properties induced by strain from substrate. A) First-principles epitaxial phase diagram of EuTiO_3 strained from -2% (biaxial compression) to $+2\%$ (biaxial tension), calculated in 0.1% steps. Regions with paraelectric (PE), ferroelectric (FE), antiferromagnetic (AFM) and ferromagnetic (FM) behavior are shown. B) Schematic of unstrained bulk EuTiO_3 . C) Epitaxially strained thin-film EuTiO_3 on the DyScO_3 substrate showing the in-plane expansion due to biaxial tension. (Adapted from ¹¹)

CHAPTER 3 EXPERIMENTAL DETAILS AND CHARACTERIZATIONS

Target Synthesis

Ba₂FeMoO₆

The target was synthesized by a conventional solid state reaction. The starting materials were high purity (99.99% or higher) powders of BaCO₃, Fe₂O₃ and MoO₃. First, the powders were mixed for 24 hours by dry ball milling and the mixed powder was calcined at 900°C under reducing atmosphere of 5% H₂ buffered with Ar gas for 6 hours. The calcined powder was ground by mortar and pestle. It was pressed into a one-inch diameter die by hand press and then further pressed under 150 MPa for three minutes by cold isostatic pressure. It was sintered at 1150°C under the same reducing atmosphere for four hours. The calcined and sintered powders were examined by X-ray diffraction and synchrotron diffraction. The XRD patterns of calcined and sintered powders in air and reducing atmosphere were shown in Figure 3-1. The final powders heat treated under reducing atmosphere showed only peaks from Ba₂FeMoO₆ marked with stars in contrast to the powders processed in air containing impurity phases. The diffraction data obtained from synchrotron source were analyzed with Rietveld refinement using the GSAS program. The refined crystal structure of Ba₂FeMoO₆ is cubic (Fm-3m) with the lattice parameter of 8.0752 Å and the obtained composition after refinement is Ba_{2.0374}Fe_{1.0935}Mo_{1.0065}O_{6.4476} summarized in Figure 3-2. The crystal structure was generated with the data using the Crystal Maker program shown in Figure 3-3.

Ba_{1-x}Sr_xTiO₃ (x=0, 0.5)

The targets were synthesized by a conventional solid state reaction. The starting materials for a target were high purity (99.99% or higher) powders of BaTiO₃, SrTiO₃. First, the powders were mixed to desired compositions using mortar and pestle for an hour. It was pressed into a one-inch diameter die by hand press. It was then sintered at 1400°C in air for 10 hours.

Phosphorus Doped ZnO

The targets of undoped and 0.1 & 0.5 atomic % doped ZnO were synthesized by a conventional solid state reaction. The starting materials for a target were high purity (99.99% or higher) powders of ZnO and P₂O₅. First, the powders were mixed to stoichiometric compositions using mortar and pestle for an hour. It was pressed into a one-inch diameter die by a hand press. It was then sintered at 1200°C in air for four hours.

Thin Film Deposition

All the thin films and hetero-structures were deposited by pulsed laser deposition (PLD) in this research. In this technique, a high power pulsed laser is used to ablate a target. Pulsed ablations melt, evaporate, and ionize the surface of a target and lead to formation of a plasma plume in which atoms and molecules are transferred onto a substrate. In Figure 3-4, a sketch is shown for schematic of PLD system with the image of a plasma plume.

PLD has been widely used to deposit high quality thin film materials. This technique has significant advantages over other film deposition techniques. It allows the deposition from almost any materials with the limitation of bandgap and absorption of the laser energy. It can provide the stoichiometric material transfer from target to film of

any desired composition (under optimized growth conditions), the creation of solid solution, multi-cation epitaxial films, which are often difficult to make the targets of desired compositions. Also, it can give a path to multilayers of different materials by using multiple targets.

Despite these advantages, PLD is still confined to research purposes due to three main reasons. First, the deposited area is relatively small. Second, a plasma plume created during ablation is highly directional and therefore induces non-uniform thicknesses over a film. Last, the extended period of ablation of a target sometimes results in formations of particulate in the plume and thus incorporation of them in film materials.

Substrate Preparation

(100) oriented SrTiO₃ substrates are used to deposit perovskite thin films and hetero-structures. As-received SrTiO₃ substrates are etched and then annealed to acquire TiO₂-terminated surfaces. The detailed procedure is as follows. First, as-received SrTiO₃ substrates were rinsed in deionized water for 5 minutes and blown dry with nitrogen gas. Second they were etched in buffered oxide etchant for 15-20 seconds, rinsed in deionized water for 5 minutes, and blown dry with nitrogen gas. Last, the substrates were annealed at 900°C for three hours in flowing oxygen. All substrates were rinsed with trichloroethylene (TCE), acetone, and methanol for 10 minutes each and then blown dry with nitrogen gas.

ZnO and phosphorus doped ZnO thin films were grown on *c*-plane (0001) sapphire substrates. The substrates were rinsed with trichloroethylene (TCE), acetone, and methanol for 10 minutes each and then blown dry with nitrogen gas before deposition.

Ba₂FeMoO₆, Ba_{1-x}Sr_xTiO₃ (x=0, 0.5) Thin Films and Hetero-Structures

Before the deposition, the chamber was pumped down to the base pressure of $\sim 10^{-9}$ Torr. The samples were deposited at temperatures ranging from 600-900°C. The atmosphere and pressure used were $\sim 10^{-7}$ Torr (without any external gas feed in), 1-10 mTorr for pure O₂, and 0.1-100 mTorr O₂/Ar (0.2% oxygen) mixture gas. The growth condition for each sample was described in detail in the experimental part of chapter 4-7. The laser energy and the repetition rate were 1.5 J/cm² and 1-5 Hz, respectively.

Phosphorus Doped ZnO Thin Films

The chamber was pumped down to the base pressure of $\sim 10^{-8}$ Torr. ZnO buffer layers were grown under two conditions: low and high temperature buffer layers were grown at 400°C under 20 mTorr O₂ and 700°C and 1 mTorr O₂. Phosphorus doped ZnO were grown at 700 °C under 10 & 150 mTorr O₂. The laser energy and the repetition rate were 1.5-2 J/cm² and 1 Hz, respectively. After the deposition, samples were rapid thermal annealed at 900°C for 3-5 minutes under oxygen atmosphere to convert the carrier type in thin films.

Characterization Techniques

X-ray Diffraction (XRD)

X-ray diffraction is a widely used non-destructive technique to investigate the phase, crystallographic structure, lattice spacing of various forms of materials such as powder, single crystal, and thin films. The basic principle of x-ray diffraction is Bragg equation for diffraction,

$$n\lambda = 2d\sin\theta,$$

where n is the order of diffraction, λ is the wave length of an incident x-ray beam, d is the distance between specific crystallographic planes, and θ is the angle between the

incident beam and the atomic plane. Figure 3-5 shows the basic interpretation of Bragg diffraction condition. The Philips APD 3720 was used to examine the crystalline phases and the periodicity of superlattice samples at the Major Analytical Instrumentation Center (MAIC) at University of Florida. In addition, Philips MRD X'pert was used to examine the epitaxy and lattice parameters of samples. The detailed geometry information of this high resolution XRD was depicted in Figure 3-6.

Atomic Force Microscopy (AFM) and Scanning Electron Microscopy (SEM)

Atomic force microscopy (AFM) or scanning probe microscopy (SPM) is the most commonly used technique to examine the surface structure and roughness of a sample. For high quality device fabrication, smooth film surfaces are required. An AFM is a mechanical imaging instrument that measures the three dimensional topography as well as physical properties of a surface with a sharpened probe. The sharpened probe is positioned close enough to the surface such that it can interact with the force fields associated with the surface. An image of the surface is reconstructed by monitoring the precise motion of the probe as it is scanned over the surface. A Digital Instruments Dimension 3100 was used to observe the surface morphology of thin films at the MAIC facility.

Scanning electron microscopy (SEM) is a basic tool to observe the microstructure of a sample. At the MAIC facility, a JEOL JSM 6335F field emission gun SEM was used to observe the microstructure of sample surfaces as well as vertical structures.

Auger Electron Spectroscopy (AES)

Auger electron spectroscopy is a quantitative analysis technique to investigate the chemical properties of materials. This technique is based on Auger Effect, which is an electronic process resulting from inter- and intrastate transitions of electrons in an

excited atom. When a sample is probed by electron beams, an inner shell electron can be removed leaving behind a hole. As this state is unstable, the hole can be filled by an outer shell electron which loses energy when it drops to the inner shell. If this transition energy is greater than the orbital binding energy, it induces an emission of electron in the outer shell. Since orbital energies are unique to an atom of a specific element, the ejected electrons can provide the information about the chemical composition of a surface. Due to the nature of Auger electrons, this technique provides a high sensitivity to surface. A spot, line, and area analysis can be carried out with help of an electron microscope. Perkin-Elmer PHI 660 – AES at the MAIC facility was used to examine the chemical properties of thin films.

Hall Effect and Magnetoresistance

Hall effect is the generation of potential difference over an electrical conductor perpendicular to both an electric current flowing along the conductor and an external magnetic field, when it is put in the magnetic field applied at right angles to the current upon application of the magnetic field. The basic principle is schematically depicted with the van der Pauw sample geometry used in this research in Figure 3-7. As deflecting direction that a charge carrier experiences depends on the type of a carrier, it can be used to investigate the type, concentration, mobility of charge carriers.

The magneto-resistance effect is a change in the electrical resistance R of a substance when a magnetic field is applied on it. The value is defined as $\Delta R/R_0$, where R_0 is the resistance under no magnetic field. The value of magneto-resistance is very small for most materials, but is relatively large (a few percent) for strongly magnetic materials. Very large values of magneto-resistance have been observed in certain special materials and thin film arrays. The resistance of thin film structures composed of

alternating ferromagnetic and nonmagnetic materials shows a substantial difference (~10%) in resistivity depending on whether the magnetizations in the magnetic layers are parallel or antiparallel. This gives what is known as Giant Magneto-resistance (GMR), which has found an application in the read heads for a hard disk drive. And certain perovskite oxides containing manganese and rare earths show an even larger magneto-resistance (100% or more), leading them to be called Colossal Magneto-resistive materials (CMR). They are also candidates for magnetic field detectors in computer drives. More recently, double perovskite oxide $\text{Sr}_2\text{FeMoO}_6$ shows large magneto-resistance (~30%) even at a room temperature.

In this research, Lakeshore 7507 Hall Effect-Electronic measurement system and Quantum Design Physical Properties Measurement System (PPMS) were utilized to investigate the transport properties of samples, specifically focusing on the behavior under applied magnetic field.

Superconducting Quantum Interference Device (SQUID)

Superconducting quantum interference device (SQUID) is a highly sensitive magnetometer that can measure generally about 10^{-7} emu. This device is based on the tunneling of superconducting electrons across a very narrow gap, called a Josephson junction, between two superconductors. It's designed so that equal currents pass through each of two Josephson junctions when a superconducting current flows through the ring. A change in magnetic flux through the ring by an applied magnetic field generates a voltage and a current in the ring, according to Faraday's Law. This induced current adds to the measuring current in one junction, and subtracts in the other. Because of the wave nature of the superconducting current, the result is a periodic appearance of resistance in the superconducting circuit, and the appearance of a

voltage. Each voltage step corresponds to the passage of a single flux quantum across the boundary of the ring. The existence of the flux quantum was demonstrated in somewhat similar experiments on superconducting rings; its value is $h/2e = 2.07 \times 10^{-7}$ weber or Tm^2 . This sensitivity is rarely needed to measure a magnetic field and in practice the device is most commonly linked to a coil to measure the flux from a small sample and thus the sample magnetization. In this form, it is called a SQUID magnetometer. Since a superconducting Josephson junction device requires low temperature operation, it is usually used in conjunction with a superconducting solenoid. In this research, Quantum Design Magnetic Properties Measurement System (MPMS) sample magnetometer was used to investigate the $\text{Ba}_2\text{FeMoO}_6$ thin film and superlattice samples.

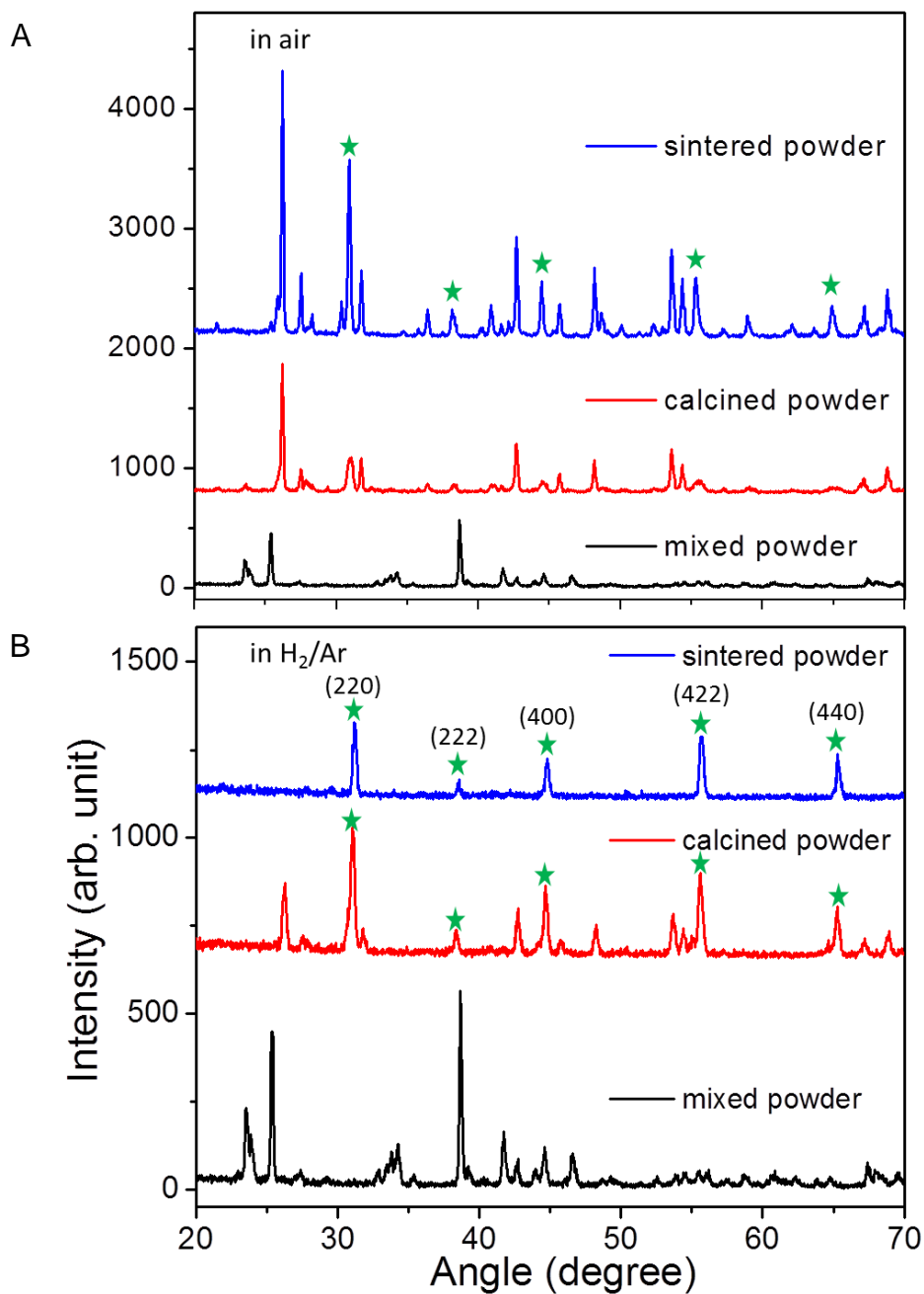
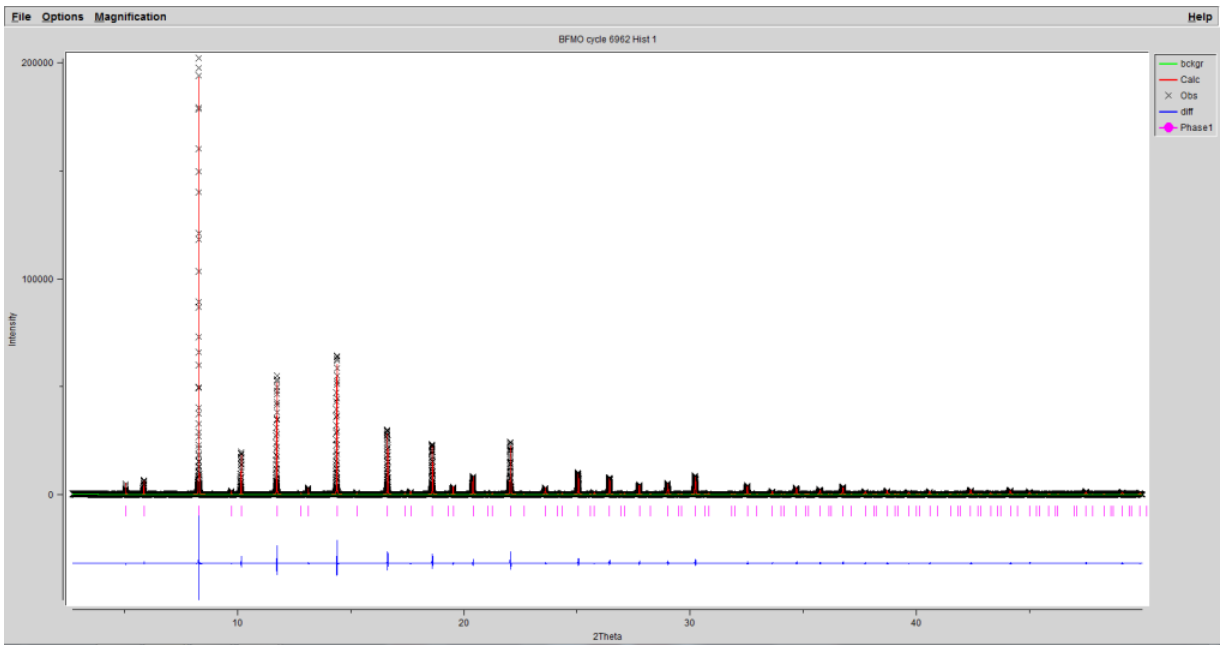


Figure 3-1. XRD patterns of $\text{Ba}_2\text{FeMoO}_6$ powders calcined and sintered. Images give for A) air and B) reducing atmosphere. The peaks marked with star represent the phases from $\text{Ba}_2\text{FeMoO}_6$.



Chi square = 6.72 %
 Structure: Cubic F m-3m
 $a = b = c = 8.072 \text{ \AA}$
 $\alpha = \beta = \gamma = 90^\circ$
 Composition: $\text{Ba}_{2.0374}\text{Fe}_{1.0935}\text{Mo}_{1.0065}\text{O}_{6.4476}$

Figure 3-2. Rietveld results of the diffraction data of $\text{Ba}_2\text{FeMoO}_6$ powders from synchrotron source.

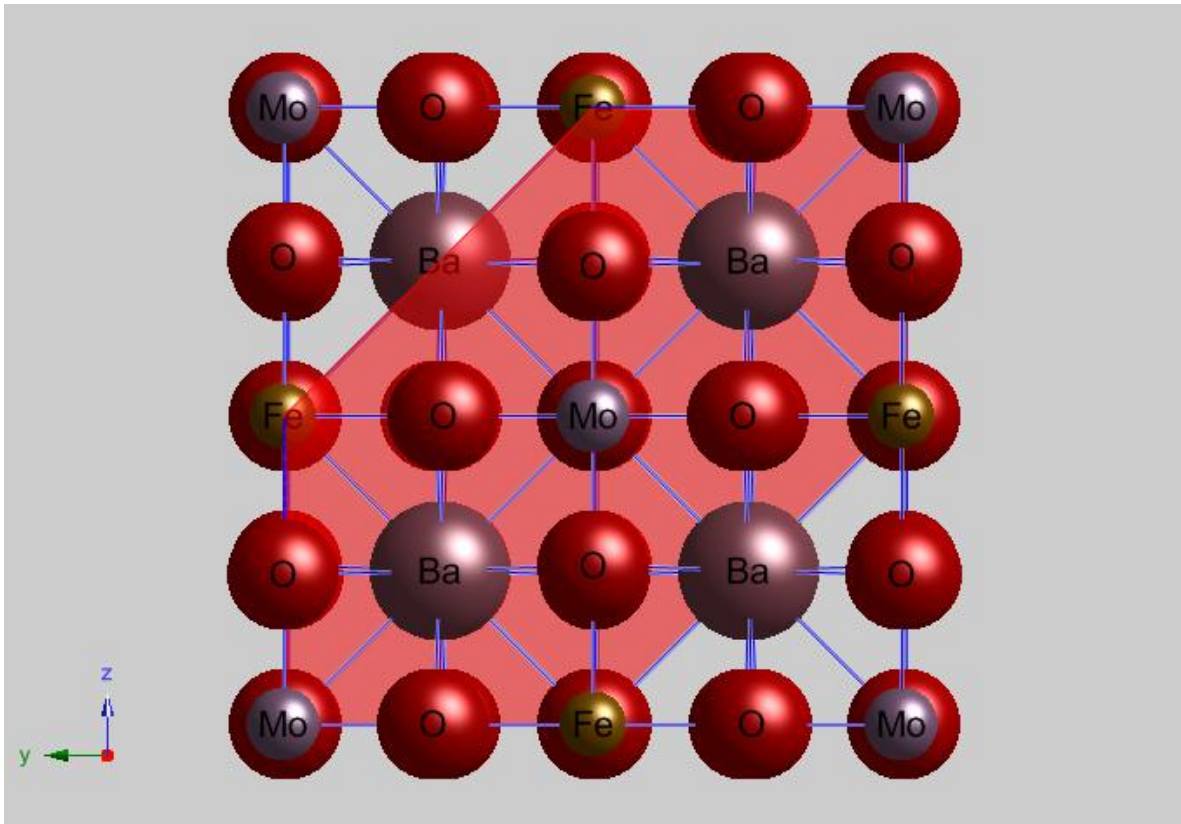


Figure 3-3. Crystal structure of $\text{Ba}_2\text{FeMoO}_6$ from (100) direction generated by CrystalMaker using the refinement data.

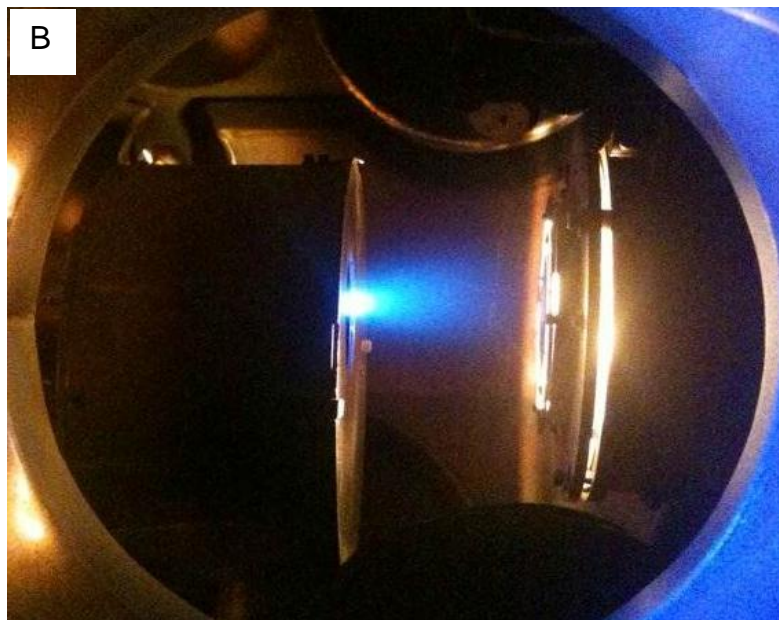
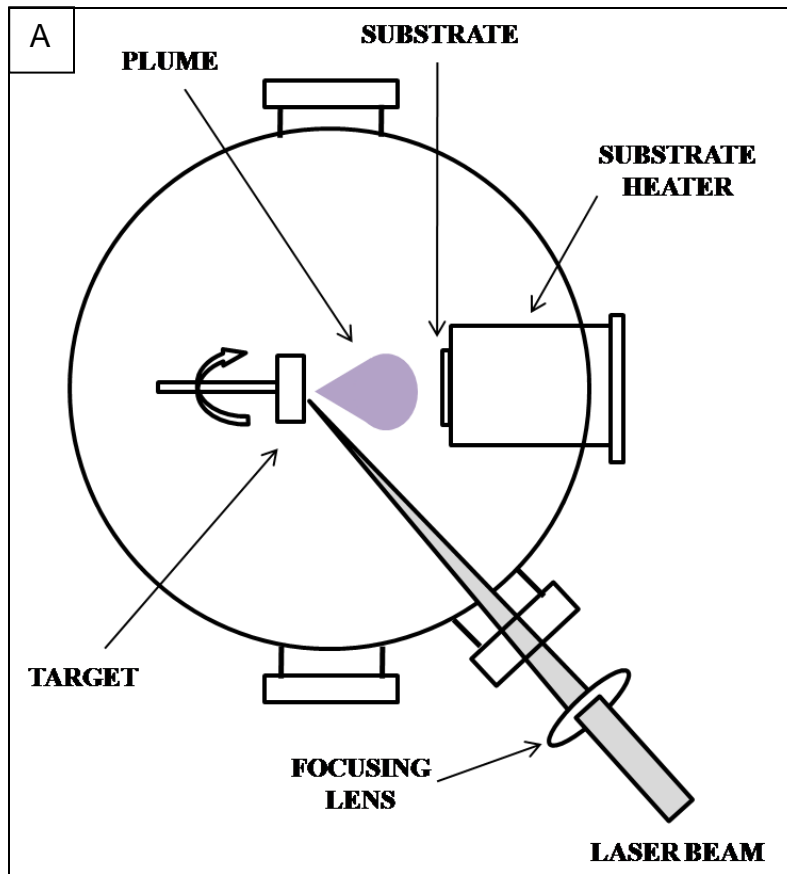


Figure 3-4. Schematic description of pulsed laser deposition (PLD) deposition. Images given for A) for system and B) a plasma plume.

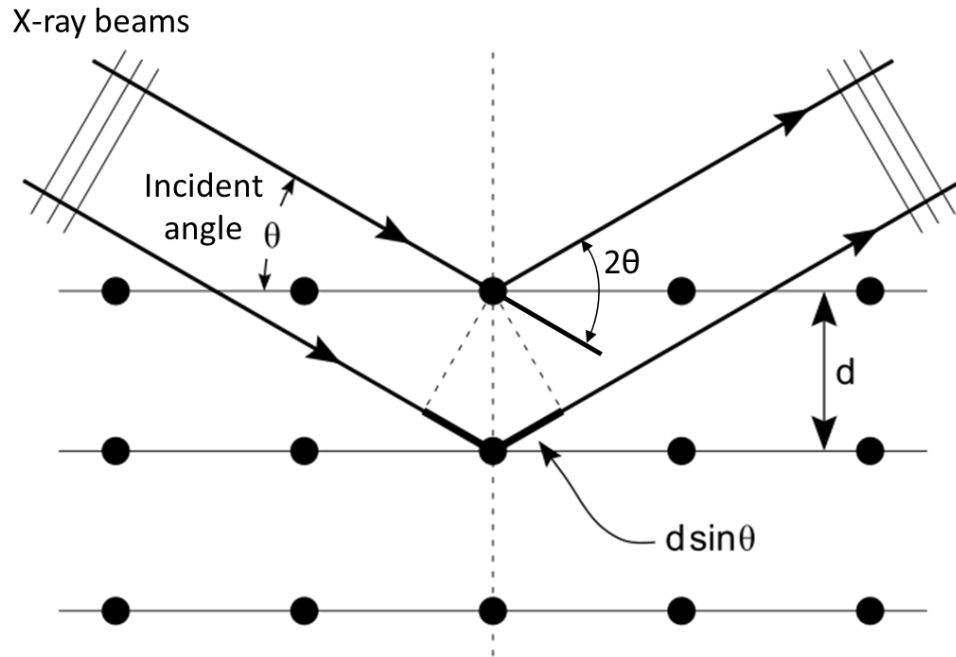


Figure 3-5. Bragg diffraction

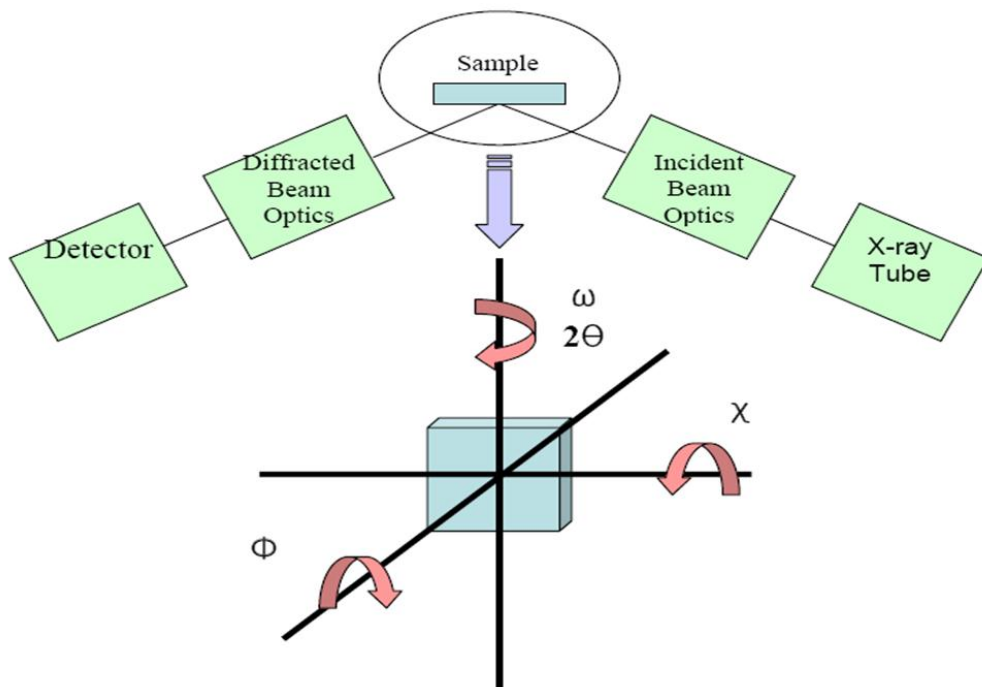


Figure 3-6. The geometry for a high resolution X-ray diffraction (HRXRD)

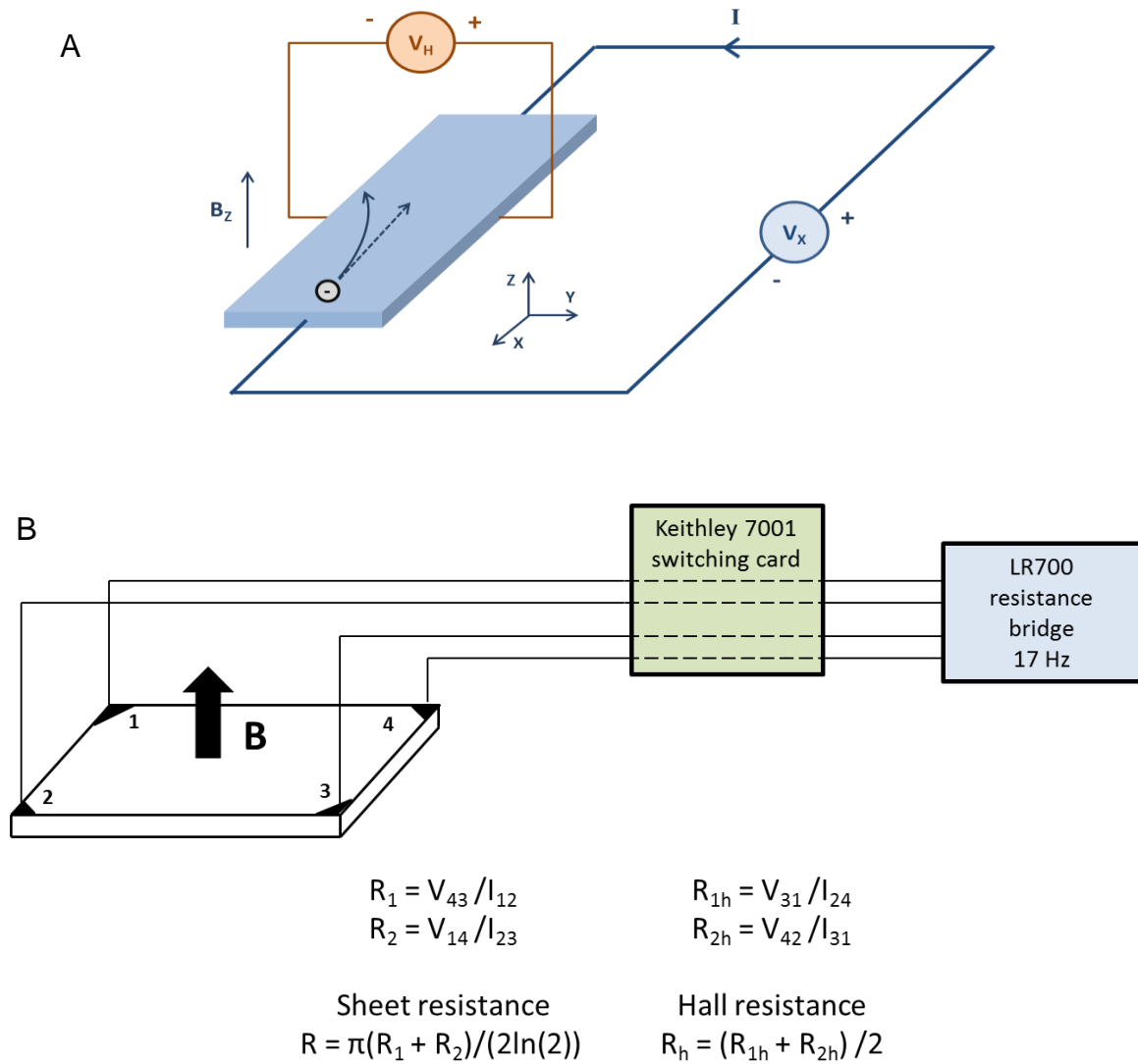


Figure 3-7. Schematic description of transport property measurement. Images given for A) Hall effect and B) van der Pauw geometry.

CHAPTER 4
MAGNETIC AND MAGNETOTRANSPORT PROPERTIES OF Ba₂FeMoO₆ PULSED
LASER DEPOSITED THIN FILMS

Introductory Remarks

Half metallic oxides have attracted a significant interest in the field of spin-polarized transport applications. However, in most material systems, the high spin polarization disappears at room temperature due to a low Curie temperature (T_C). Since Kobayashi *et al.*¹² reported that half-metallic double perovskite Sr₂FeMoO₆ remains as high spin polarized state at room temperature due to its high T_C up to 420K, this material has been of interest for its spin-polarized transport properties and considered a good candidate for device application.^{19,20,38,93,94} A simulation study suggested that the defect-free Sr₂FeMoO₆ has a high T_C of 450K and a saturation magnetization of 4 μ_B per formula unit (f.u.) at a low temperature with a long range antiferromagnetic ordering among Fe³⁺ ions and Mo⁵⁺ ions.²⁰ However, the experimental values of a saturation magnetization have been reported to be lower than 4 μ_B /f.u. in most studies; achieving this value seems more challenging in thin film materials.

Ba₂FeMoO₆ is a member of the double perovskite A₂FeMoO₆ (A=Ba, Ca, Sr) family and reported to have T_C as high as 367K.¹⁹ Even though Ba₂FeMoO₆ has attracted less interest mainly due to the lower T_C than Sr₂FeMoO₆, there have been multiple reports of over 30% negative magneto-resistance for polycrystalline ceramic samples.^{22,44} However, there lack studies on thin film Ba₂FeMoO₆.

In this study, we have prepared epitaxial Ba₂FeMoO₆ thin films on SrTiO₃ substrate and investigated their magnetic and magneto-transport properties. Samples grown at high temperatures showed higher values in saturation magnetization and magneto-resistance. Interestingly, a change from positive to negative magneto-

resistance was observed under increasing magnetic field. Also, an anomalous Hall effect was observed accompanied by conduction mechanism changes for different temperature ranges.

Experimental

The $\text{Ba}_2\text{FeMoO}_6$ thin films were deposited on SrTiO_3 substrates by pulsed laser deposition with a stoichiometric target. The target was synthesized by a conventional solid state reaction. The starting materials for a target were high purity (99.99% or higher) powders of BaCO_3 , Fe_2O_3 and MoO_3 . First, the powders were mixed for 24 hours by dry ball milling and the mixed powder was calcined at 900°C under reducing atmosphere of 5% H_2 buffered with Ar gas for 6 hours. The calcined powder was ground by mortar and pestle. It was pressed into a one-inch diameter die by hand press and then further pressed under 150 MPa for three minutes by cold isostatic pressure. It was sintered at 1150°C under the same reducing atmosphere for four hours. The calcined and sintered powders were examined by X-ray diffraction and synchrotron diffraction. The diffraction data obtained from synchrotron source were analyzed with Rietveld refinement using the GSAS program. The refined crystal structure is cubic with the lattice parameter of 8.0752 \AA and the obtained composition after refinement is $\text{Ba}_{2.00}\text{Fe}_{1.07}\text{Mo}_{0.99}\text{O}_{6.33}$.

The thin films were deposited under vacuum at temperatures ranging from 600 to 900°C for two hours. The chamber was pumped down to the base pressure of $\sim 10^{-9}$ Torr and the pressure during deposition was in the order of 10^{-7} Torr. The 248 nm wavelength KrF laser was employed to ablate the ceramic target. The laser energy and the repetition rate were 1.5 J/cm^2 and 4 Hz , respectively. The growth rate is around 0.1 \AA per laser pulse.

The crystal structure and phase of the thin films were examined by X-ray diffraction (Phillips APD3720 and Phillips MRD X'pert). Magnetization, Hall effect and magneto-transport were respectively measured using Quantum Design Magnetic Properties Measurement System (MPMS) and Physics Properties Measurement System (PPMS). In addition, a field emission scanning electron microscope (JEOL 6335F) was used to observe the microstructure of samples.

Results and Discussion

Figure 4-1A shows the XRD patterns of the Ba₂FeMoO₆ thin films grown at 900°C under $\sim 10^{-7}$ Torr without external gas feed in and 1×10^{-3} Torr oxygen ambient. An impurity BaMoO₄ phase is observed in the sample grown under oxygen ambient in contrast to the phase pure sample grown under $\sim 10^{-7}$ Torr. Figure 4-1B shows the XRD patterns of the Ba₂FeMoO₆ thin films grown at 600-900°C under $\sim 10^{-7}$ Torr. All films are phase-pure and oriented along the *c*-directions in which the (00*l*) peaks of films are observed next to the (00*m*) peaks of SrTiO₃ substrate. And the epitaxial growth is confirmed by in-plane phi scan in Figure 4-1C and the reciprocal space map shows that the film is slightly relaxed as shown in Figure 4-1D. As the growth temperature increases, the (004) peaks of the films show a continuous shift to high angle, which indicates a decrease of the *c*-lattice parameter. This might be due to compositional change of Fe:Mo and the different lattice sizes of BaFeO₃ (4.02 Å) and BaMoO₃ (4.04 Å),⁹⁵ though a systematic change was not observed in Fe:Mo ratio from SEM/EDS analysis, of which the resolution might not be good enough for a slight change in composition. The Fe:Mo composition can vary with the growth temperature due to the different volatility and sticking coefficients during the deposition. Also, the oxygen content is another possibility that can affect the lattice parameter change. It is known

that the lattice parameter can be affected by oxygen content in the sublattices of BaFeO₃ and BaMoO₃ as well as the double perovskite SrFeMoO₆.^{38,96}

Magnetization loops with magnetic fields oriented perpendicular to the c-axis are plotted in Figure 4-2. At 10K, Figure 4-2A shows typical ferromagnetic behavior in which the saturation magnetization with values near 0.4, 0.8, and 1.1 μ_B /f.u. for the 700, 800, and 900°C samples respectively increases with increasing growth temperature. Also as shown in the lower panels of Figure 4-2B plotted with magnetic field on an expanded scale, the coercive fields increase for the higher growth temperature samples, although the values are small. It is clear from the above discussion that both the magnitude of the magnetization and the coercive field improve with higher growth temperature, presumably because of better crystalline quality. But the low values of M_S ($\sim 1 \mu_B$ /f.u.) compared to the predicted 4 μ_B /f.u. can be explained by the compositional variance, i.e., B:B' site order-disorder and oxygen content. It is well known that this double perovskite material and the substructural BaFeO₃ and BaMoO₃ are very sensitive to the oxygen content.^{94,96-98} Sarma *et al.* reported that disordering of Fe/Mo sites in Sr₂FeMoO₆ has a significant negative effect on magneto-transport properties of the material.²⁵ The coercive field increases with increasing growth temperature, though the values are still small below 1 kOe. At 300K, the samples still show the saturation of magnetization but the coercive field is strongly diminished.

In Figure 4-3A-C, the temperature dependence of magnetization is shown in both field cooled (FC) and zero field cooled (ZFC) protocols. In the zero field cooled method, a sample is cooled from room temperature without any applied magnetic field and then a small magnetic field of 100 Oe is applied at 10K. The magnetization is measured as a

function of temperature during warm up under a constant field. In field cooled case, the sample is cooled from room temperature to 10K in an applied magnetic field and magnetization is measured during warm up. The sample grown at 700°C has a T_C higher than 300K. It is consistent to the fact that the saturation magnetization remains almost the same at 10K and 300 K for the 700°C sample. Also the FC data in Figure 4-3A show an increase of magnetization during warm-up, which is unusual as in FC mode magnetization should always decrease with increasing temperature (increased thermal energy destroys spin alignment and decreases magnetization). It is interesting to note that the saturation magnetization depends on growth temperature while both the Curie temperature (near where M deviates from a constant value) and the irreversibility temperature (marked by the deviation between FC and ZFC curves) remains roughly constant for the samples grown at 800 & 900°C. This correlated behavior of T_C and M can be explained using antisite (AS) disorder, where Fe & Mo exchange their site positions without changing carrier density n . It has been shown both theoretically¹⁴ and experimentally⁹⁹ that AS disorder systematically reduces the saturation magnetization (M_S) without affecting T_C in $\text{Sr}_2\text{FeMoO}_6$. The curves show that the Curie temperatures (T_C) are around 250K for samples grown at 800°C and 900°C, which is lower than 367K reported for $\text{Ba}_2\text{FeMoO}_6$ ceramics.¹⁹ The FC data in Figure 4-3B shows a decrease of magnetization during cooling followed by an increase at lower temperatures, which may be due to the presence of both ferromagnetic and antiferromagnetic couplings in these non-optimized films.

Figure 4-4A shows the magneto-resistance of the samples. All samples show typical negative magneto-resistance at a high magnetic field. However, the sample

grown at 900°C shows a positive magneto-resistance below 2 T. There is a report that Sr₂FeMoO₆ thin films showed the positive or negative magneto-resistance when grown at different temperatures,³⁸ but in that report the samples showed only one characteristic depending on growth condition throughout the whole magnetic field range, while in our 900°C sample the magneto-resistance reflects a positive contribution at low fields and a stronger negative contribution at high fields. The positive magneto-resistance is not fully understood. A similar type of field dependence of magneto-resistance was reported in dilute magnetic semiconductor of (Ga,Mn)As,¹⁰⁰ in which the positive magneto-resistance was believed to be induced by the rotation of spins and it disappeared when the magnetic field was applied parallel to the sample plane. We observed in the sample grown at 700°C a negative magneto-resistance of -3% at a temperature of 10K and a magnetic field of 7 T. The small value of magneto-resistance is believed to be mainly due to disorder in the films. The degradation of magneto-resistance by disorder has been reported in double perovskite ceramics.^{25,32,44} The sample grown at 900°C has a smaller negative magneto-resistance value which is to some extent due to cancellation by the positive region observed at small magnetic fields. In Figure 4-4B, the magneto-resistance decreases with increasing temperature and it almost disappears at room temperature which is expected from the thermal dependence of magnetization results.

The resistivity and Hall resistivity are plotted in Figure 4-5A and B, respectively. The resistivity decreases with increasing growth temperature for all samples and a large dependence on temperature is observed from the sample grown at 700°C. A closer look at the plot for the sample grown at 700°C reveals a change in conduction mechanism at

different temperature ranges. The resistivity increases logarithmically with decreasing temperature below 20K, which is observed in Kondo system. Even though Kondo system originally describes the transport property of a metallic system with magnetic impurities,¹⁰¹ there have been reports of Kondo like behavior in ferromagnetic materials including ferromagnetic perovskite oxide materials.^{102,103} It is believed that this behavior is correlated with the spin glass phase induced by disorder.³⁷ It is also another indication of the disorder in the B-cation arrangements of the $A_2BB'O_6$ double perovskite. Segregation into the clusters of $BaFeO_3$ or $BaMoO_3$ may induce a significant change in magnetic and magneto-electric properties of double perovskite since it is well known that those two materials have quite different properties. Above 50K, on the other hand, the temperature dependence can be described by $R \propto \exp[(T_0/T)^{0.25}]$. This change in a conduction mechanism is very similar to the report on epitaxial double perovskite Sr_2FeMoO_6 thin films, though there are small discrepancies in temperature ranges for each dependency.³⁹

In ferromagnetic materials, the transverse resistivity is given by

$$\rho_{xy} = R_H B + R_A \mu_0 M,$$

with the magnetization M and the ordinary and anomalous Hall coefficients R_H and R_A , respectively.¹⁰⁴ The Hall resistivity is measured at constant temperatures of 10, 100 and 300K up to 7 T and shown in Figure 4-5B. In low magnetic fields, the Hall resistivity is dominated by the anomalous Hall contribution which behaves hole-like as indicated by the positive slope. This positive sign arises because the single itinerant electron associated with the t_{2g} band of the Mo has a spin antiferromagnetically coupled to the localized $S=5/2$ core spins on the Fe sites. In high fields, the ordinary Hall effect is

dominant and the data show a linear negative slope which indicates an electron-like behavior. Assuming naïve single band model negative slopes at magnetic field from 4 to 7 T gives a carrier density of 0.4, 0.6 and 4 electrons per f.u. for 10, 100 and 300K, respectively. This anomalous Hall behavior is also seen in $\text{Sr}_2\text{FeMoO}_6$ systems, where the origin of this anomalous Hall effect is believed to be induced by skew scattering.³⁹

In Figure 4-6, the SEM images of samples show grain-like structure in which the size of the features increases with increasing growth temperature. For films grown at 800 and 900°C, smaller particles with the size of tens of nanometer are observed, though there is no explicit second phase observed from the XRD results. They tend to be segregated in the boundary region for 900°C sample while they are located homogeneously all over the area for 800°C sample. The temperature dependence of resistivity might be induced by this microstructural change in part. It is consistent with the report that resistivity and magnetoresistance decreased with increasing grain size in $\text{Ba}_2\text{FeMoO}_6$ ceramics study.²² The coercive field increases with increasing growth temperature. However, Poddar *et al.* reported that the coercive field decreased with increasing grain size in polycrystalline $\text{Sr}_2\text{FeMoO}_6$.³⁷ This discrepancy suggests that the strain induced by the substrate can play a role in the properties of thin film double perovskite materials.

Summary and Conclusions

In summary, structural, magnetic and magneto-transport properties were investigated in $\text{Ba}_2\text{FeMoO}_6$ thin films grown by pulsed laser deposition. The grain size, the conductivity, the saturation magnetization and the coercive field all increase with increasing growth temperature, thus indicating that substrate temperatures on the order of 900°C during growth are a prerequisite for high quality films. Our observation that the

T_C of these films remains constant while magnetization and conductivity improve is consistent with previous experimental results⁹⁹ and recent theoretical notions¹⁴ that antisite disorder (i.e., exchange of Fe and Mo atoms) is responsible for diminished magnetic properties. Clearly, the attainment of higher quality double perovskite films will require precise stoichiometry, improved ordering on the B and B' sites and a comprehensive understanding of the role of substrate-induced strain.

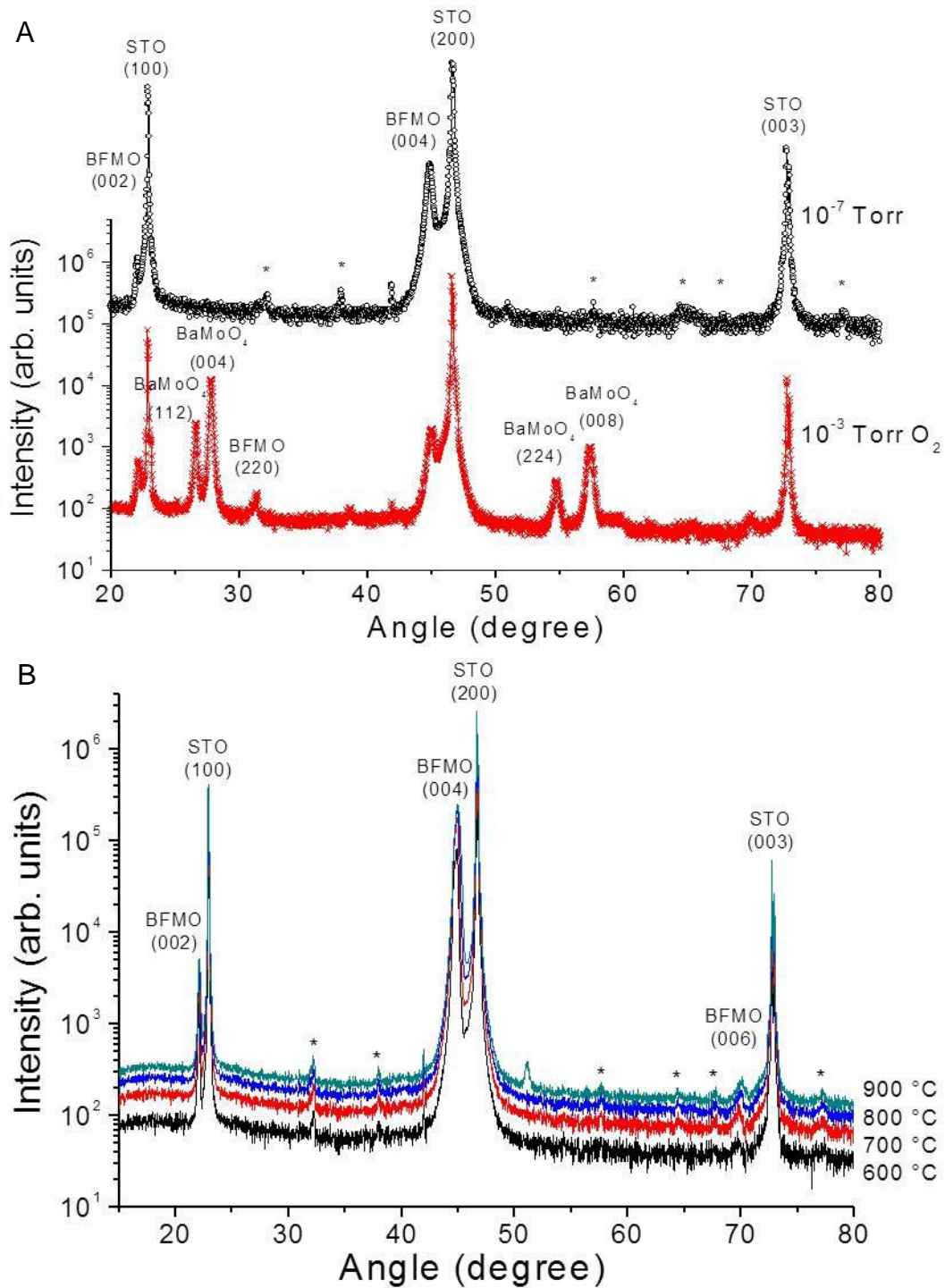


Figure 4-1. XRD patterns of $\text{Ba}_2\text{FeMoO}_6$ thin films. Images given for A) sample grown at 900°C under 10^{-7} Torr (without external gas feed-in) and 10^{-3} Torr O_2 and B) samples grown at $600\text{--}900^\circ\text{C}$ under 10^{-7} Torr. The peaks marked with asterisk (*) are from the XRD sample holder (which is not covered by 5×5 mm² samples). C) In-plane phi scan. D) Reciprocal space map of the sample grown at 700°C .

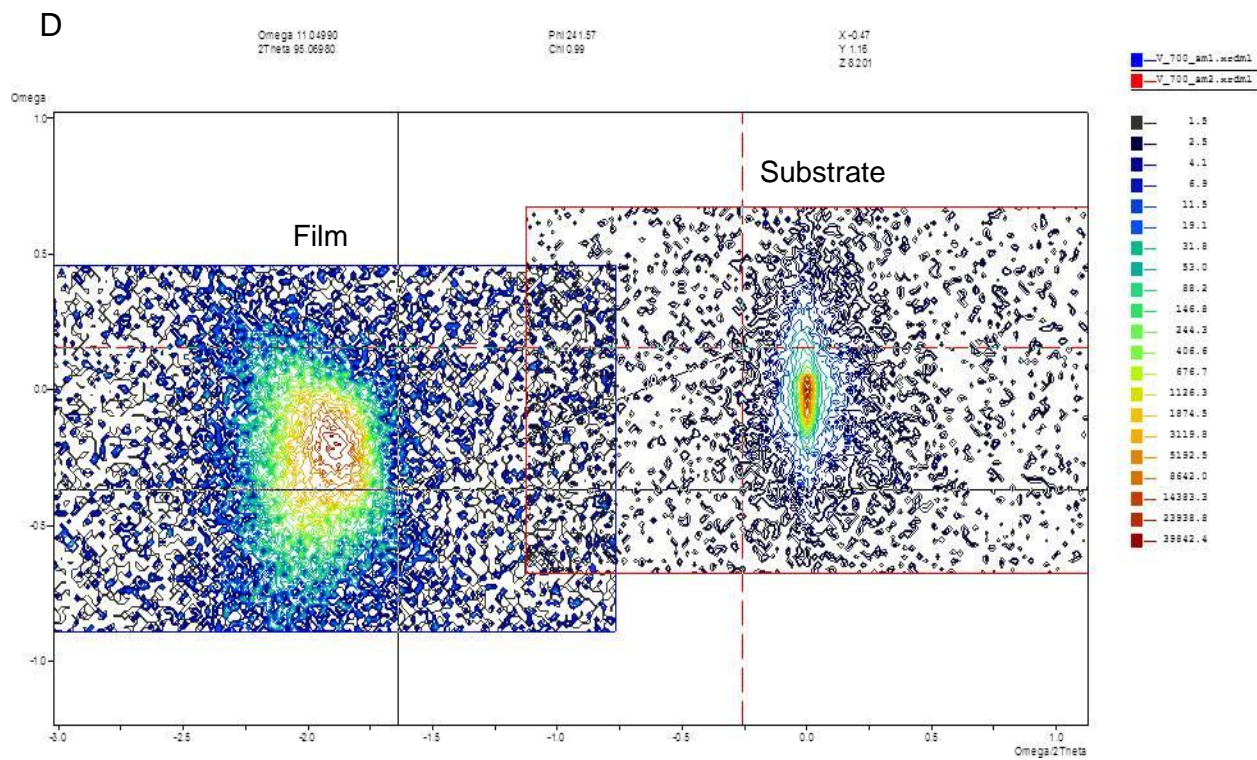
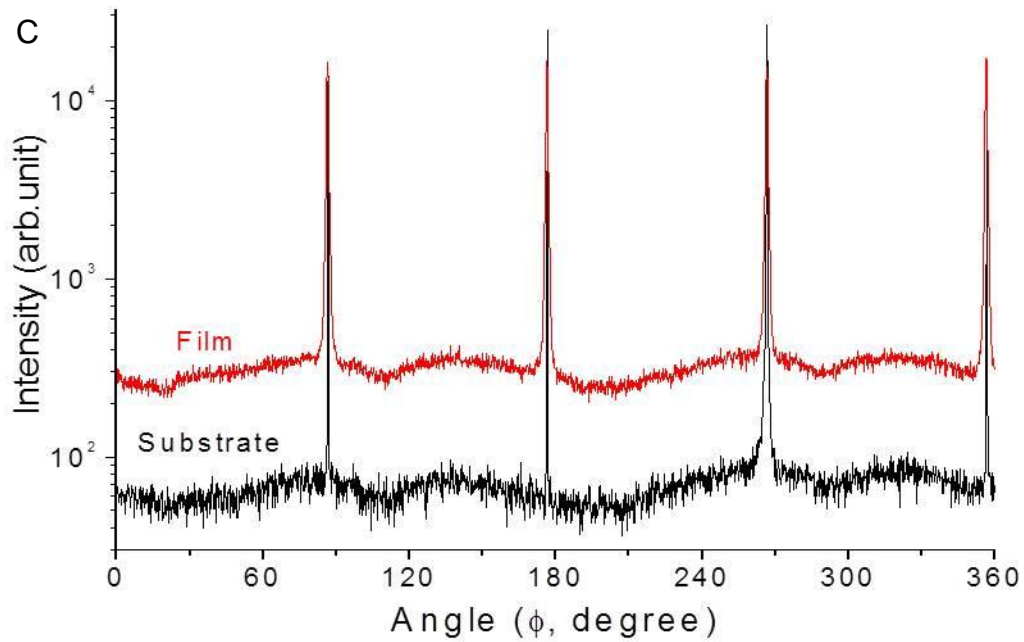


Figure 4-1. Continued

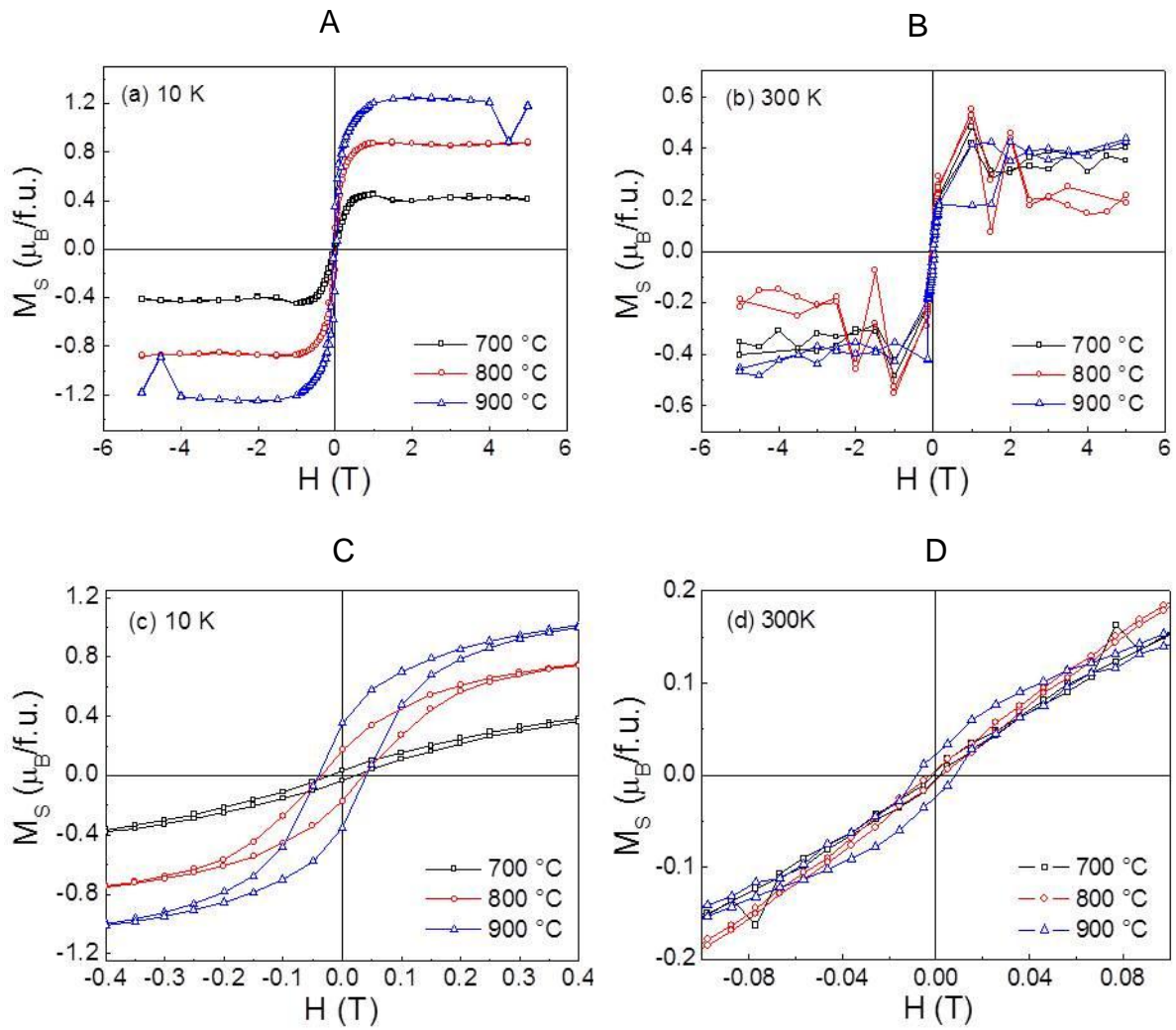


Figure 4-2. Magnetization curves of $\text{Ba}_2\text{FeMoO}_6$ thin films grown at 700-900°C. Images given for samples measured at A-B) 10K and C-D) 300 K.

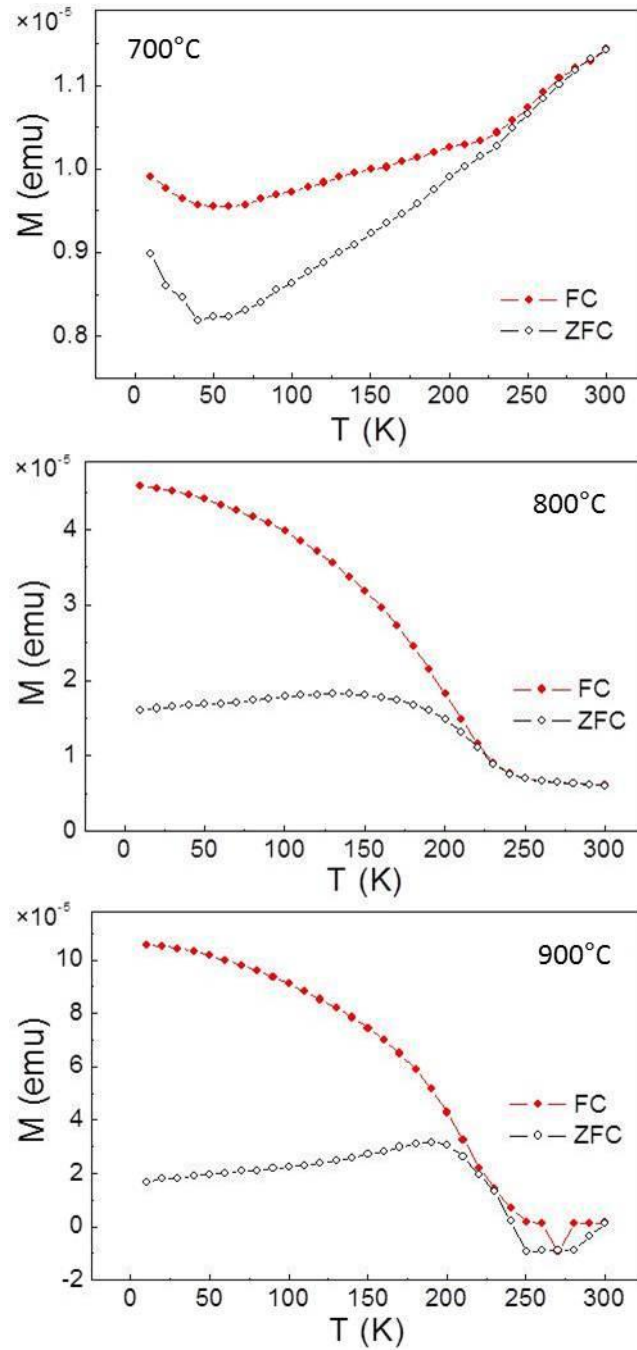


Figure 4-3. The temperature dependence of the magnetization of $\text{Ba}_2\text{FeMoO}_6$ thin films grown at temperatures indicated

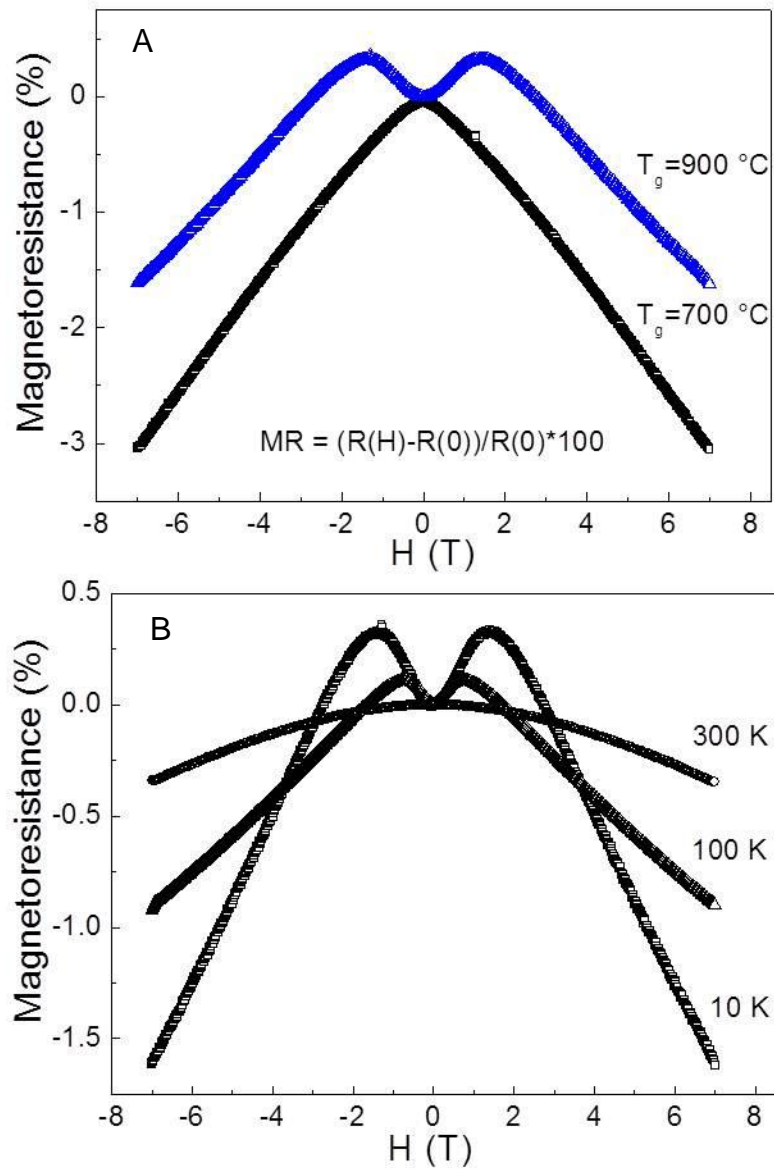


Figure 4-4. Magneto-resistance of $\text{Ba}_2\text{FeMoO}_6$ thin films. Images given for A) samples grown at 700 and 900 °C measured at 10K and B) sample grown at 900°C measured at temperatures indicated.

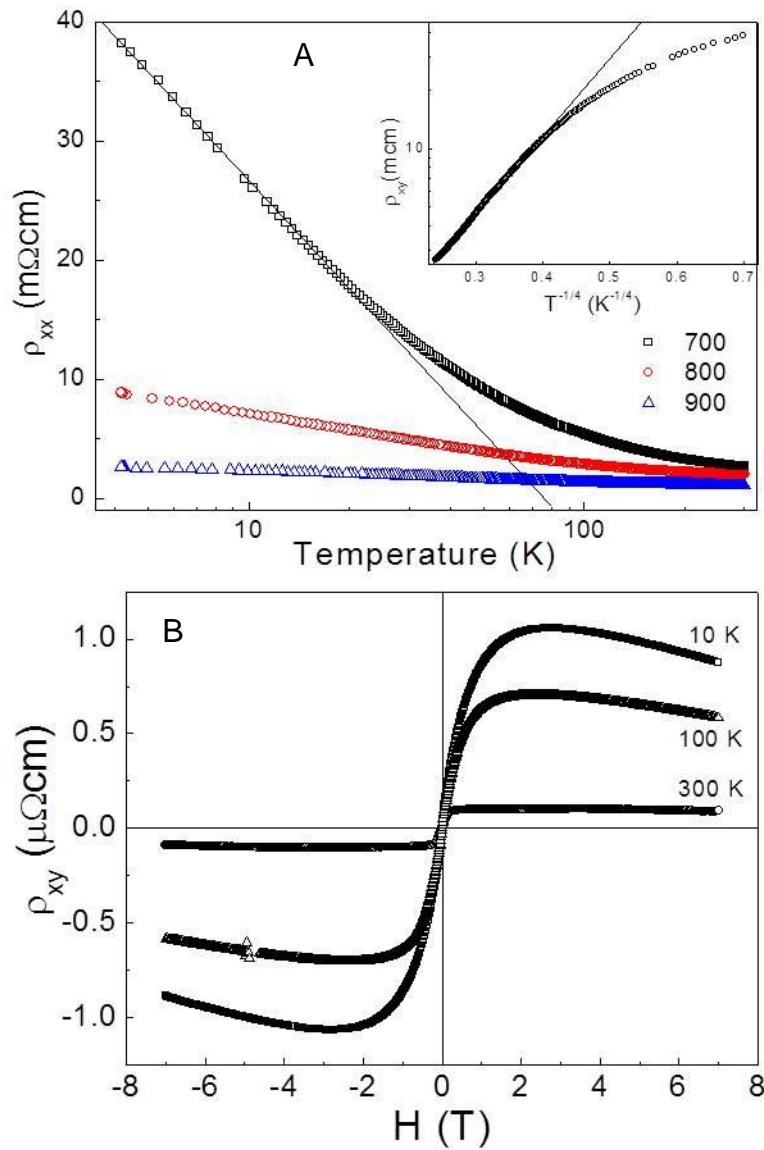


Figure 4-5. Transport properties of $\text{Ba}_2\text{FeMoO}_6$ thin films. Images given for A) resistivity of samples grown at 700-900°C and B) Hall resistivity of a sample grown at 900°C.

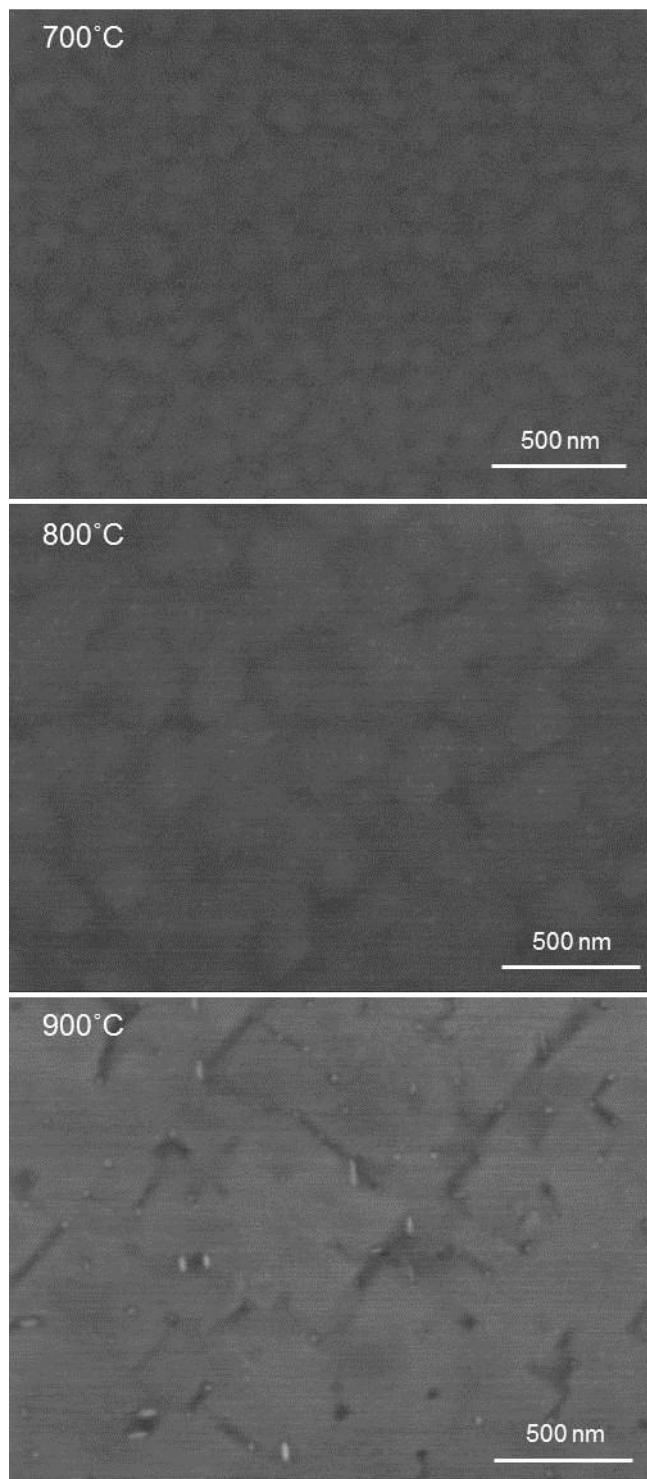


Figure 4-6. SEM images of the samples grown at 700 to 900°C

CHAPTER 5
THE EFFECTS OF OXYGEN PRESSURE ON THE PROPERTIES OF $\text{Ba}_2\text{FeMoO}_6$
THIN FILMS GROWN VIA PULSED LASER DEPOSITION

Introductory Remarks

Double perovskites (DPs) with the general formula $\text{A}_2\text{BB}'\text{O}_6$ comprise two interpenetrating simple perovskite (ABO_3) structures with a simple three-dimensional ordering of the B and B' cations. Double perovskites are known as a particular type of half metallic oxide with a fully polarized conduction band, which with Curie temperatures higher than room temperature are good candidates for applications that take advantage of the unusual magneto-transport and magnetic properties that are associated with various perovskite materials available for chemical modification.¹³ Double perovskites are remarkable materials with localized and itinerant ferromagnetism existing separately on the B and B' sublattices respectively.¹⁴ With the absence of both Jahn-Teller effects and antiferromagnetic superexchange due to increased distance between B-site cations, double perovskites also have higher Curie temperatures compared to manganites.¹⁴

Among the different types of double perovskites, $\text{Sr}_2\text{FeMoO}_6$ has been most studied since Kobayashi *et al.* reported that this half-metallic $\text{Sr}_2\text{FeMoO}_6$ remains as high spin polarized state above room temperature.¹² Clearly such materials are good candidates for device applications.^{19,20,38,93,94} A simulation study suggested that the defect-free $\text{Sr}_2\text{FeMoO}_6$ has a high T_C of 450K and a saturation magnetization of $4 \mu_B$ per formula unit (f.u.) at a low temperature with a long range antiferromagnetic ordering between the localized core spins on the Fe^{3+} sites and the itinerant spins on the Mo^{5+} sites.²⁰ However, the experimental values of a saturation magnetization have been

lower than $4 \mu_B/f.u.$ in most studies; achieving this value seems more challenging in thin film materials.

Ba_2FeMoO_6 is also a member of the double perovskite A_2FeMoO_6 ($A=Ba, Ca, Sr$) family and is reported to have a T_C as high as 367K.¹⁹ Even though Ba_2FeMoO_6 has attracted much less interest largely due to a lower T_C than Sr_2FeMoO_6 , there have been multiple reports of over 30% negative magneto-resistance for polycrystalline ceramic samples.^{22,44} However, to our knowledge there is no significant study on thin film Ba_2FeMoO_6 .

In the previous chapter, we discussed preparing epitaxial thin films under vacuum and examined structural, magnetic, and magneto-transport properties. In this chapter, we have deposited epitaxial Ba_2FeMoO_6 thin films under oxygen atmosphere and investigated the effect of oxygen pressure on the properties of thin films. We have found that the films prepared under a low oxygen pressure showed a high saturation magnetization value while the magneto-resistance was enhanced with higher oxygen pressure during deposition. Interestingly, an unusual positive magneto-resistance observed in the sample grown at a high temperature under vacuum disappeared by the addition of oxygen.

Experimental

We have prepared epitaxial Ba_2FeMoO_6 thin films on $SrTiO_3$ substrates by pulsed laser deposition with a stoichiometric target. The target was synthesized by a conventional solid state reaction under reducing atmosphere of H_2/Ar (5% Hydrogen mixture gas). The detailed procedures and properties of the target synthesized were described in the chapter 3.

The thin films were deposited at temperatures of 700 and 800°C for an hour. The base pressure of chamber was $\sim 10^{-9}$ Torr and the pressure during deposition was ranging from 0.1 to 10 mTorr of O₂/Ar (0.2% oxygen) mixture gas, corresponding to 2.0×10^{-7} to 2.0×10^{-5} Torr of oxygen partial pressure. The 248 nm wavelength KrF laser was utilized to ablate the ceramic target. The laser energy and the repetition rate were 1.5 J/cm² and 5 Hz, respectively. The growth rate is 0.2 Å per laser pulse.

The structural properties of the thin films were examined by powder and high resolution X-ray diffraction using Phillips APD3720 and four point X'pert MRD at MAIC facility. Magnetization, Hall effect, and magneto-transport were respectively measured using a Quantum Design Magnetic Properties Measurement System (MPMS) and Physics Properties Measurement System (PPMS). Also Auger Electron Spectroscopy (AES) was used to investigate the chemical properties.

Results and Discussion

Figure 5-1A shows the XRD patterns of the Ba₂FeMoO₆ thin films grown at 700°C under 0.1 to 10 mTorr of O₂/Ar mixture gas. All films were phase pure and oriented along the *c*-directions in which the (00*l*) peaks of films were observed next to the (00*m*) peaks of SrTiO₃ substrate. An unidentified peak around 32 degree is overlapped with one of the peaks from the sample holder for XRD measurement due to small sample size of 5x5 mm². As it is not matched with any peak positions of possible impurities such as BaMoO₄ or Fe₃O₄, which are most likely to form under a high oxygen pressure, it is believed to be originated from the substrate holder with unusually high intensity for the sample grown at 10 mTorr.

In Figure 5-1B, the (004) peak of films were observed to shift toward a high angle, i.e., small lattice spacing with increasing oxygen pressure. For the sample grown under

10 mTorr, the peak showed broadening and spitting which might be due to phase segregation of Fe- and Mo-rich phases in the film and in turn can lead to degradation of magnetic properties. Figure 5-1C shows the (004) and (642) peaks of the samples grown at 700°C under 0.1 and 10 mTorr. The *a*- and *c*-lattice parameters obtained from (004) and (642) peak positions are 8.120 and 8.176 Å and 8.066 and 8.082 Å for 0.1 and 10 mTorr samples, respectively. Both samples are elongated along *c*-direction by strain induced by substrate of smaller lattice spacing (3.905 Å).

This change in lattice parameter is believed to be induced by compositional variations under different oxygen partial pressure during deposition. Sr₂FeMoO₆ thin film has shown a high sensitivity to oxygen pressure as low as 10⁻⁶ to 10⁻⁴ Torr.⁹⁴ The lattice parameter have been reported to be affected by oxygen content in the sub-structural BaFeO₃ and BaMoO₃ as well as the double perovskite SrFeMoO₆.^{38,96-98} The other possible chemical modulation is a change in ratio of cations (Ba:Fe:Mo), especially in B-site cations. Due to the different lattice sizes of BaFeO₃ (4.02 Å) and BaMoO₃ (4.04 Å), antisite defects, i.e., exchange of Fe and Mo atoms and phase segregations can lead to the lattice parameter change.

Auger electron spectroscopy (AES) was used to measure the chemical compositions for samples grown at 700°C. The compositions obtained by AES were summarized in Table 5-1. It should be noted that the surface state of a sample can affect significantly the intensity of the peak for each element and the sensitivity factor of each element can change the results. However, the relative amounts of cations with varying growth condition can provide important aspects of how the oxygen pressure influences the film property. The Fe:Mo ratio is larger for the 10 mTorr sample than the

0.1 mTorr sample and this increased off-stoichiometry is believed to be responsible for degraded magnetic properties of the samples under high oxygen pressure. The values of Fe:Mo ratio are larger than the ideal ratio of one, which might be the crucial factor for the low saturation magnetization.^{36,43} Due to the limitation of the measurement mentioned above, the comparative quantitative characterization is further required to confirm the chemical composition.

The magnetization curves measured at 10 and 300K were plotted in Figure 5-2. At both growth temperatures, the saturation magnetization (M_S) decreased with increasing oxygen pressure during deposition and they are about 0.6, 0.4, and 0.1 μ_B /f.u. for 0.1, 1, 10 mTorr samples, respectively. But there is no significant change in M_S with the measurement temperature, which is consistent with the result of temperature dependent magnetizations shown in Figure 5-3. It shows that all films grown at 700°C have a Curie temperature higher than 300K. In contrast, the films grown at 800°C show increased T_c in the one grown under higher oxygen pressure. At 10K, the samples grown under 1 mTorr has smaller coercive field than the samples grown under 0.1 and 10 mTorr which have almost the same values. The coercive field was diminished at 300K for all samples. This effect, namely the smaller coercive value at a specific pressure and increasing with oxygen pressure, is also observed in the samples grown at 800°C. The film grown under 0.5 mTorr has a smaller coercive field than the films grown under vacuum and 5 mTorr.

Figure 5-4 shows the magneto-resistance of the samples grown at 700 and 800°C. All samples show typical negative magneto-resistance at 700°C. The magneto-resistance increased with increasing oxygen pressure, which interestingly showed the

opposite tendency to the saturation magnetization. The saturation magnetization and magneto-resistance are the two characteristics used most commonly to evaluate this double perovskite oxide material. Most studies have shown that those two properties show the same tendency with the processing conditions which are believed to affect stoichiometry and disordering. Thus, the changes in magnetization and magneto-resistance observed above suggest that there is another factor other than stoichiometry and disordering, which is dependent on the oxygen pressure during deposition.

The increase of magneto-resistance with increasing oxygen pressure was observed in the samples grown at 800°C. Interestingly, the positive portion observed in the sample grown under vacuum disappeared in the samples grown under oxygen atmosphere. This positive portion under small field which was reported in dilute magnetic semiconductor of (Ga,Mn)As is not clearly understood.¹⁰⁰ The partial pressure of oxygen is as low as 1×10^{-6} Torr for 0.5 mTorr of O₂/Ar mixture gas and it clearly shows the high sensitivity of this material to oxygen. This sensitivity suggests that the positive magneto-resistance might be associated with oxygen related defects. A closer look at the graph in the small field range gives more detailed changes. First, when a magnetic field is applied, the samples show a sharp decrease (up to 1 kOe) and a small plateau appears (1 to 2 kOe) for all samples. The differences emerge after this point. Samples grown under oxygen showed an ordinary negative MR under increased applied field. In contrast, the sample grown under vacuum has extended plateau up to 4 kOe and started to increase until reaching a maximum around 15 kOe.

The resistivity and Hall resistivity are plotted in Figure 5-5. The resistivity increases with increasing oxygen pressure and a large dependence on temperature is observed

from the sample grown under 10 mTorr. The temperature dependence of resistivity is similar to that of films grown under vacuum, in which a conduction mechanism change is observed with temperature. Interestingly, it reflects correlation between resistivity and magneto-resistance. The sample grown under 10 mTorr shows a higher resistivity and magneto-resistance than the samples grown under 0.1 and 1 mTorr.

In ferromagnetic materials, the transverse resistivity is given by

$$\rho_{xy} = R_H B + R_A \mu_0 M,$$

with the magnetization M and the ordinary and anomalous Hall coefficients R_H and R_A , respectively.¹⁰⁴ The Hall resistivity is measured at 300K under an applied magnetic field up to 7 T and shown in Figure 5-5B. An anomalous Hall effect is observed in all samples. In low magnetic fields, the Hall resistivity is dominated by the anomalous Hall contribution which behaves hole-like as indicated by the positive slope. This positive sign arises because the single itinerant electron associated with the t_{2g} band of the Mo has a spin antiferromagnetically coupled to the localized $S=5/2$ core spins on the Fe sites. In high fields, the ordinary Hall effect is dominant and the data show a linear negative slope which indicates an electron-like behavior. The anomalous portion is suppressed in the film grown under high oxygen pressure due to low magnetization (in the second term of equation, $R_A \mu_0 M$). This anomalous Hall behavior is also seen in $\text{Sr}_2\text{FeMoO}_6$ systems, where the origin of this anomalous Hall effect is believed to be induced by skew scattering.³⁹

Summary and Conclusions

In summary, the structure and magnetic properties were investigated in $\text{Ba}_2\text{FeMoO}_6$ thin films grown by pulsed laser deposition, focusing on the effects of oxygen pressure during deposition. The saturation magnetization decreases with

increasing oxygen pressure while magneto-resistance was enhanced by higher oxygen pressure. This opposite tendency of magnetization and magneto-resistance is unusual in this double perovskite. As it cannot be explained by the stoichiometry and disordering, oxygen related defects are believed to be responsible for the odd behaviors of the samples. Disappearance of positive magneto-resistance even with very low oxygen partial pressure during deposition reflects the high sensitive of this double perovskite to oxygen, which is another hint of existence of oxygen related defects.

Table 5-1. Compositions of Ba₂FeMoO₆ thin films grown at 700°C under 0.1 and 10 mTorr by Auger Electron Spectroscopy

| | Sample | Ba | Fe | Mo | O | Fe/Mo |
|-----------|------------------|-------|-------|------|-------|-------|
| 0.1 mTorr | As grown | 36.97 | 13.60 | 5.38 | 44.05 | 2.53 |
| | sputtered 30 sec | 39.28 | 16.35 | 6.30 | 38.07 | 2.60 |
| 10 mTorr | As grown | 35.65 | 18.52 | 6.13 | 39.69 | 3.02 |
| | sputtered 30 sec | 39.92 | 24.39 | 7.19 | 28.50 | 3.39 |

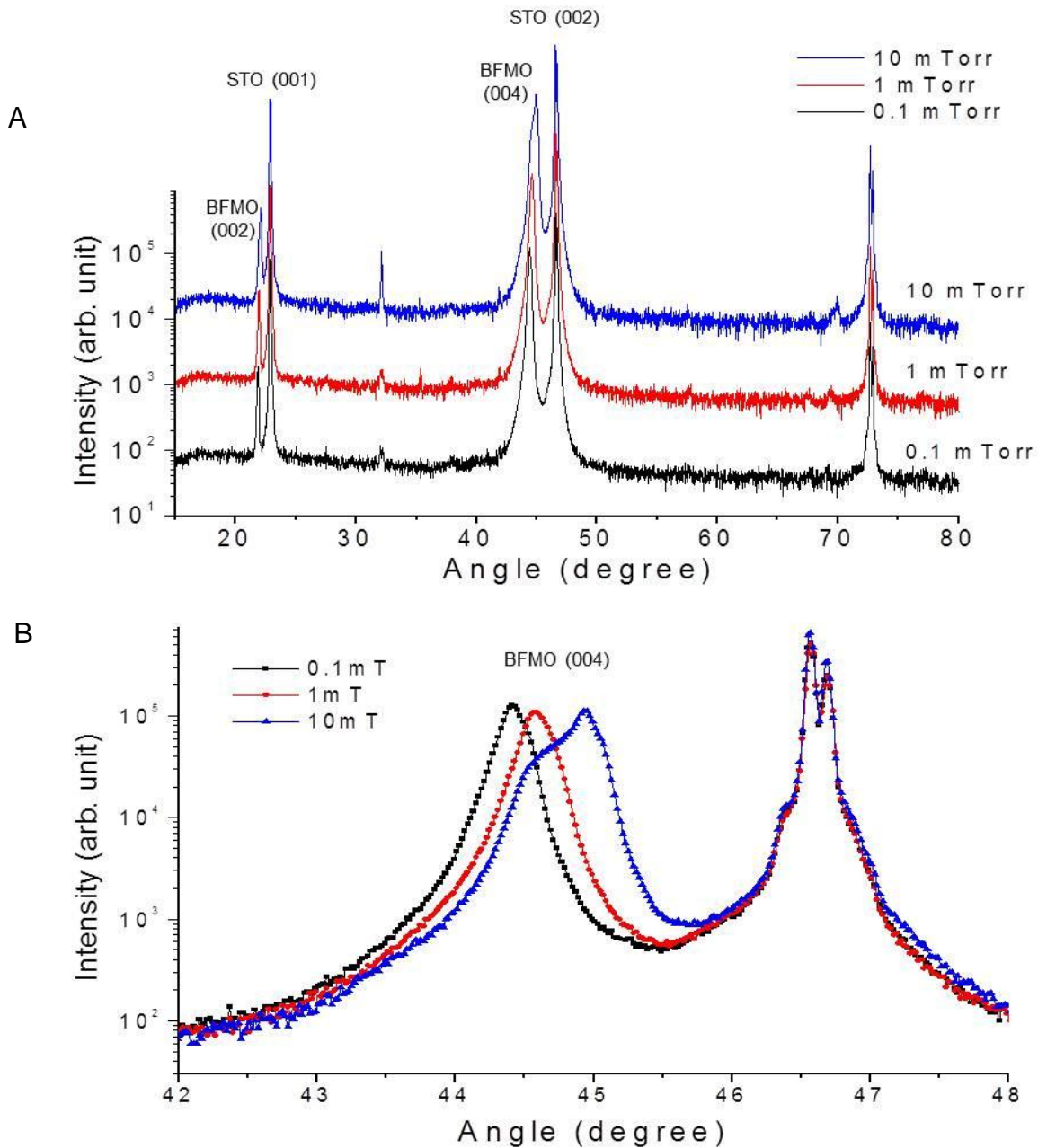


Figure 5-1. XRD patterns of $\text{Ba}_2\text{FeMoO}_6$ thin films grown at 700°C under 0.1 to 10 mTorr O_2/Ar mixture gas. Images given for A) scanned from 20 to 80 degree and B) (004) peaks of samples. C) Omega-rocking curves of (004) peaks.D) (642) peaks in theta-2theta scan

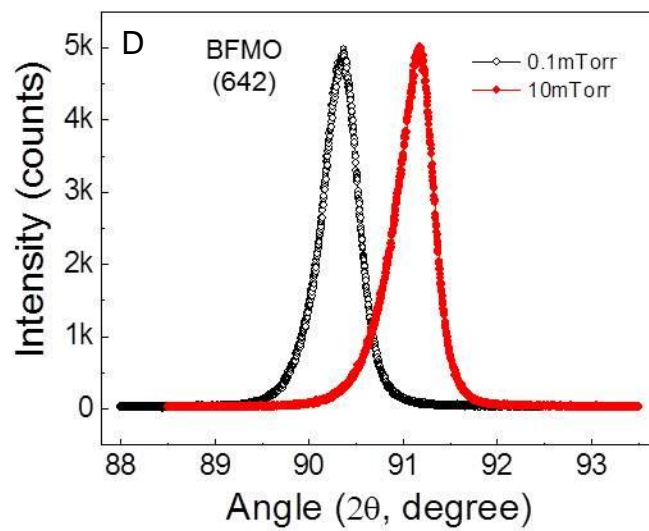
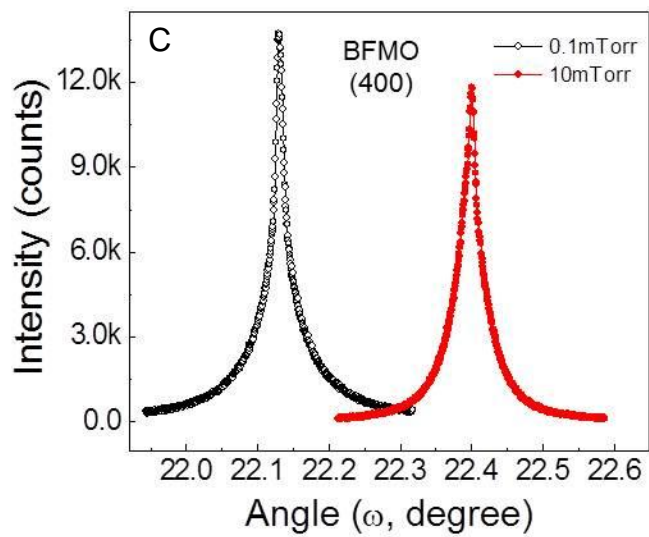


Figure 5-1. Continued

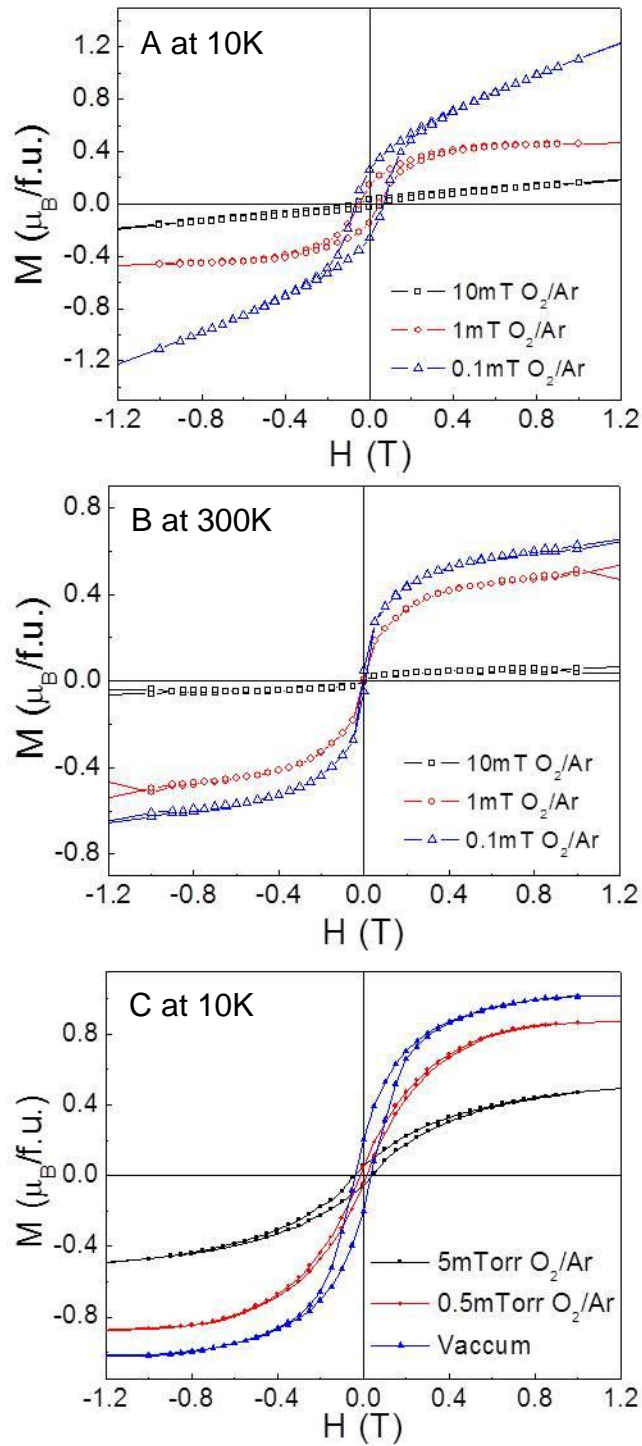


Figure 5-2. Magnetization curves of Ba_2FeMoO_6 thin films. Images given for samples grown at A-B) 700°C and C-D) 800°C measured at temperatures indicated.

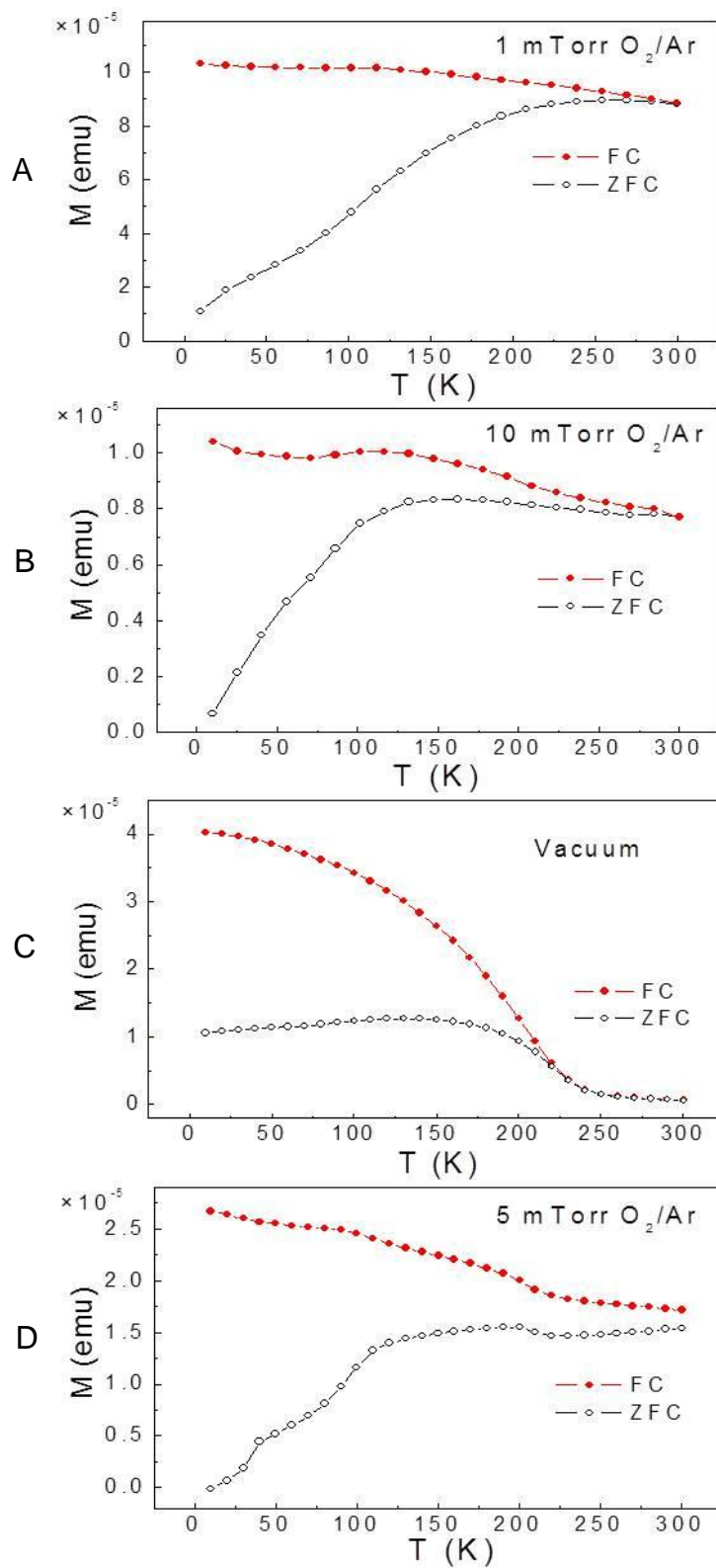


Figure 5-3. The temperature dependence of the magnetization of $\text{Ba}_2\text{FeMoO}_6$ thin films. Images given for samples grown at A-B) 700°C and C-D) 800°C.

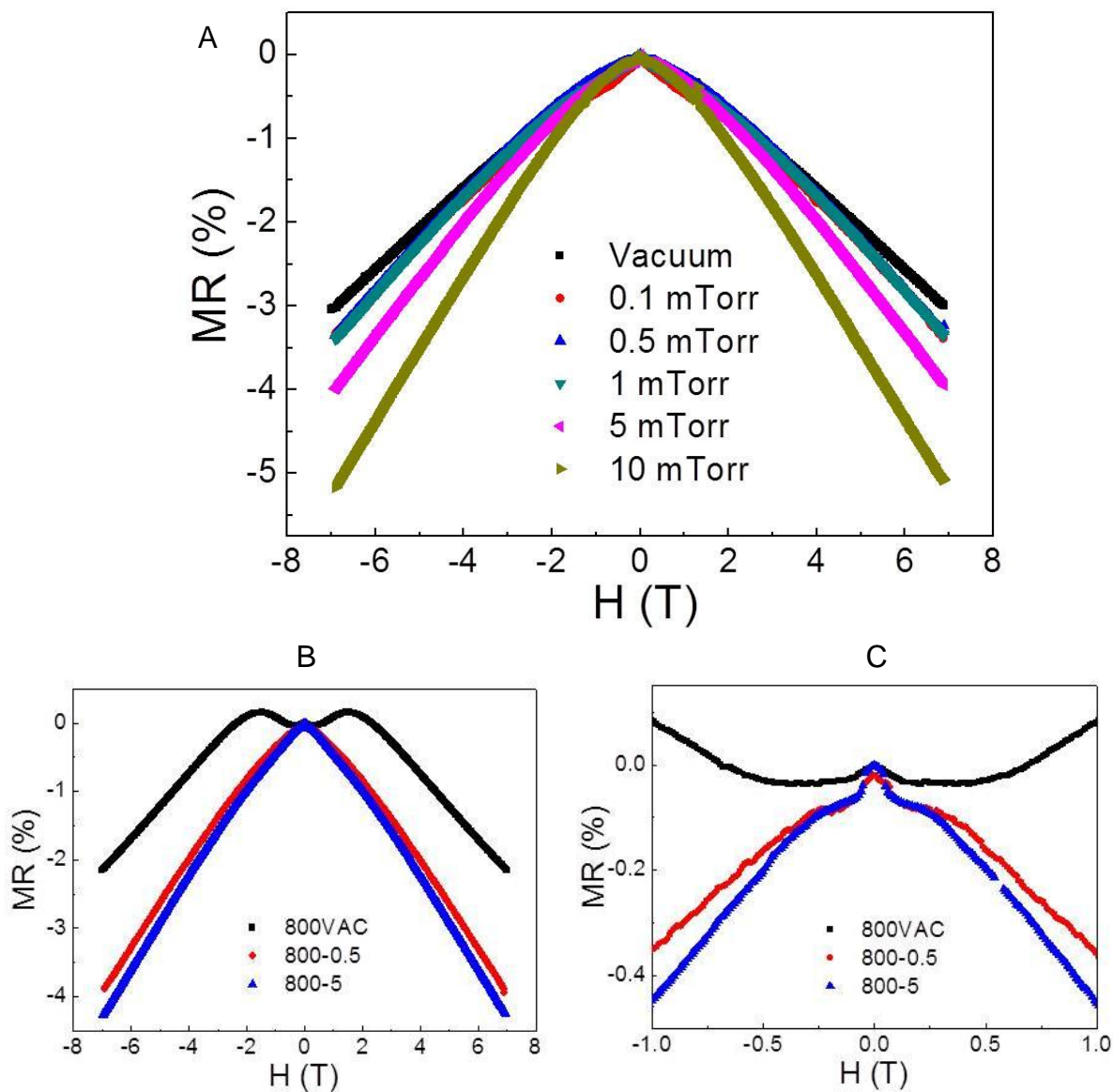


Figure 5-4. Magneto-resistance of Ba_2FeMoO_6 thin films grown at the oxygen pressures indicated and measured at 10K. Images given for samples grown at A) 700°C and B-C) 800°C.

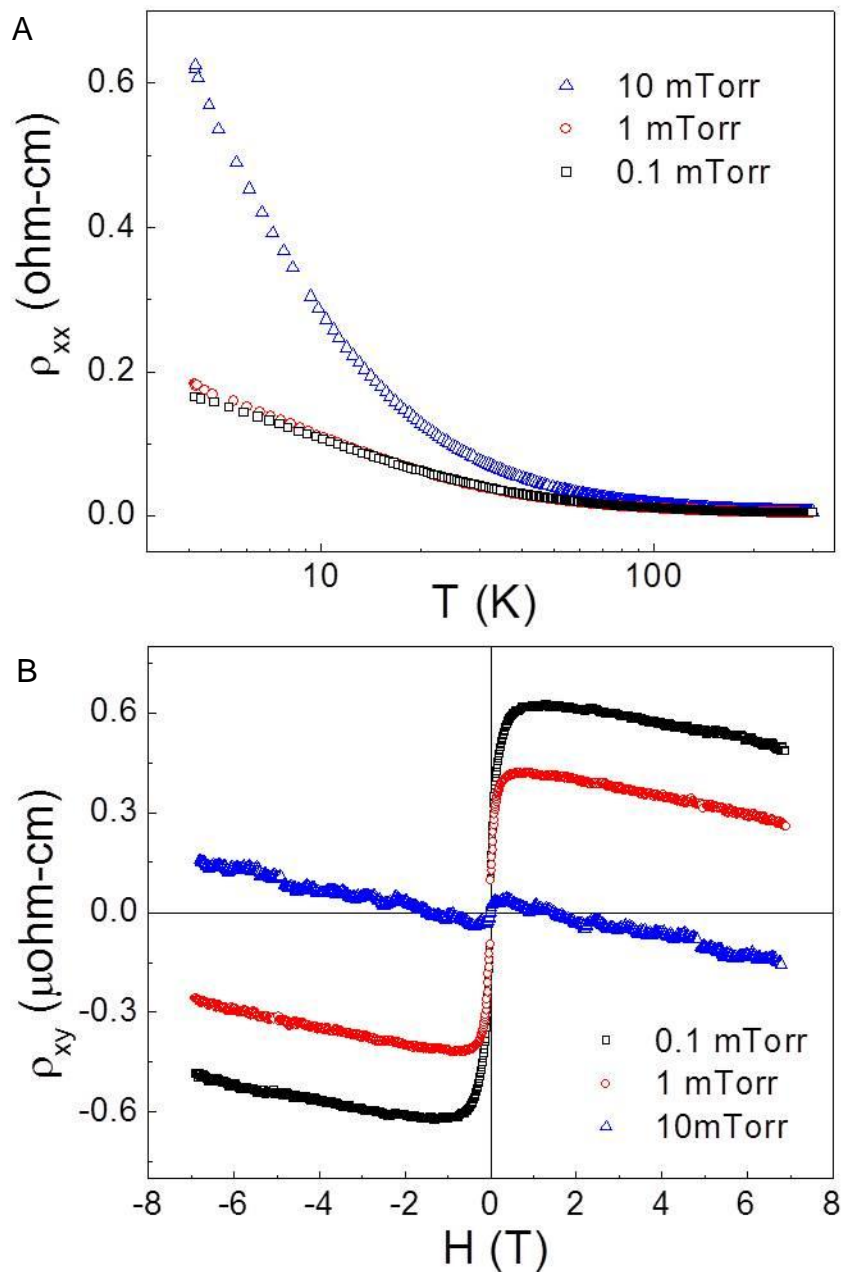


Figure 5-5. Transport properties of $\text{Ba}_2\text{FeMoO}_6$ thin films grown at 700°C under varying oxygen pressure indicated and measured at 300 K. Images given for A) resistivity and B) Hall resistivity.

CHAPTER 6
STRAIN INDUCED ENHANCEMENT OF MAGNETIZATION IN Ba₂FeMoO₆ BASED
HETEROSTRUCTURES WITH (Ba,Sr)TiO₃

Introductory Remarks

Multiferroics, especially ferroelectric ferromagnets, have attracted significant interest due to novel phenomena and the potential for various applications.^{49,50,59,68,70,105-109} As a limited number of single phase multiferroic materials exists due to the mutually exclusive nature of orbital structures required for ferroelectricity and ferromagnetism,⁶¹ horizontal or vertical hetero-structures have been explored as an alternative way to achieve the multiferroic property.⁷⁰

Since Kobayashi *et al.* reported that the half-metallic double perovskite Sr₂FeMoO₆ remains as high spin polarized state at a room temperature due to its high T_C up to 420K, this material has been of interest for its spin-polarized transport properties and considered as a good candidate for spintronics application.^{12,19,20,38,93,94} A simulation study suggested that the defect-free Sr₂FeMoO₆ can have the high T_C of 450K and the saturation magnetization of 4 μ_B per formula unit (f.u.) at a low temperature with antiferromagnetic ordering among Fe³⁺ ions and Mo⁵⁺ ions.²⁰

Ba₂FeMoO₆ is a member of the double perovskite A₂FeMoO₆ (A=Ba, Ca, Sr) family and reported to have T_C as high as 367K.¹⁹ Even though Ba₂FeMoO₆ has attracted much less interest mainly due to lower T_C than Sr₂FeMoO₆, there have been multiple reports of over 30% negative magneto-resistance for polycrystalline ceramic samples.^{22,44} However, the thin film studies of this material have not been done much. In previous chapters, we have prepared epitaxial thin film Ba₂FeMoO₆ under various growth conditions and investigated the magnetic and magneto-transport properties of the thin films. In this chapter, we prepared hetero-epitaxial multilayers of Ba₂FeMoO₆

with ferroelectric (Ba,Sr)TiO₃ on SrTiO₃ substrate by pulsed laser deposition and investigated their magnetic and magneto-electric properties, focusing on the effect of strain induced by different coupling layers and in different hetero-structures.

Experimental

Ba₂FeMoO₆ thin film and hetero-structures with Ba_{1-x}Sr_xTiO₃ (x=0 and 0.5) were synthesized on SrTiO₃ substrates by multiple target pulsed laser deposition. The targets were synthesized by a conventional solid state reaction with high purity (99.99% or higher) powders of BaCO₃, Fe₂O₃, MoO₃, BaTiO₃ and SrTiO₃. The detailed procedure for target fabrication and analysis on the powders were explained in chapter 3.

All samples were deposited at 700°C under 0.5 mTorr O₂/Ar (0.2% oxygen) mixture gas. In case of the Ba₂FeMoO₆/Ba_{1-x}Sr_xTiO₃ superlattices (SLs), five layers of double perovskite Ba₂FeMoO₆ were coupled with BaTiO₃, Ba_{0.5}Sr_{0.5}TiO₃ of 20 layers and 25 pairs of the structure were repeated. Also, bilayer (BL) structures of BaTiO₃ on Ba₂FeMoO₆ and Ba_{0.5}Sr_{0.5}TiO₃ on Ba₂FeMoO₆ were deposited to compare the effect of strain induced in the different multilayer structures. The volume of Ba₂FeMoO₆ layer was kept the same for all structures to exclude the dependency of magnetization on volume. The 248 nm wavelength KrF laser was utilized to ablate the ceramic target. The laser energy and the repetition rate were 1.5 J/cm² and 2 Hz, respectively. The growth rate is around 0.2 for Ba₂FeMoO₆ and Å for BaTiO₃ and Ba_{0.5}Sr_{0.5}TiO₃.

The crystal structure, phase of the thin film, superlattices and bilayers were examined by X-ray diffraction (Phillips APD3720). Also the periodicities of superlattices were obtained from the X-ray diffraction. Magnetization and magneto-transport were respectively measured using a Quantum Design Magnetic Properties Measurement System (MPMS) and Physics Properties Measurement System (PPMS).

Results and Discussion

Figure 6-1A shows the XRD patterns of $\text{Ba}_2\text{FeMoO}_6$ thin film, $\text{Ba}_{0.5}\text{Sr}_{0.5}\text{TiO}_3$ on $\text{Ba}_2\text{FeMoO}_6$ bilayer, and $\text{Ba}_2\text{FeMoO}_6/\text{Ba}_{0.5}\text{Sr}_{0.5}\text{TiO}_3$ superlattice. Satellite peaks of a superlattice next to (00 l) peaks of the SrTiO_3 substrate clearly showed the superlattice structure. A close look at the area around (002) peak of the substrate revealed the structural differences among three different structures. $\text{Ba}_{0.5}\text{Sr}_{0.5}\text{TiO}_3$ on $\text{Ba}_2\text{FeMoO}_6$ bilayer showed two separate peaks for $\text{Ba}_2\text{FeMoO}_6$ (004) and $\text{Ba}_{0.5}\text{Sr}_{0.5}\text{TiO}_3$ (002) while only $\text{Ba}_2\text{FeMoO}_6$ (004) peak was observed for the thin film. In addition, the (004) peaks that shifted to higher angle from thin film to bilayer to superlattice indicate the strained state of $\text{Ba}_2\text{FeMoO}_6$ layer in hetero-structures, more in the superlattice, compared to the bilayer.

Figure 6-1C and D show the (004) peaks of bilayers and superlattices. In case of bilayers, only one peak was observed for BaTiO_3 on $\text{Ba}_2\text{FeMoO}_6$ bilayer due to very similar lattice parameters of BaTiO_3 (4.002 Å) on $\text{Ba}_2\text{FeMoO}_6$ (8.06 Å), while the two separate peaks were observed for $\text{Ba}_{0.5}\text{Sr}_{0.5}\text{TiO}_3$ (002) and $\text{Ba}_2\text{FeMoO}_6$ (004). Also the higher peak intensity of BaTiO_3 on $\text{Ba}_2\text{FeMoO}_6$ bilayer suggests the overlapped peaks of lattice matching layers (it's plotted in the log scale). However, (004) peak of $\text{Ba}_2\text{FeMoO}_6$ layer in the two bilayers have the same position, which suggests that strain induced in the bilayer is limited only at the interface area and there's not a significant dependence on the top layer. In contrast, (004) peak of $\text{Ba}_2\text{FeMoO}_6/\text{Ba}_{0.5}\text{Sr}_{0.5}\text{TiO}_3$ superlattice clearly shifted more to a high angle than that of $\text{Ba}_2\text{FeMoO}_6/\text{BaTiO}_3$ superlattice, which suggests more strained state of $\text{Ba}_2\text{FeMoO}_6$ layer in the superlattice coupled with the layer with a smaller lattice parameter of $\text{Ba}_{0.5}\text{Sr}_{0.5}\text{TiO}_3$ (3.954 Å). Even with very similar lattice size of the two materials, $\text{Ba}_2\text{FeMoO}_6/\text{BaTiO}_3$ superlattice has

more shifted (004) peak for Ba₂FeMoO₆ layer than the bilayers. It clearly shows that superlattice structure can give more strain and bigger dependence on the lattice parameter of coupled layers.

The periodicity, Λ , of the superlattices was calculated using an equation

$$\Lambda = (L_i - L_j) \lambda / 2(\sin\theta_i - \sin\theta_j),$$

where, L_i and L_j are satellite peak indices, θ_i and θ_j are corresponding Bragg angles, and λ is the wavelength of an incident X-ray.¹¹⁰ And the results are shown in table 6-1. The periodicities obtained are 113 and 115 Å on average for Ba₂FeMoO₆/BaTiO₃ and Ba₂FeMoO₆/Ba_{0.5}Sr_{0.5}TiO₃ superlattice, respectively.

Figure 6-2 shows the magnetization curves of thin film, bilayers, and superlattices. In Figure 6-2A, at 10 K, the saturation magnetization (M_S) increased substantially for both superlattices and especially Ba₂FeMoO₆/Ba_{0.5}Sr_{0.5}TiO₃ superlattice showed a huge increase over 300% in M_S compared to the thin film. In contrast, BaTiO₃ on Ba₂FeMoO₆ bilayer remained similar to the thin film and Ba_{0.5}Sr_{0.5}TiO₃ on Ba₂FeMoO₆ bilayer showed decreased magnetization. This change of magnetization might be due to the strain induced in the hetero-structures. It is known that strain from substrate or in superlattice can enhance the magnetization.¹¹¹⁻¹¹³ Except the Ba_{0.5}Sr_{0.5}TiO₃ on Ba₂FeMoO₆ bilayer, the enhancement in magnetization has the same tendency with the amount of strain indicated by the peak shift in X-ray diffraction of hetero-structures.

As the strain from substrate SrTiO₃ is common to both bilayer samples, the interface at the top of Ba₂FeMoO₆ layer is believed to be responsible for the difference between the two bilayer samples. In the bilayer structures, the strain is limited only to layers at the interface and there is no difference in (004) peak positions of Ba₂FeMoO₆

layer in the two bilayers. The small difference of 0.7% in lattice parameters of $\text{Ba}_2\text{FeMoO}_6$ and BaTiO_3 is not expected to affect the magnetization much, which is consistent to the result that the magnetization curves for the bilayer and thin film are very similar throughout all the magnetic field. It is not clearly understood what suppressed the magnetization of $\text{Ba}_2\text{FeMoO}_6$ layer in the bilayer with $\text{Ba}_{0.5}\text{Sr}_{0.5}\text{TiO}_3$, although the lattice mismatch, 1.9%, is larger between two materials compared to the bilayer with BaTiO_3 . A coercive field decreased in superlattices while it remained almost the same for BaTiO_3 on $\text{Ba}_2\text{FeMoO}_6$ bilayer. Figure 6-2 C) shows the magnetization curves measured at 300K. Under small magnetic field, superlattices showed larger saturation magnetization (indicated by a steep slope) than thin film and BL samples. However, the data point got scattered as the magnetic field increased and so it is difficult to evaluate the magnetization exactly. The coercive field was diminished for all samples at room temperature.

In Figure 6-3, the temperature dependence of magnetization was shown in both field cooled (FC) and zero field cooled (ZFC) methods. In the zero field cooled method, a sample is cooled from room temperature without any applied magnetic field and then a small magnetic field of 100 Oe is applied at 10K. The magnetization is measured as a function of temperature during warm up under a constant field. In field cooled case, the sample is cooled from room temperature to 10K in an applied magnetic field and magnetization is measured during warm up. The curves show that $\text{Ba}_2\text{FeMoO}_6$ thin film has the Curie temperatures over 300K as it doesn't drop sharply up to a room temperature. In contrast, all superlattices and bilayers started to decrease from low temperatures (as low as) around 30K. Those graphs look similar in shape, but

interesting differences were observed in the irreversibility temperature (marked by the deviation between FC and ZFC curves). The temperature was lowest around 30K for $\text{Ba}_2\text{FeMoO}_6/\text{Ba}_{0.5}\text{Sr}_{0.5}\text{TiO}_3$ superlattice and got higher for $\text{Ba}_2\text{FeMoO}_6/\text{BaTiO}_3$ superlattice and BaTiO_3 on $\text{Ba}_2\text{FeMoO}_6$ bilayer. This tendency in this specific temperature is inversely proportional to the amount of strain in $\text{Ba}_2\text{FeMoO}_6$ layer induced by the coupled layer in SL and BL samples. Therefore, it is thought that the strain is responsible for the lowered Curie temperatures and different temperature dependency of magnetization in hetero-structures.

Figure 6-4 shows the magneto-resistance of the thin film and superlattice samples. The magnetoresistance increased slightly in $\text{Ba}_2\text{FeMoO}_6/\text{BaTiO}_3$ superlattice and remained almost same in $\text{Ba}_2\text{FeMoO}_6/\text{Ba}_{0.5}\text{Sr}_{0.5}\text{TiO}_3$ superlattice. Clearly, the magneto-resistance has not shown the same dependence on strain induced by coupling layers in superlattices to the M_S and T_C . Singh *et al.* reported the magneto-electric coupling depends on the layer and, in the study, only ferroelectric BaTiO_3 or $\text{Ba}_{0.5}\text{Sr}_{0.5}\text{TiO}_3$ enhanced the magneto-resistance in SLs with $(\text{La,Ca})\text{MnO}_3$ while paraelectric SrTiO_3 didn't enhance the magneto-resistance.¹¹⁴ Magneto-capacitance measurement is useful to check the coupling between magnetic and ferroelectric materials. However, it was difficult to investigate further because $\text{Ba}_2\text{FeMoO}_6$ is conductive as half-metal and even $\text{Ba}_{1-x}\text{Sr}_x\text{TiO}_3$ layer is not very insulating because of the growth condition of low oxygen partial pressure.

Summary and Conclusions

In summary, the structural, magnetic and magnetotransport properties were investigated in $\text{Ba}_2\text{FeMoO}_6$ thin film and heterostructures coupled with $\text{Ba}_{1-x}\text{Sr}_x\text{TiO}_3$ synthesized by pulsed laser deposition. The superlattice structure was confirmed by

XRD analysis of satellite peaks and the relative amount of strain in $\text{Ba}_2\text{FeMoO}_6$ layer was observed by the peak shift. The strain induced enhancement of magnetization was observed in superlattice samples in contrast to the bilayer samples which showed no enhancement or even suppression. The Curie temperatures decreases significantly in all the heterostructures and the decrease showed the same tendency with the strain in $\text{Ba}_2\text{FeMoO}_6$ layer induced by coupled layers.

Table 6-1. Periodicities of the superlattices calculated from positions of the satellite peaks around (002) peak of Ba₂FeMoO₆ in Figure 6-1E

| Satellite peak index | BFMO/BTO SL | | BFMO/BSTO SL | |
|----------------------|------------------------|-----------------|------------------------|-----------------|
| | peak position (degree) | Periodicity (Å) | peak position (degree) | Periodicity (Å) |
| -2 | 20.49 | | 20.61 | |
| -1 | 21.27 | 115.1 | 21.41 | 112.2 |
| 0 | 22.09 | 109.6 | 22.19 | 115.2 |
| +1 | 22.91 | 109.7 | 22.97 | 115.4 |
| +2 | 23.67 | 118.6 | 23.75 | 115.5 |

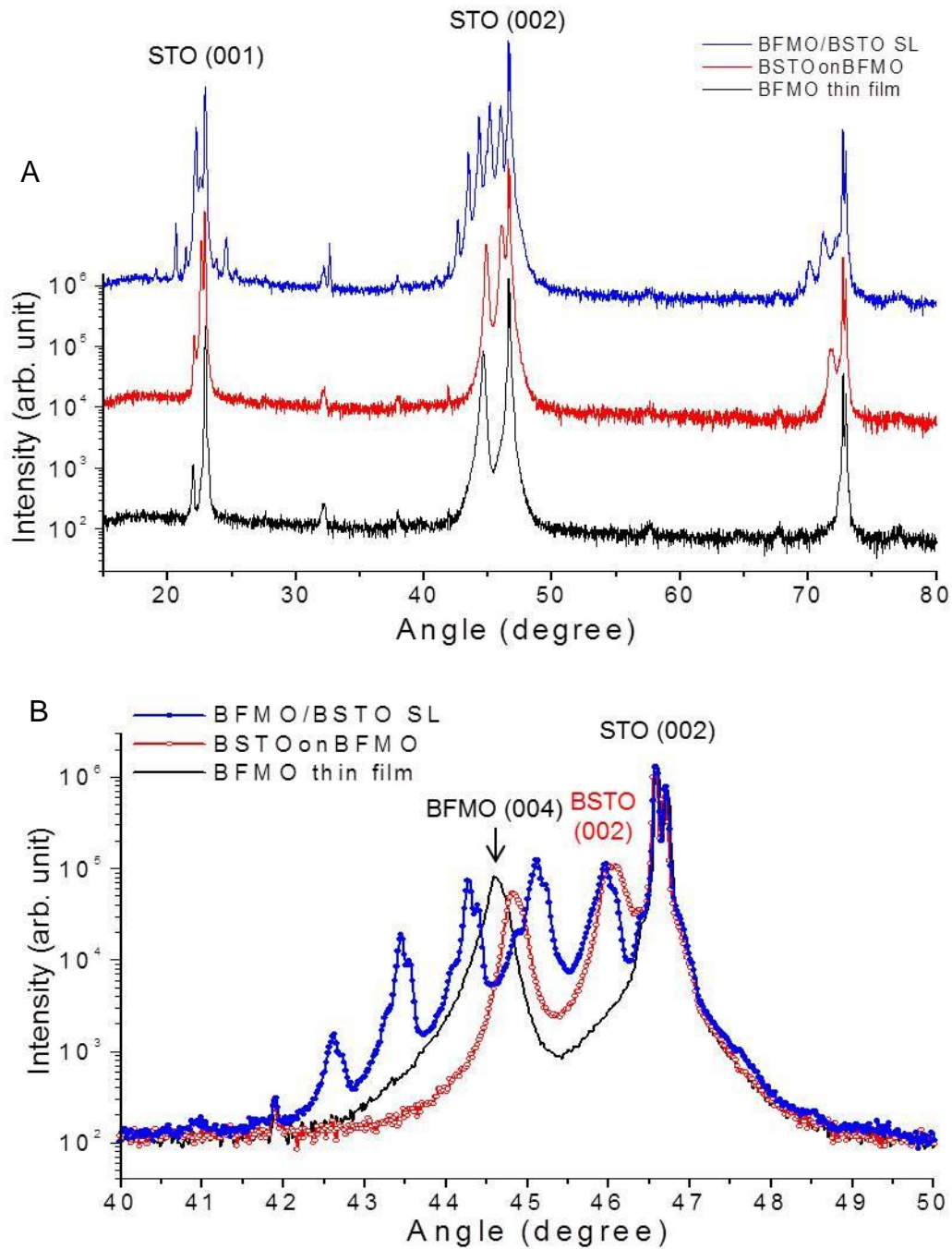


Figure 6-1. XRD patterns of $\text{Ba}_2\text{FeMoO}_6$ thin film and heterostructures. Images given for A) θ - 2θ scan, B) (004) peaks of A), C) (004) peaks of bilayers, D) superlattices, and E) satellite peaks around (002) peak of $\text{Ba}_2\text{FeMoO}_6$ in the superlattices.

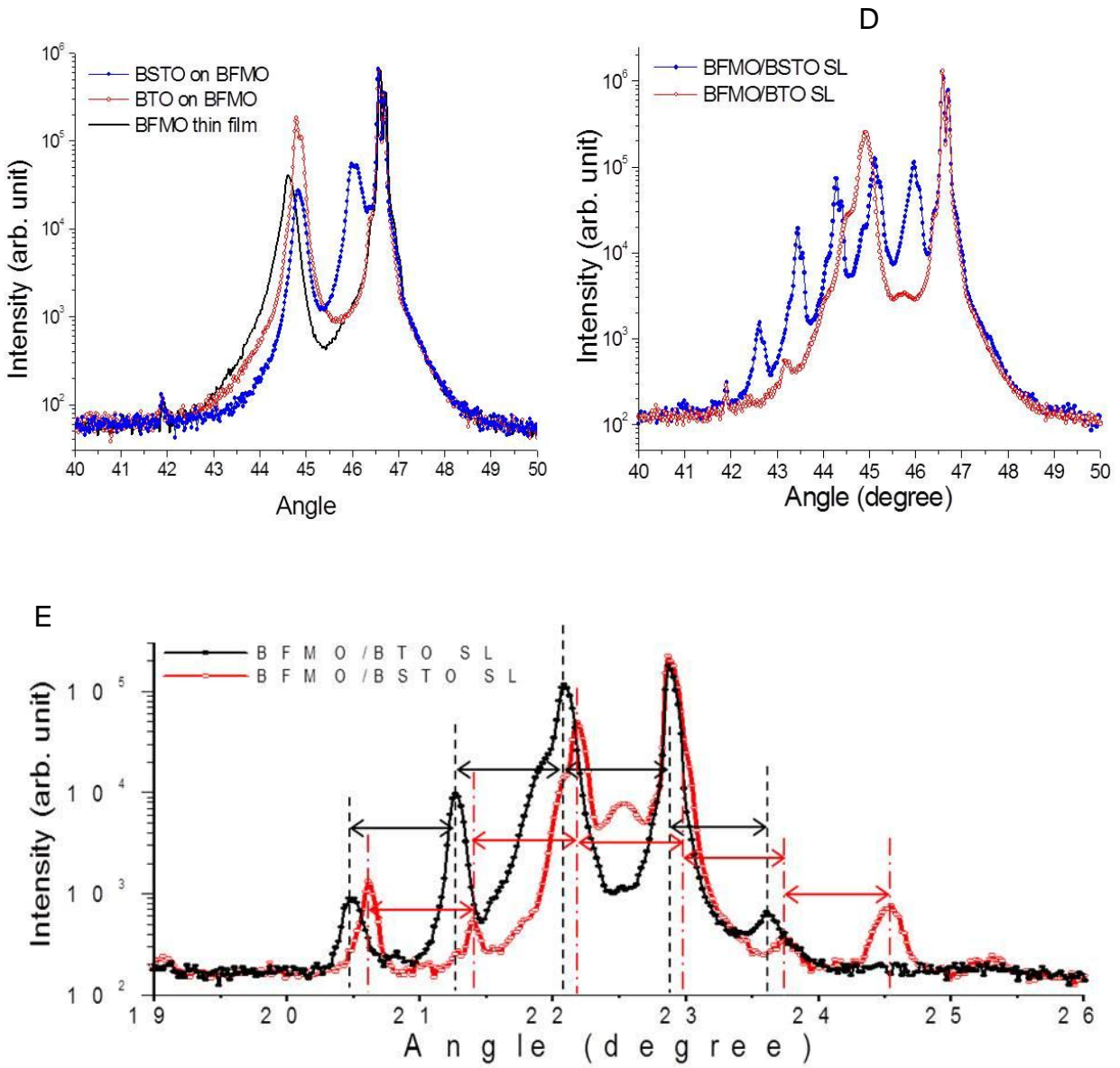


Figure 6-1. Continued

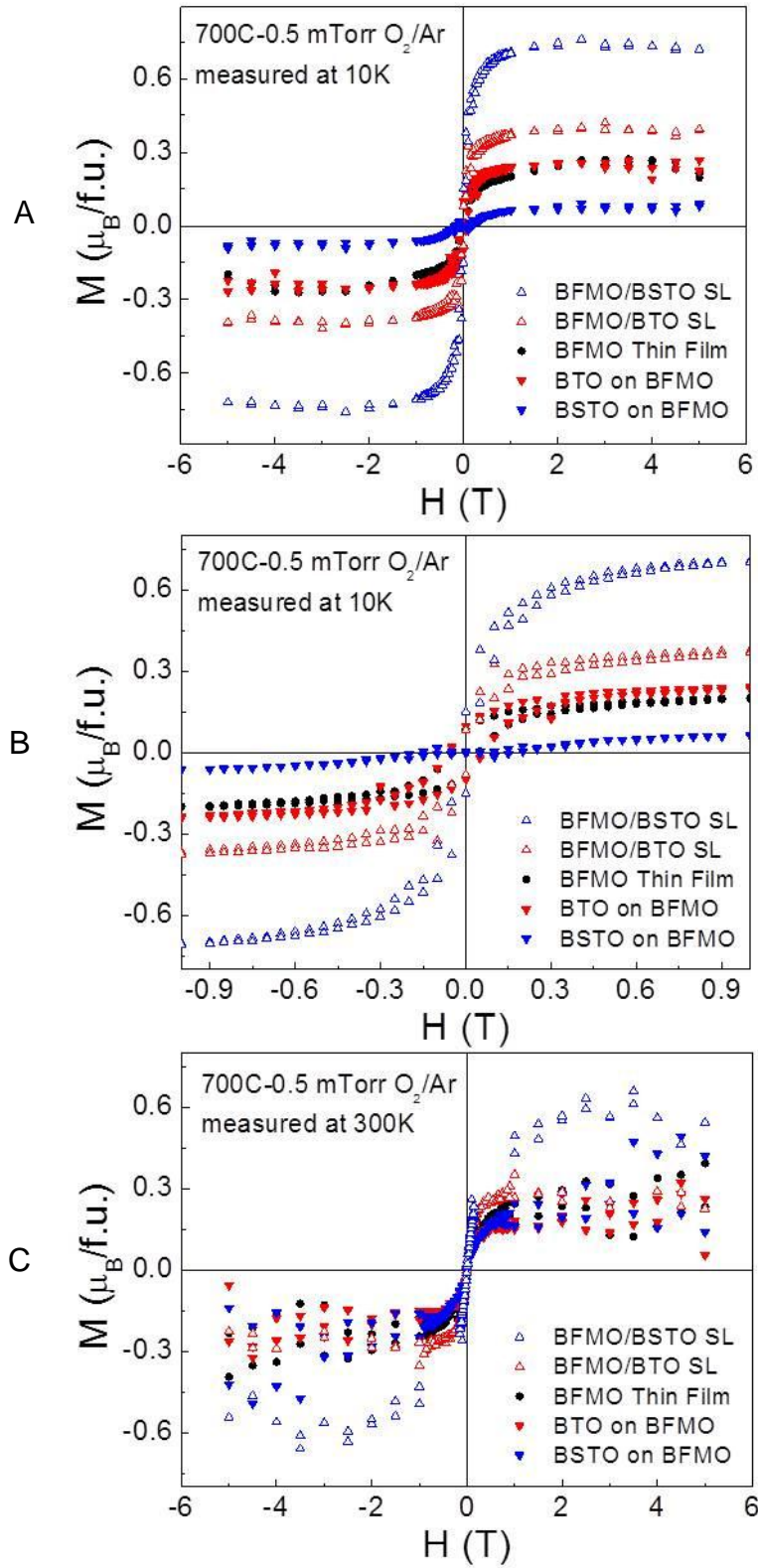


Figure 6-2. Magnetization curves of $\text{Ba}_2\text{FeMoO}_6$ thin films and hetero-structures measured at temperatures indicated

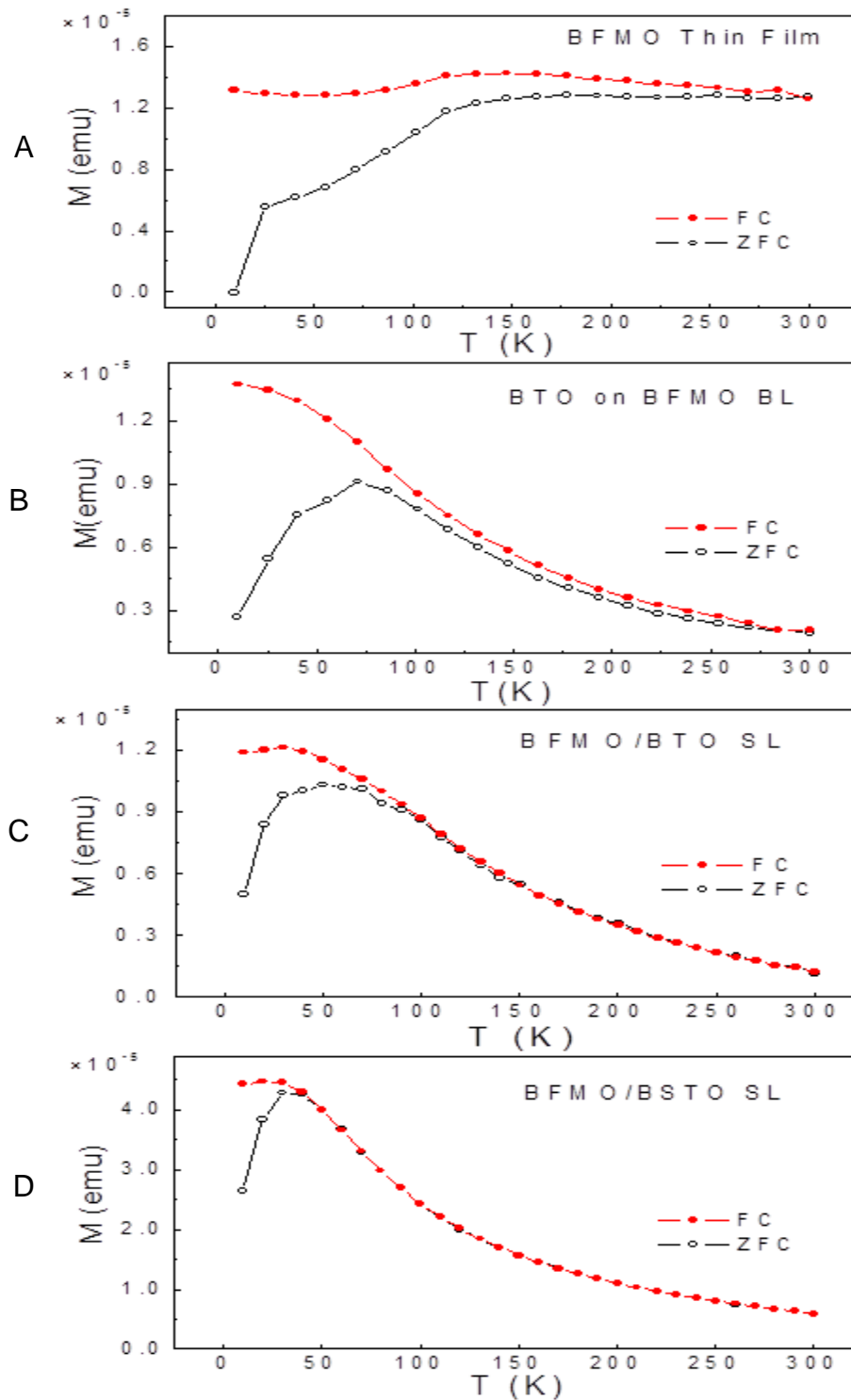


Figure 6-3. The temperature dependence of the magnetization $\text{Ba}_2\text{FeMoO}_6$ thin film and heterostructures. Images given for A) $\text{Ba}_2\text{FeMoO}_6$ thin film, B) BaTiO_3 on $\text{Ba}_2\text{FeMoO}_6$ BL, C) $\text{Ba}_2\text{FeMoO}_6/\text{BaTiO}_3$ SL, and D) $\text{Ba}_2\text{FeMoO}_6/\text{Ba}_{0.5}\text{Sr}_{0.5}\text{TiO}_3$ SL.

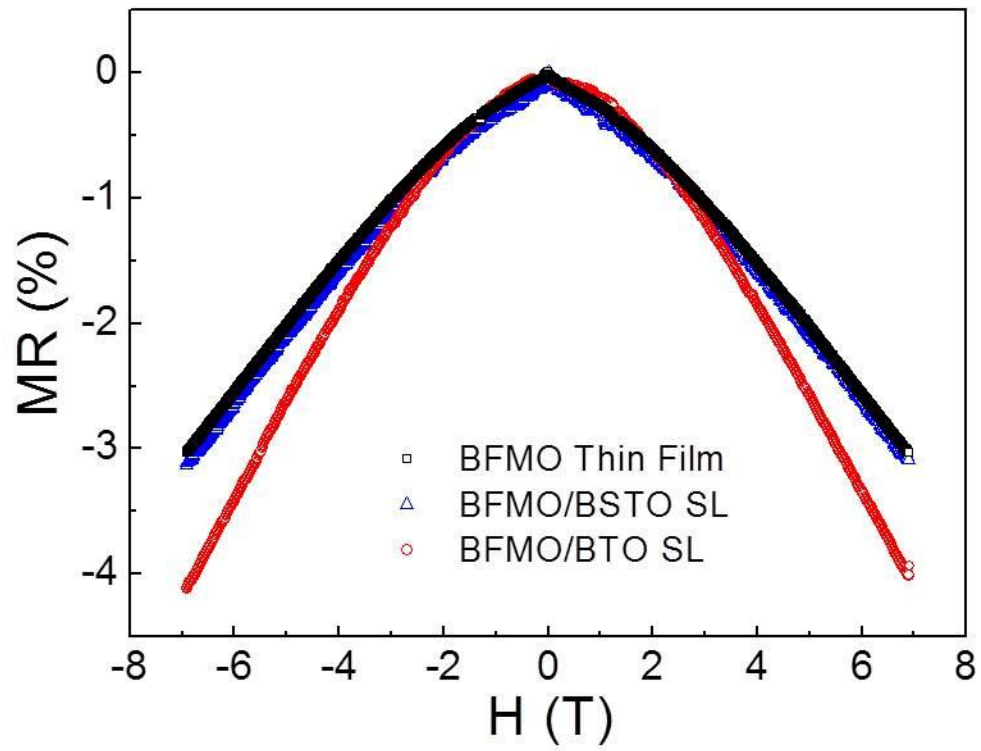


Figure 6-4. Magneto-resistance of $\text{Ba}_2\text{FeMoO}_6$ thin film and superlattices

CHAPTER 7
THE EFFECT OF STRUCTUE ON THE PROPERTIES OF $\text{Ba}_2\text{FeMoO}_6/\text{Ba}_{0.5}\text{Sr}_{0.5}\text{TiO}_3$
SUPERLATTICES

Introductory Remarks

A_2FeMoO_6 (A=Ca, Sr, Ba) is a double perovskite family which is a half metallic ferrimagnet with a high Curie temperature (T_C) over room temperature. $\text{Sr}_2\text{FeMoO}_6$ has been most studied due to a high T_C among them since Kobayashi *et al.* demonstrated the high saturation magnetization (M_S) close to the calculated value and a huge magneto-resistance in which the significant portion of it remained up to room temperature under a low magnetic field.¹² This gives substantial advantages in terms of device application over the manganite materials which also show a huge magneto-resistance called colossal magneto-resistance (CMR), but with a high magnetic field and relatively low temperature required. This makes $\text{Sr}_2\text{FeMoO}_6$ a prime candidate for spintronic related device applications.^{19,20,38,93,94} A simulation study showed that a long range antiferromagnetic ordering of Fe^{3+} ions and Mo^{5+} ions is a key aspect for achieving the high quality sample. Experimental works followed showing degradation of magnetic property by disordering, lowered M_S to less than $4\mu_B$ per formula unit and magneto-resistance.^{20,25,26,36}

$\text{Ba}_2\text{FeMoO}_6$ is a member of the A_2FeMoO_6 (A=Ba, Ca, Sr) family and is reported to have T_C as high as 367K.¹⁹ $\text{Ba}_2\text{FeMoO}_6$ has shown a huge magneto-resistance of over negative 30% for polycrystalline ceramic samples in multiple reports.^{22,44} With T_C well over room temperature, $\text{Ba}_2\text{FeMoO}_6$ can be one of the material selections for spintronic applications. However, this material has not been studied for a high quality film synthesis and its properties.

In previous chapters, $\text{Ba}_2\text{FeMoO}_6$ hetero-structures with $(\text{Ba,Sr})\text{TiO}_3$ were deposited and the properties of them were examined and compared with those of the thin films. In this chapter, we prepared hetero-epitaxial $\text{Ba}_2\text{FeMoO}_6/(\text{Ba,Sr})\text{TiO}_3$ superlattices on SrTiO_3 substrate by multiple target pulsed laser deposition and investigated their magnetic properties, specifically focusing on the dependence on the structure of the superlattice.

Experimental

The $\text{Ba}_2\text{FeMoO}_6/\text{Ba}_{0.5}\text{Sr}_{0.5}\text{TiO}_3$ superlattices were synthesized on SrTiO_3 substrates by multiple-target pulsed laser deposition. The targets were synthesized by a conventional solid state reaction with high purity (99.99% or higher) powders of BaCO_3 , Fe_2O_3 , MoO_3 , BaTiO_3 and SrTiO_3 . The detailed procedure for target fabrication is explained with diffraction studies of the target synthesized in the chapter 3.

$[\text{Ba}_2\text{FeMoO}_6]_5/[\text{Ba}_{0.5}\text{Sr}_{0.5}\text{TiO}_3]_N$ ($N=5, 10, 15, 20$) “ $5 \times N$ ” superlattices were deposited at $700\text{ }^\circ\text{C}$ under $0.5\text{ mTorr O}_2/\text{Ar}$ (0.2% oxygen) mixture gas. Five layers of double perovskite $\text{Ba}_2\text{FeMoO}_6$ were coupled with $\text{Ba}_{0.5}\text{Sr}_{0.5}\text{TiO}_3$ of N layers. The 248 nm wavelength KrF laser was utilized to ablate the ceramic targets. The laser energy and the repetition rate were 1.5 J/cm^2 and 2 Hz , respectively.

The structural properties of the superlattices were examined by X-ray diffraction (Phillips APD3720). Magnetization and magneto-transport were respectively measured using a Quantum Design Magnetic Properties Measurement System (MPMS) and Physics Properties Measurement System (PPMS).

Results and Discussion

Figure 7-1A shows the XRD pattern of $\text{Ba}_2\text{FeMoO}_6/ \text{Ba}_{0.5}\text{Sr}_{0.5}\text{TiO}_3$ 5×5 superlattice. Satellite peaks were observed along with $(00l)$ peaks of SrTiO_3 substrate.

A close look at the (002) peak area shown in Figure 7-1B clearly shows the decreased average lattice spacing of $[\text{Ba}_2\text{FeMoO}_6]_5/[\text{Ba}_{0.5}\text{Sr}_{0.5}\text{TiO}_3]_N$ superlattices with increasing layers of $\text{Ba}_{0.5}\text{Sr}_{0.5}\text{TiO}_3$ indicated by peaks shifting to a high angle. In Fig 7-2A, the average lattice spacing, d_{001} , of the superlattices were obtained using the zero-order superlattice peaks and plotted with the calculated ones using the half of the double perovskite $\text{Ba}_2\text{FeMoO}_6$ (4.03Å) and $\text{Ba}_{0.5}\text{Sr}_{0.5}\text{TiO}_3$ (3.954Å). The larger lattice spacing of superlattices than the calculated values suggests that the layers comprising the superlattices are elongated along the *c*-direction, which is partially attributed to in-plane compressive strain from the substrate SrTiO_3 (3.905 Å). It is known that the layers comprising superlattices suffer compressive or tensile strain depending on their relative lattice parameters of the parent materials and the strain affects the magnetic and ferroelectric properties.¹¹⁵⁻¹¹⁷ The difference between experimental and calculated values decreases with increasing layers of $\text{Ba}_{0.5}\text{Sr}_{0.5}\text{TiO}_3$, which suggests that the effect of strain decrease with *N*. $\text{Ba}_2\text{FeMoO}_6$ layer in a superlattice suffers more strain with the thicker $\text{Ba}_{0.5}\text{Sr}_{0.5}\text{TiO}_3$ layer. Thus the smaller difference indicates a relaxed $\text{Ba}_{0.5}\text{Sr}_{0.5}\text{TiO}_3$ layer in thicker superlattices.

In Figure 7-1B, the distances between adjacent satellite peaks decreased with increasing $\text{Ba}_{0.5}\text{Sr}_{0.5}\text{TiO}_3$ layer thicknesses. The periodicity, Λ , of a superlattice can be calculated using an equation

$$\Lambda = (L_i - L_j) \lambda / 2(\sin\theta_i - \sin\theta_j),$$

where, L_i and L_j are satellite peak indices, θ_i and θ_j are corresponding Bragg angles, and λ is the wavelength of X-ray.¹¹⁰ From obtained positions of satellite peaks around (001) of SrTiO_3 substrate, the periodicities of superlattices were calculated and

summarized in Table 7-1 and plotted with the $\text{Ba}_{0.5}\text{Sr}_{0.5}\text{TiO}_3$ layer thickness, N , in Figure 7-2B. The chemical modulation matched well with the designed structure for 5x5 and 5x10 superlattices and started to deviate from the SL 5x15. This discrepancy for thicker samples might be associated with the change of target surface state or fluctuation of laser energy difference in periodicity with the extended ablation.

Figure 7-3 shows the magnetization curves of the superlattices. In Figure 7-3A, at 10K, the superlattices showed the enhanced saturation magnetization (M_S) compared to thin films. The increased M_S are believed to be attributed to the strain in the superlattices. There have been reports on the strain induced enhancement of magnetization.¹¹¹⁻¹¹³ 5x15 and 5x20 superlattices in which $\text{Ba}_2\text{FeMoO}_6$ layers experience larger strain show the larger increase in M_S than 5x10 superlattice. However, the 5x5 superlattice didn't saturate in magnetization and showed paramagnetic behavior, which is not clearly understood. All superlattices showed a smaller coercive field than the thin film and the values are almost the same. In Figure 7-3C, at 300K, the superlattices except the 5x5 sample show the enhancement of M_S similar to the behavior at 10K, although the differences among samples are less clear due to the scattered data points around 0.3 T. It is interesting that the 5x5 superlattice showed the saturation in magnetization and the value is slightly lowered than the thin film. One possibility for this odd behavior of the sample is correlation between $\text{Ba}_2\text{FeMoO}_6$ and $\text{Ba}_{0.5}\text{Sr}_{0.5}\text{TiO}_3$ layers. The $\text{Ba}_{0.5}\text{Sr}_{0.5}\text{TiO}_3$ layers in the 5x5 superlattice experience the largest strain by the $\text{Ba}_2\text{FeMoO}_6$ layers, which might modify the property of $\text{Ba}_{0.5}\text{Sr}_{0.5}\text{TiO}_3$ layer. One would need to investigate the change with temperature in detail to understand the origin of paramagnetic to ferromagnetic transition.

In Figure 7-4, the temperature dependence of magnetization was shown in both field cooled (FC) and zero field cooled (ZFC) methods. In the zero field cooled method, a sample is cooled from room temperature without any applied magnetic field and then a small magnetic field is applied at 10K. The magnetization is measured as a function of temperature during warm up under a constant field. In the field cooled case, the sample is cooled from room temperature to 10K in an applied magnetic field and magnetization is measured during warm up. The thin film sample has a Curie temperature over 300K as shown in Figure 7-4A. In case of the 5x5 SL sample, during warm-up, the magnetization increased up to around 80 K and then decreased slowly in both modes but it didn't disappear up to a room temperature. As for the rest of superlattices, in contrast, the magnetization started to decrease from lower temperatures. And the temperatures at which the magnetization reached at maximum and started to drop in the ZFC mode decreased with increasing $\text{Ba}_{0.5}\text{Sr}_{0.5}\text{TiO}_3$ layer thickness. These results suggest that the lowered Curie temperature of the $\text{Ba}_2\text{FeMoO}_6$ layer in superlattices is attributed to the strain induced by the $\text{Ba}_{0.5}\text{Sr}_{0.5}\text{TiO}_3$ layer. It should be noted that even with the decreased magnetization at elevated temperatures, superlattices with thicker $\text{Ba}_{0.5}\text{Sr}_{0.5}\text{TiO}_3$ layers showed larger saturation magnetizations at 300K. A significant reduction in magnetization and T_C was reported in a manganite based superlattice, in which the charge transfer at interface was believed to induce the change.¹¹⁸

Magneto-resistances of the thin film and superlattices are shown in Figure 7-5. A large increase is observed in 5x5 and 5x10 superlattices. The enhancement diminish in 5x20 superlattices. The dependence on structure of magnetization and magneto-resistance was reported in $\text{La}_{0.7}\text{Ca}_{0.3}\text{MnO}_3/\text{BaTiO}_3$ superlattices, in which the strain

induced in the hetero-structures is maximized at a specific thickness of BaTiO_3 layer and the strains play a particular role in coupling of the two layers.¹¹⁶ It is interesting that the magnetization and magneto-resistance showed the same tendency with the thickness of coupled layers in that report, while magnetization and magneto-resistance does not show a clear correlation in this study.

Figure 7-6 shows the transport properties of the thin film and superlattices. In Figure 7-6A the resistivity decreases with increasing $\text{Ba}_{0.5}\text{Sr}_{0.5}\text{TiO}_3$ layer thickness, which suggests that $\text{Ba}_{0.5}\text{Sr}_{0.5}\text{TiO}_3$ layer is not insulating due to the low oxygen pressure during deposition. Also, the charge transfer at the interface might increase during an extended growth for thick $\text{Ba}_{0.5}\text{Sr}_{0.5}\text{TiO}_3$ layers. In figure 7-6B, all superlattices show anomalous Hall effect behaving hole-like indicated by the positive slope under a low magnetic field and show ordinary Hall effect behaving electron like under a large magnetic field. The anomalous portion increases with increasing thickness of $\text{Ba}_{0.5}\text{Sr}_{0.5}\text{TiO}_3$ layer that indicates the enhanced magnetization, although the difference is not clearly seen in the magnetization curves measured at 300K in Figure 7-3C.

Summary and Conclusions

In summary, the structural and magnetic properties were investigated in $\text{Ba}_2\text{FeMoO}_6$ thin film and $[\text{Ba}_2\text{FeMoO}_6]_5/[\text{Ba}_{0.5}\text{Sr}_{0.5}\text{TiO}_3]_N$ ($5 \times N$) superlattices prepared by pulsed laser deposition. The structural changes of superlattices were confirmed by XRD analysis with changes in the average lattice spacing. The magnetic properties of $\text{Ba}_2\text{FeMoO}_6$ layer significantly depend on the structure of the superlattices. At both 10K and 300K, superlattices with relatively thick $\text{Ba}_{0.5}\text{Sr}_{0.5}\text{TiO}_3$ showed strain induced enhancement of magnetization. A significant reduction in the Curie temperatures was observed and the magnitude of reduction increased with the strain. Interestingly,

magneto-resistance showed difference dependency on the structure from the magnetization, enhancement in superlattices with thin $\text{Ba}_{0.5}\text{Sr}_{0.5}\text{TiO}_3$ layers. The decreased resistivity of superlattices with thick $\text{Ba}_{0.5}\text{Sr}_{0.5}\text{TiO}_3$ layer suggests the leaky characteristic of the ferroelectric layer under the growth condition.

Table 7-1. Periodicities of the superlattices calculated from positions of the satellite peaks around (002) peak of Ba₂FeMoO₆ in Figure 7-1B

| Sample | BFMO/BSTO 5x5 | BFMO/BSTO 5x10 | BFMO/BSTO 5x15 | BFMO/BSTO 5x20 |
|-------------------------------------|------------------|-------------------|-------------------|-------------------|
| Superlattice peak index | Periodicity (Å) | Periodicity (Å) | Periodicity (Å) | Periodicity (Å) |
| SL ₋₂ - SL ₋₃ | | 79.9 | | 109.3 |
| SL ₋₁ - SL ₋₂ | 60.5 | 80.1 | 96.5 | 108.1 |
| SL ₀ - SL ₋₁ | 60.7 | 80.2 | 95.5 | 108.3 |
| SL ₊₁ - SL ₀ | 60 | 80.4 | 95.8 | 108.4 |
| SL ₊₂ - SL ₊₁ | 59.4 | 80.5 | 95.9 | 108.6 |
| SL ₊₃ - SL ₊₂ | | 80.7 | 96.1 | 107.5 |

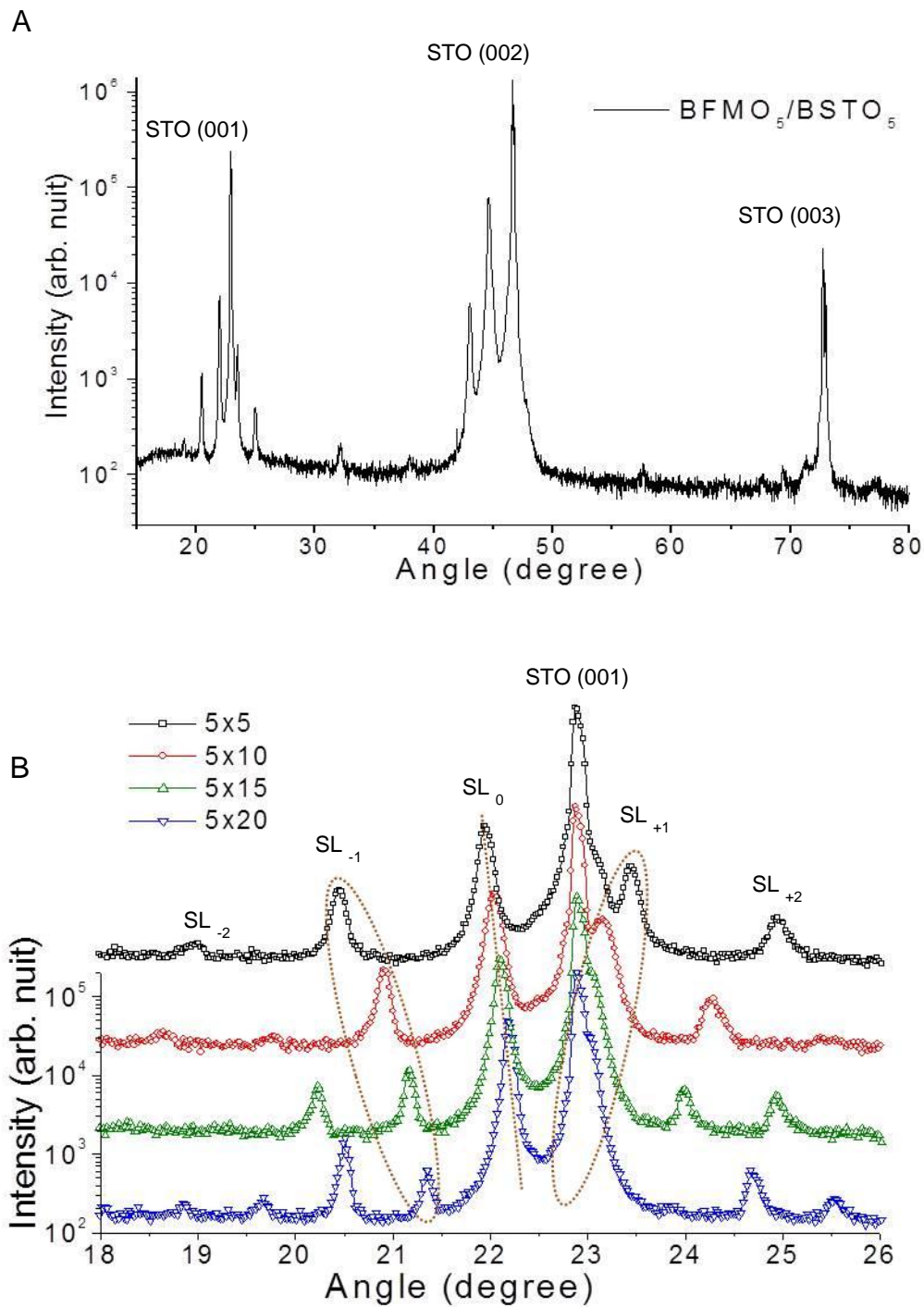


Figure 7-1. XRD pattern of Ba₂FeMoO₆/Ba_{0.5}Sr_{0.5}TiO₃ (5xN) superlattices. Images given for A) 5x5 superlattice and B) satellite peaks around (001) peak of substrate SrTiO₃.

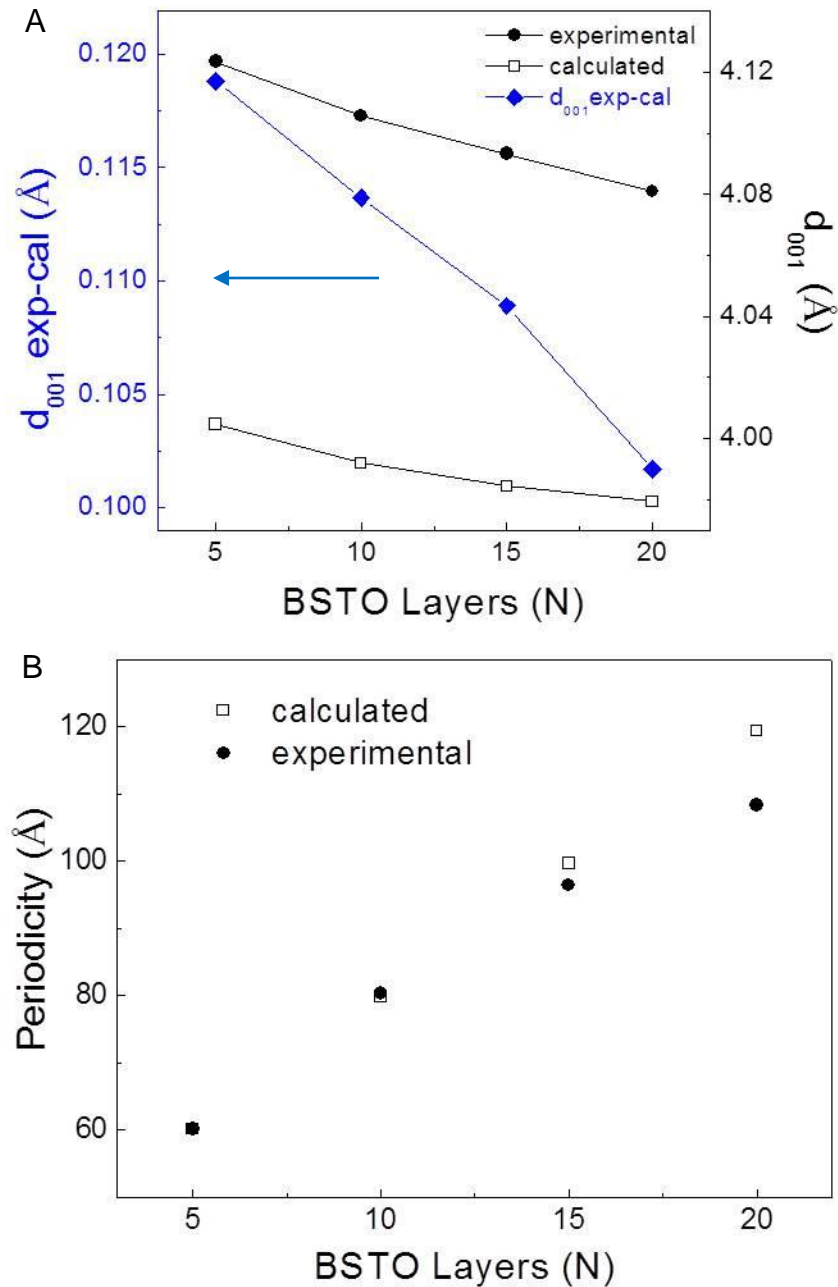


Figure 7-2. Lattice parameters and periodicities of $\text{Ba}_2\text{FeMoO}_6/\text{Ba}_{0.5}\text{Sr}_{0.5}\text{TiO}_3$ (5xN) superlattices. Images given for A) d_{001} , lattice spacing and difference between experimental and calculated ones. d_{cal} and d_{exp} are calculated value from references of bulk polycrystalline materials and experimental values from XRD measurement, respectively. B) Periodicities of superlattices.

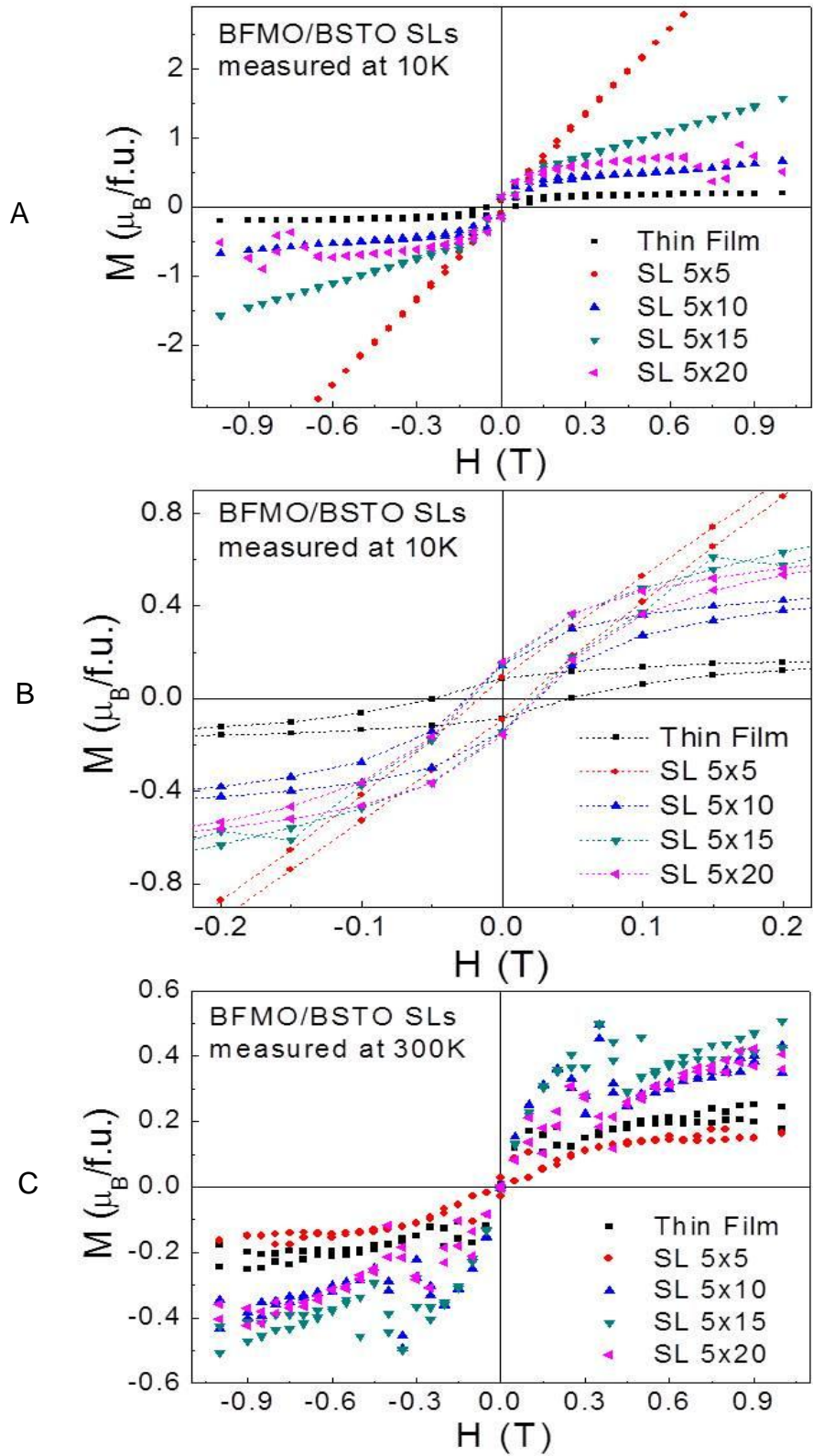


Figure 7-3. Magnetization curves of $\text{Ba}_2\text{FeMoO}_6$ thin film and superlattices measured at temperatures indicated

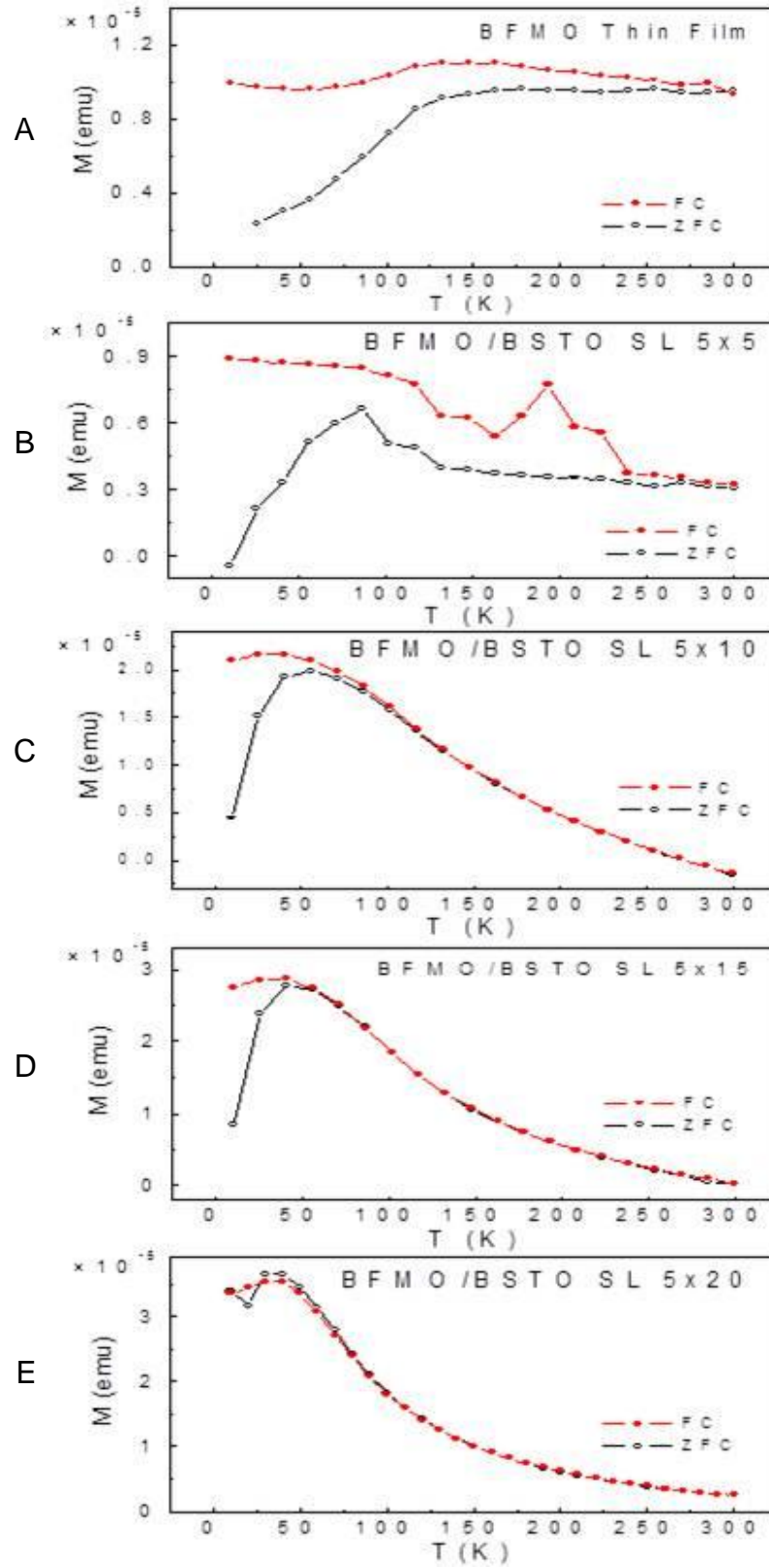


Figure 7-4. Temperature dependence of the magnetization of $\text{Ba}_2\text{FeMoO}_6$ thin film and superlattices

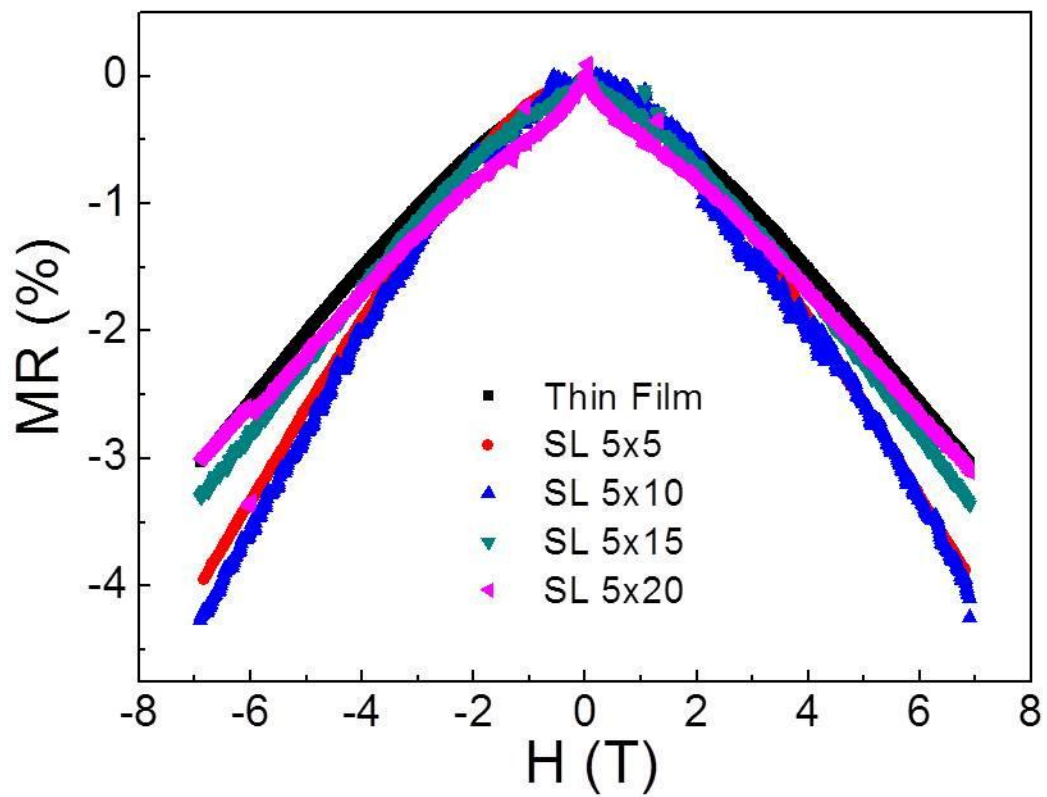


Figure 7-5. Magnetoresistance of $\text{Ba}_2\text{FeMoO}_6$ thin film and superlattices measured at 10K

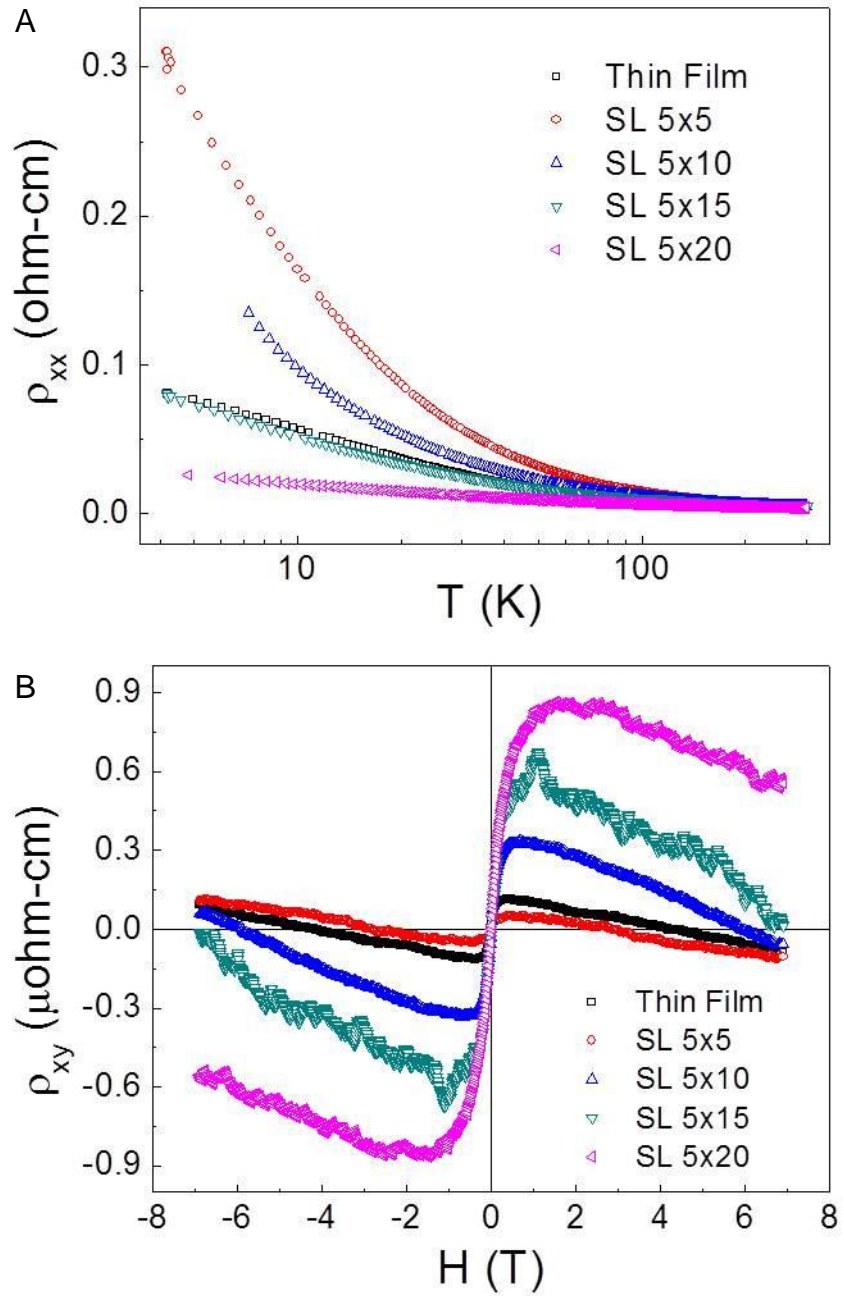


Figure 7-6. Transport properties of $\text{Ba}_2\text{FeMoO}_6/\text{Ba}_{0.5}\text{Sr}_{0.5}\text{TiO}_3$ (5xN) superlattices. Images given for A) temperature dependent resistivity and B) Hall resistivity of measured at 300K.

CHAPTER 8
THE EFFECTS OF ZnO BUFFER LAYERS ON THE PROPERTIES OF
PHOSPHORUS DOPED ZnO THIN FILMS GROWN ON SAPPHIRE BY PULSED
LASER DEPOSITION

Introductory Remarks

Zinc oxide has attracted significant interests largely due to its potential utility as a wide gap semiconductor for opto-electronics.^{71,119-121} Research on ZnO thin-film transistors and transparent conducting oxides have been driven by increasing demands for transparent electronics and photovoltaics with other competing semiconducting transparent oxide materials.¹²²⁻¹²⁵ Significant investment of effort has been made to realize highly reproducible high quality p-type ZnO thin film which is crucial to expanding the applications of ZnO based electronics.^{79,91,126-128} Also, there have been recent reports of p-type doping in nanowires and nanoparticles.¹²⁹⁻¹³³ In spite of some successful research related to p-type doping and light emitting devices,^{91,134,135} there remain significant challenges to understanding and controlling on the mechanisms for acceptor doping and the roles of related defects in ZnO.^{131,136}

The majority of studies investigating acceptor doping in ZnO have employed sapphire as the substrate. The large lattice mismatch between substrate and film induces formation of defects that degrade the crystalline quality may inhibit the realization of p-type doping. There is some debate on the roles of the different defects on doping.^{136,137} The native defects induced by the lattice mismatch during the deposition can compensate the acceptor dopants. There have been some studies on the use of undoped ZnO buffer layers in the growth of for p-type ZnO thin films.⁹¹ Previous studies suggest that the buffer layer has significant effects on the properties of doped layer subsequent. In this study, phosphorus doped ZnO thin films were deposited

on ZnO buffer layers that were grown under different conditions. Their structure and transport properties were analyzed in order to elucidate the role of the buffer layers.

Experimental

Undoped and phosphorus doped ZnO thin films were synthesized using pulsed laser deposition with ceramic targets synthesized with high purity powders. Phosphorus was chosen as a dopant for p-type doping. The targets were made by the conventional solid state reaction and the starting materials were ZnO and P₂O₅. The powders were mixed with stoichiometric compositions of 0.1 and 0.5 mole percent of phosphorus and were pressed into one-inch diameter pellets. The pellets were sintered for four hours at 1200°C in air. C-plane sapphire was used as the substrate. A 248 nm KrF laser was utilized. The laser energy density and the repetition rate are about 1.5 J/cm² and 1 Hz, respectively. The chamber was pumped down to the base pressure of low 10⁻⁷ Torr. Two types of buffer layers were considered. For one set, a low temperature buffer layer was deposited. In particular, the growth conditions for this undoped ZnO buffer layer were 400°C under 20 mTorr O₂. For a second set, a high temperature buffer layer was selected. In this case, the undoped ZnO buffer layer was deposited at 700°C under 1 mTorr O₂. The thickness of buffer layer was 50 nm for both temperatures. And the thick buffer layers were additionally grown to observe the vertical microstructures. Phosphorus doped ZnO thin films were then deposited on the buffer layers at 700°C under oxygen atmosphere with the pressure range between 10-150 mTorr. The thicknesses of phosphorus doped ZnO layers were at least 600 nm to minimize the contribution of buffer layers. After growth, samples were cooled down under the same oxygen atmosphere to room temperature. After the deposition, the films were rapid thermally annealed at 900°C for three minutes under oxygen atmosphere.

Field emission scanning electron microscopy (JEOL JSM-6335F) and atomic force microscopy (Veeco Dimension 3100) were utilized to observe the microstructure and surface of the samples. X-ray diffraction (Phillips APD 3720, Phillips X'pert MRD) was utilized to analyze the crystalline qualities of thin films. Hall effect measurement (Lakeshore 7507 Hall Effect) was carried out to investigate the transport properties of phosphorus doped ZnO thin films including carrier type, resistivity, carrier concentration, and mobility.

Results and Discussion

Table 8-1 shows the Hall transport properties of ZnO:P_{0.001} thin films. As for the films grown on high temperature buffer layer, as deposited ZnO:P_{0.001} thin films showed n-type conductivity which is consistent with previous efforts on ZnO:P_{0.005} thin films showing that phosphorus can induce either donor or acceptor states in ZnO.^{81,126} After the rapid thermal annealing, the films grown on the high temperature buffer layer showed reduced electron carrier concentrations and increased resistivity but remained n-type. The relatively small change of mobility compared to resistivity and carrier concentration suggests that the rapid thermal anneal affected the defect structure associated with phosphorus rather than the overall crystallinity of the film. Note that this change by annealing does not appear to be associated with defects solely related to Zn and O. Previous reports showed that the transport properties of undoped ZnO thin films change little with this type of rapid thermal annealing treatment.⁸¹

In contrast, the as-grown phosphorus doped ZnO films deposited on low temperature buffer layers show n-type conductivity but have much larger resistivity than films on high temperature buffer layer. After annealing, the film grown under high oxygen pressure of 150 mTorr showed p-type conduction while the sample grown under

10 mTorr remained n-type. It should be noted that the transport properties of annealed samples are difficult to quantify with Hall effect measurements due to contributions from the semi-insulating phosphorus doped ZnO and the low temperature undoped ZnO buffer layer. Despite the difficulty in quantifying carrier concentration, it is noted that the increases of resistivity are much larger in the films on the low temperature buffer layer than for films on high temperature buffer layers. Considering that the rapid thermal annealing primarily affects defects associated with phosphorus, the larger change in resistivity suggests that more dopants are incorporated during deposition and converted by the rapid thermal annealing in the films on low temperature buffer layer. It suggests that the poorer crystalline quality of the low temperature buffer layer induces a higher defect density in the subsequent phosphorus doped film, acting as favorable sites for defect incorporation related to the phosphorus dopants. Also, it is clear that a low electron carrier concentration of as grown state is important in converting the carrier type by the rapid thermal annealing. Note that after annealing, the mobility slightly increased in the films grown on high temperature buffer layers in contrast to the decreased mobility in the films on low temperature buffer layer. It is not entirely clear what yields the different tendencies.

Figure 8-1 shows the omega rocking curves of ZnO (002) peaks for ZnO:P_{0.005} thin films grown on different types of buffer layers. The diffraction results clearly show broader peaks rocking curves, and hence higher defect density, for phosphorus doped ZnO thin films grown on the low temperature buffer layer as compared to the high temperature buffer layer. It is assumed that this reflects a higher concentration of phosphorus incorporation in the poorer crystalline quality films. Also, the oxygen

pressure during deposition has a significant effect on the crystalline quality of the films for those grown on the low temperature buffer layer. Films deposited on the high temperature buffer layer don't exhibit this degree of sensitivity to oxygen pressure.

The surface microstructure was also examined using atomic force microscopy and scanning electron microscopy. Again, the use of a high temperature appears to induce a lower density of defects. From Figure 8-2 and 8-3, it is shown that the films grown on high temperature buffer layer have smoother film surfaces and less particulates. In addition, the low oxygen pressure during film deposition leads to the smooth surface. It is noted that oxygen deficient growth condition may lead to more donor defects including oxygen vacancies that can act a donor defect in ZnO thin films. This can be seen from the table which shows that phosphorus doped ZnO thin films grown under low oxygen pressure are more conductive when grown on the same buffer layer.

Another interesting feature is the microstructure of the ZnO:P_{0.001} thin films. Figure 8-4 shows the cross-section images of ZnO:P_{0.001} thin films. The structures of the films are very different on each buffer layer. After comparing with the microstructures of the buffer layers, it is found that the microstructures of ZnO:P_{0.001} thin films are mainly determined by the structures of buffer layers.

Summary and Conclusions

In conclusion, we have investigated the structure and transport property of phosphorus doped ZnO thin films by PLD grown on different buffer layers. The films grown on low temperature buffer layer are more resistive with a low carrier concentration and show significant changes in electronic properties by the rapid thermal annealing. It suggests that more dopants are incorporated in the films on low crystalline quality buffer layer grown at low temperature during deposition. In spite that a high

temperature buffer is not appropriate for p-type doping, it can be used to improve the crystalline quality and surface morphology of doped ZnO layer.

Table 8-1. Hall transport properties of as-grown and rapid thermal annealed ZnO:P_{0.001} thin films

| | As grown | Annealed | As grown | Annealed |
|---|----------|----------|----------|----------|
| A) 700°C-150 mTorr O ₂ | | | | |
| Carrier Concentration (cm ⁻³) | 1.29E+19 | 3.04E+17 | 1.83E+18 | 3.31E+15 |
| Mobility (cm ² /V·s) | 3.24E+01 | 3.87E+01 | 1.07E+00 | 5.31E-01 |
| Resistivity (Ω·cm) | 1.50E-02 | 5.30E-01 | 3.19E+00 | 3.56E+03 |
| Carrier Type | n | n | n | p |
| Buffer layer | on HTB | | on LTB | |
| B) 700°C-10 mTorr O ₂ | | | | |
| Carrier Concentration (cm ⁻³) | 3.51E+19 | 6.11E+17 | 5.18E+18 | 3.44E+14 |
| Mobility (cm ² /V·s) | 4.54E+01 | 5.61E+01 | 7.67E+00 | 1.76E+00 |
| Resistivity (Ω·cm) | 3.91E-03 | 1.82E-01 | 1.57E-01 | 1.03E+04 |
| Carrier Type | n | n | n | n |
| Buffer layer | on HTB | | on LTB | |

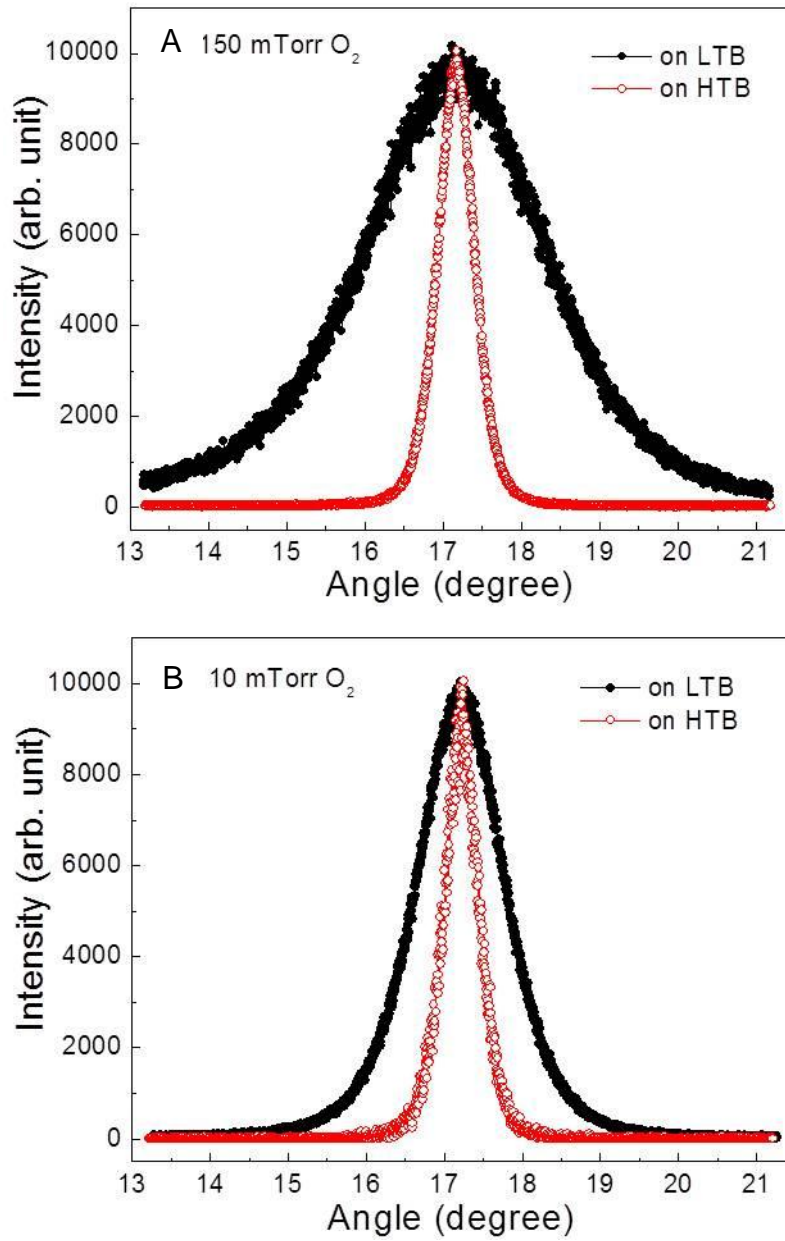


Figure 8-1. Rocking curves of (002) peaks of ZnO:P_{0.005} thin films grown on the buffer layers under oxygen pressures indicated

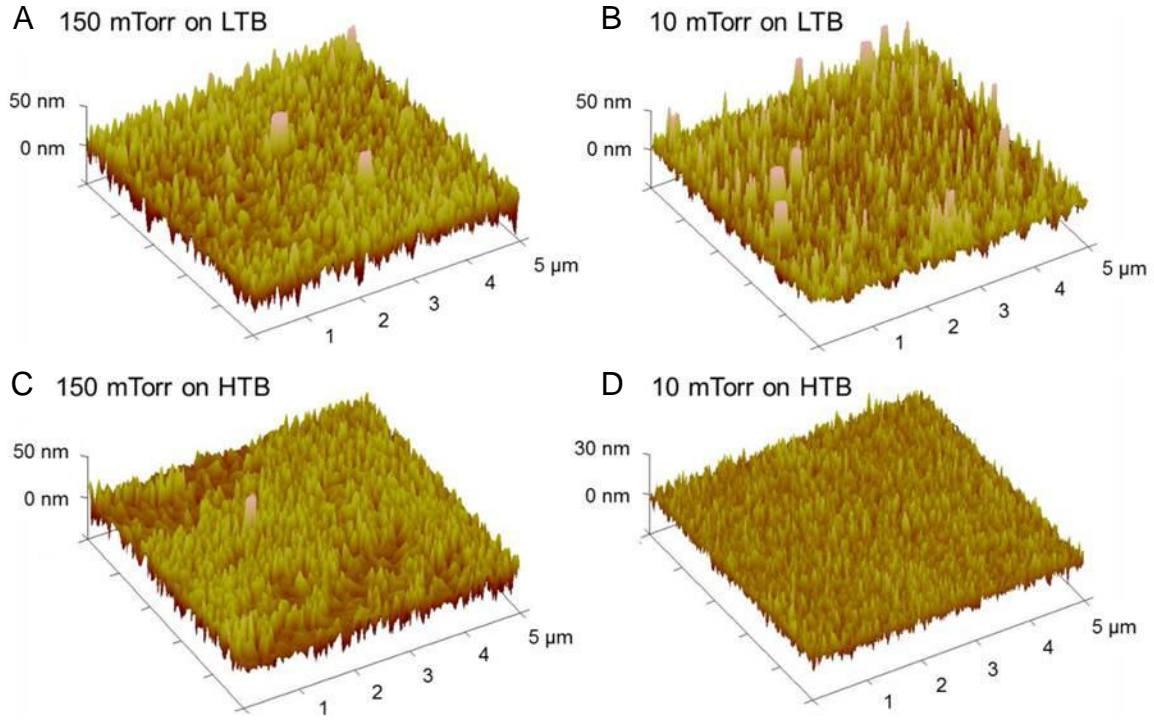


Figure 8-2. AFM images of ZnO:P_{0.005} thin films grown on the buffer layers under oxygen pressures indicated. RMS roughness values are 13.3, 11.4, 10.2, and 4.84 nm from A) to D).

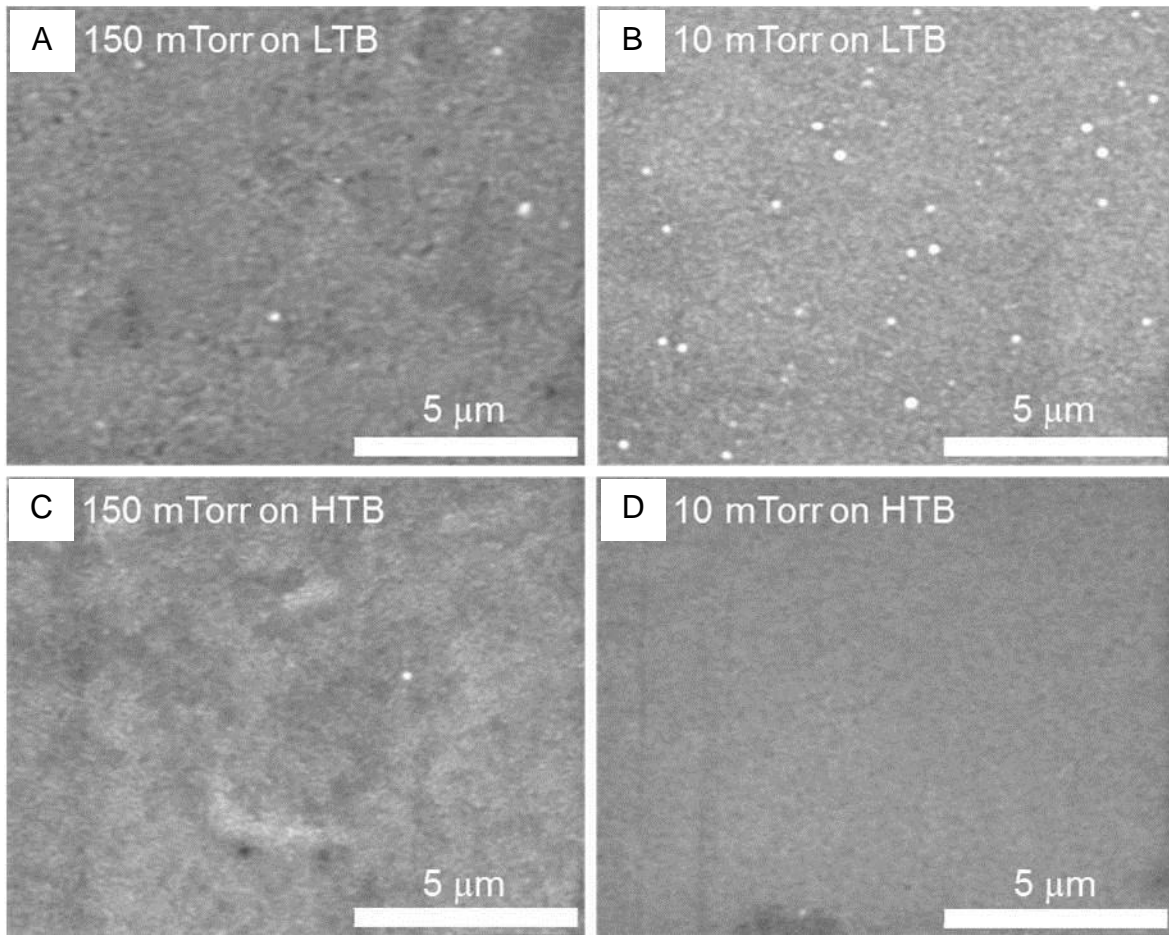


Figure 8-3. SEM images of ZnO:P_{0.005} films grown on the buffer layers under oxygen pressures indicated

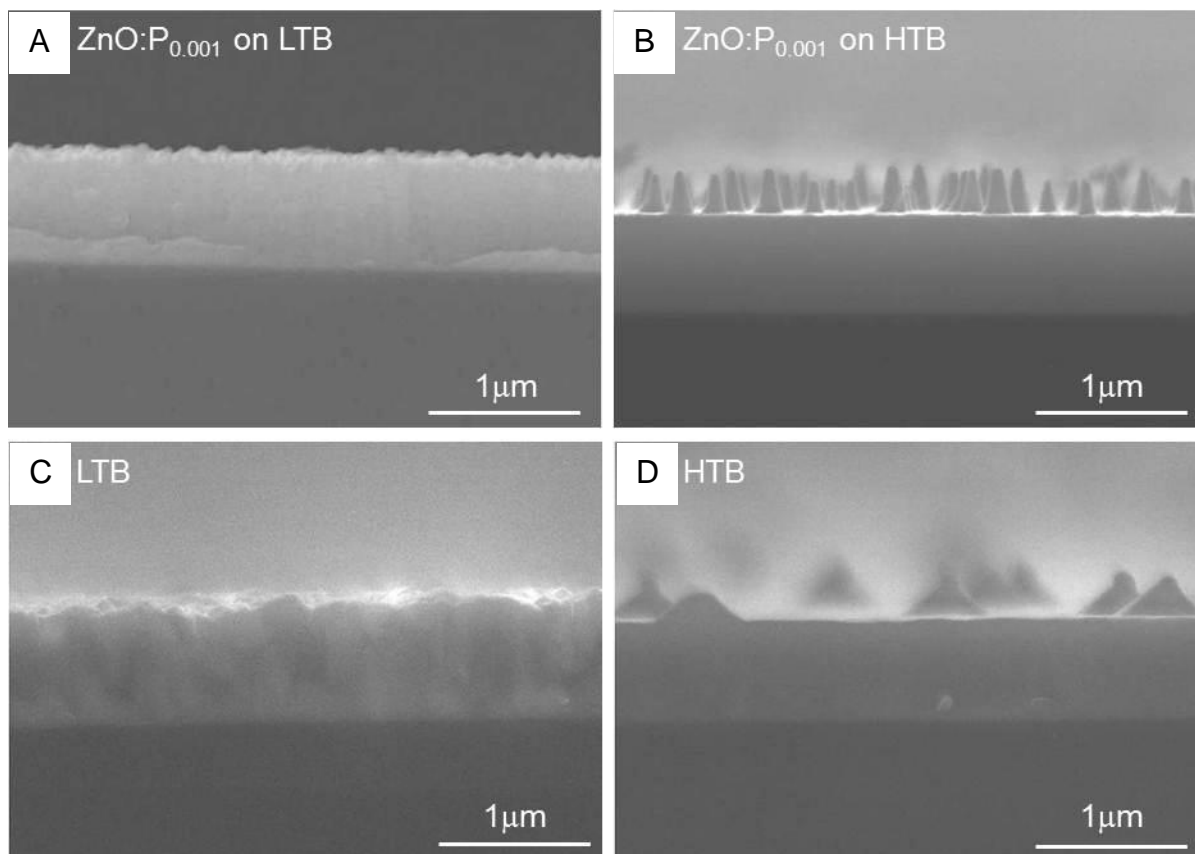


Figure 8-4. Cross section images of ZnO:P_{0.001} thin films and buffer layers grown at 700°C under 10 mTorr O₂. Images given for A) ZnO:P_{0.001} thin films grown on low temperature buffer layer, B) ZnO:P_{0.001} thin films grown on high temperature buffer layer, C) low temperature buffer, and D) high temperature buffer

CHAPTER 9 CONCLUSIONS

Ba₂FeMoO₆ Thin Film and Hetero-structures

Double perovskite Ba₂FeMoO₆ thin films were grown under various growth conditions by pulsed laser deposition and the structural, magnetic and magneto-transport properties were investigated, focusing on the effects of growth temperature and oxygen partial pressure. Phase pure Ba₂FeMoO₆ thin films were epitaxially grown on SrTiO₃ substrates at temperatures ranging from 700-900°C under high vacuum while an impurity BaMoO₄ phase coexisted when the films were deposited with pure oxygen gas. The thin films grown at high temperature showed a better saturation magnetization (M_S) and magneto-resistance but its Curie temperature (T_C) is low, around 250K compared to the previous bulk studies. The low M_S (1.1 μ_B /f.u. for 900°C sample) and T_C (around 250K) of thin films were believed to due to the antisite defects, i.e., disordering of Fe and Mo atoms in B-sites. Also Ba₂FeMoO₆ thin films showed interesting transport properties; a change in conduction mechanisms with temperature and anomalous Hall effect. The samples showed an anomalous Hall effect with hole-like behavior under low magnetic field and showed an ordinary electron-like transport property under high magnetic field. The portion of anomalous Hall effect decreased due to increasing electron carriers at elevated temperatures.

When thin films were grown under low oxygen partial pressure with O₂/Ar mixture gas, the magnetic properties were degraded but the Curie temperature increased. Auger electron spectroscopy (AES) study revealed that the ratio of Fe:Mo got further from one, the ideal stoichiometry, with increasing oxygen pressure during deposition, which is consistent with XRD results that showed the smaller lattice spacing of the thin

films grown under higher oxygen pressure. This increased off-stoichiometry was responsible for the degradation of magnetization of the films grown under high oxygen partial pressure. Also unusual positive magneto-resistance observed in films grown under high vacuum disappeared, which suggests that it is associated with the oxygen related defects.

The $\text{Ba}_2\text{FeMoO}_6$ based hetero-structures with $\text{Ba}_{1-x}\text{Sr}_x\text{TiO}_3$ were synthesized and their structures and magnetic properties were examined. The superlattice structures were confirmed by satellite peaks and the periodicities were calculated. The $\text{Ba}_2\text{FeMoO}_6/\text{Ba}_{1-x}\text{Sr}_x\text{TiO}_3$ superlattices showed the strain induced enhancement of magnetization compared to the thin film and the enhancement was dependent on the strain induced by coupled layer. The Curie temperatures of superlattices were lowered substantially. The effects of superlattice structure were investigated with the samples having varying $\text{Ba}_{1-x}\text{Sr}_x\text{TiO}_3$ layer thicknesses. The saturation magnetization was enhanced in superlattices with thick $\text{Ba}_{1-x}\text{Sr}_x\text{TiO}_3$ layers at 10K and 300K. The Curie temperatures of superlattices were suppressed significantly by strain induced in the superlattice structures. Interestingly, the enhancement of magneto-resistance was observed in the superlattices with the thin $\text{Ba}_{0.5}\text{Sr}_{0.5}\text{TiO}_3$ layer unlike the magnetization. The decreased resistivity of superlattices with thick $\text{Ba}_{0.5}\text{Sr}_{0.5}\text{TiO}_3$ layer indicates the ferroelectric layer is undesirably leaky under the growth condition. The change in the portion of anomalous Hall effect is consistent with the change in magnetization induced by the strains in superlattices.

p-type Doping in ZnO Thin Films

Phosphorus doped ZnO thin films were deposited on two different types of ZnO buffer layers; high temperature buffer layer (HTB) and low temperature buffer layer

(LTB) were deposited at 700°C under 1mTorr O₂ and 400°C under 20 mTorr O₂, respectively. The properties of phosphorus doped ZnO thin films were investigated focusing on the the effects of f buffer layers. Phosphorus doped ZnO thin films on LTB were less conductive as grown state and showed a drastic change in the transport properties upon the rapid thermal annealing. This suggests that poor crystalline quality of the LTB lead to the more incorporation of phosphorus dopants in following films. The p-type conduction was observed only in the phosphorus doped thin films grown on LTB. All the phosphorus doped ZnO thin films grown on HTB showed n-type conduction regardless of the growth condition. A high resolution X-ray diffraction study revealed that phosphorus doped ZnO thin films grown on LTB had the poor crystalline quality indicated by much broader peaks of omega rocking curves. Also it was observed that the microstructures of the phosphorus doped ZnO thin film significantly depended on the buffer layer. HTB might be useful to improve the surface morphology and crystalline quality, although it is not proper for the incorporation of dopants.

LIST OF REFERENCES

- 1 D. Dijkkamp, T. Venkatesan, X. D. Wu, S. A. Shaheen, N. Jisrawi, Y. H. Min-Lee, W. L. McLean, and M. Croft, *Appl. Phys. Lett.* 51, 619 (1987).
- 2 D. G. Schlom, J. N. Eckstein, E. S. Hellman, S. K. Streiffer, J. J. S. Harris, M. R. Beasley, J. C. Bravman, T. H. Geballe, C. Webb, K. E. von Dessionneck, and F. Turner, *Appl. Phys. Lett.* 53, 1660 (1988).
- 3 A. Ohtomo, D. A. Muller, J. L. Grazul, and H. Y. Hwang, *Nature* 419, 378 (2002).
- 4 G. Logvenov, A. Gozar, and I. Bozovic, *Science* 326, 699 (2009).
- 5 A. Tsukazaki, A. Ohtomo, T. Kita, Y. Ohno, H. Ohno, and M. Kawasaki, *Science* 315, 1388 (2007).
- 6 A. Ohtomo and H. Y. Hwang, *Nature* 427, 423 (2004).
- 7 S. Okamoto and A. J. Millis, *Nature* 428, 630 (2004).
- 8 S. Thiel, G. Hammerl, A. Schmehl, C. W. Schneider, and J. Mannhart, *Science* 313, 1942 (2006).
- 9 J. Chakhalian, J. W. Freeland, G. Srajer, J. Stremper, G. Khaliullin, J. C. Cezar, T. Charlton, R. Dalgliesh, C. Bernhard, G. Cristiani, H. U. Habermeier, and B. Keimer, *Nat. Phys.* 2, 244 (2006).
- 10 J. H. Haeni, P. Irvin, W. Chang, R. Uecker, P. Reiche, Y. L. Li, S. Choudhury, W. Tian, M. E. Hawley, B. Craigo, A. K. Tagantsev, X. Q. Pan, S. K. Streiffer, L. Q. Chen, S. W. Kirchoefer, J. Levy, and D. G. Schlom, *Nature* 430, 758 (2004).
- 11 J. H. Lee, L. Fang, E. Vlahos, X. Ke, Y. W. Jung, L. F. Kourkoutis, J.-W. Kim, P. J. Ryan, T. Heeg, M. Roeckerath, V. Goian, M. Bernhagen, R. Uecker, P. C. Hammel, K. M. Rabe, S. Kamba, J. Schubert, J. W. Freeland, D. A. Muller, C. J. Fennie, P. Schiffer, V. Gopalan, E. Johnston-Halperin, and D. G. Schlom, *Nature* 466, 954 (2010).
- 12 K. I. Kobayashi, T. Kimura, H. Sawada, K. Terakura, and Y. Tokura, *Nature* 395, 677 (1998).
- 13 D. Serrate, J. M. D. Teresa, and M. R. Ibarra, *J. Phys.: Condens. Matter* 19, 023201 (2007).
- 14 O. Erten, O. N. Meetei, A. Mukherjee, M. Randeria, N. Trivedi, and P. Woodward, *Phys. Rev. Lett.* 107, 257201 (2011).
- 15 A. P. Ramirez, *J. Phys.: Condens. Matter* 9, 8171 (1997).

- 16 N. D. Mathur, G. Burnell, S. P. Isaac, T. J. Jackson, B. S. Teo, J. L. MacManus-Driscoll, L. F. Cohen, J. E. Evetts, and M. G. Blamire, *Nature* 387, 266 (1997).
- 17 R. von Helmolt, J. Wecker, B. Holzapfel, L. Schultz, and K. Samwer, *Phys. Rev. Lett.* 71, 2331 (1993).
- 18 H. Y. Hwang, S. W. Cheong, N. P. Ong, and B. Batlogg, *Phys. Rev. Lett.* 77, 2041 (1996).
- 19 R. P. Borges, R. M. Thomas, C. Cullinan, J. M. D. Coey, R. Suryanarayanan, L. Ben-Dor, L. Pinsard-Gaudart, and A. Revcolevschi, *J. Phys.: Condens. Matter* 11, L445 (1999).
- 20 A. S. Ogale, S. B. Ogale, R. Ramesh, and T. Venkatesan, *Appl. Phys. Lett.* 75, 537 (1999).
- 21 C. Ritter, M. R. Ibarra, L. Morellon, J. Blasco, J. García, and J. M. D. Teresa, *J. Phys.: Condens. Matter* 12, 8295 (2000).
- 22 H. Han, B. J. Han, J. S. Park, B. W. Lee, S. J. Kim, and C. S. Kim, *J. Appl. Phys.* 89, 7687 (2001).
- 23 N. Nguyen, F. Sriti, C. Martin, F. Bourée, J. M. Grenèche, A. Ducouret, F. Studer, and B. Raveau, *J. Phys.: Condens. Matter* 14, 12629 (2002).
- 24 J. H. Song, J. H. Park, and Y. H. Jeong, *J. Appl. Phys.* 97, 046105 (2005).
- 25 D. D. Sarma, E. V. Sampathkumaran, S. Ray, R. Nagarajan, S. Majumdar, A. Kumar, G. Nalini, and T. N. Guru Row, *Sol. Stat. Comm.* 114, 465 (2000).
- 26 C. Meneghini, S. Ray, F. Liscio, F. Bardelli, S. Mobilio, and D. D. Sarma, *Phys. Rev. Lett.* 103, 046403 (2009).
- 27 J. Linden, T. Yamamoto, M. Karppinen, H. Yamauchi, and T. Pietari, *Appl. Phys. Lett.* 76, 2925 (2000).
- 28 D. Kumar and D. Kaur, *Phys. B: Condens. Matter* 405, 3259 (2010).
- 29 R. P. Borges, S. Lhostis, M. A. Bari, J. J. Versluijs, J. G. Lunney, J. M. D. Coey, M. Besse, and J. P. Contour, *Thin Solid Films* 429, 5 (2003).
- 30 W. Westerburg, D. Reisinger, and G. Jakob, *Phys. Rev. B* 62, R767 (2000).
- 31 M. S. Moreno, J. E. Gayone, M. Abbate, A. Caneiro, D. Niebieskikwiat, R. D. Sánchez, A. de Siervo, R. Landers, and G. Zampieri, *Sol. Stat. Comm.* 120, 161 (2001).
- 32 J. Navarro, B. Li, F. Sandiumenge, M. Bibes, A. Roig, B. Martínez, and J. Fontcuberta, *J. Phys.: Condens. Matter* 13, 8481 (2001).

- 33 K. Kuepper, M. Kadiroglu, A. V. Postnikov, K. C. Prince, M. Matteucci, V. R. Galakhov, H. Hesse, G. Borstel, and M. Neumann, *J. Phys.: Condens. Matter* 17, 4309 (2005).
- 34 H. Jalili, N. F. Heinig, and K. T. Leung, *Phys. Rev. B* 79, 174427 (2009).
- 35 M. Rutkowski, *J. Vac. Sci. Technol., A* 28, 1240 (2010).
- 36 D. Topwal, D. D. Sarma, H. Kato, Y. Tokura, and M. Avignon, *Phys. Rev. B* 73, 094419 (2006).
- 37 A. Poddar, R. N. Bhowmik, I. P. Muthuselvam, and N. Das, *J. Appl. Phys.* 106, 073908 (2009).
- 38 H. Asano, S. B. Ogale, J. Garrison, A. Orozco, Y. H. Li, E. Li, V. Smolyaninova, C. Galley, M. Downes, M. Rajeswari, R. Ramesh, and T. Venkatesan, *Appl. Phys. Lett.* 74, 3696 (1999).
- 39 W. Westerburg, F. Martin, and G. Jakob, *J. Appl. Phys.* 87, 5040 (2000).
- 40 J. E. Evetts, M. G. Blamire, N. D. Mathur, S. P. Isaac, B. S. Teo, L. F. Cohen, J. L. Macmanus-Driscoll, P. B. Littlewood, G. A. Gehring, T. Venkatesan, M. Rzchoswki, R. Stroud, and A. J. Millis, *Phil. Trans.: Math. Phys. Eng. Sci.* 356, 1593 (1998).
- 41 T. Asaka, X. Z. Yu, Y. Tomioka, Y. Kaneko, T. Nagai, K. Kimoto, K. Ishizuka, Y. Tokura, and Y. Matsui, *Phys. Rev. B* 75 (2007).
- 42 A. Maignan, B. Raveau, C. Martin, and M. Hervieu, *Journal of Solid State Chemistry* 144, 224 (1999).
- 43 W. Y. Lee, H. Han, S. B. Kim, C. S. Kim, and B. W. Lee, *J. Magn. Magn. Mater.* 254, 577 (2003).
- 44 W. Zhong, N. J. Tang, C. T. Au, and Y. W. Du, *IEEE Trans. Mag.* 43, 3079 (2007).
- 45 H. V. Alexandru, C. Berbecaru, A. Ioachim, L. Nedelcu, and A. Dutu, *Appl. Surf. Sci.* 253, 354 (2006).
- 46 S. F. Karmanenko, A. I. Dedyk, A. A. Melkov, R. N. Il'in, V. I. Sakharov, I. T. Serenkov, and H. Jowoong, *J. Phys.: Condens. Matter* 14, 6823 (2002).
- 47 L. M. B. Alldredge, J. C. Woicik, W. Chang, S. W. Kirchoefer, and J. M. Pond, *Appl. Phys. Lett.* 91, 052909 (2007).
- 48 T. M. Shaw, Z. Suo, M. Huang, E. Liniger, R. B. Laibowitz, and J. D. Baniecki, *Appl. Phys. Lett.* 75, 2129 (1999).

- 49 H. Schmid, *Ferroelectrics* 162, 317 (1994).
- 50 J. Wang, J. B. Neaton, H. Zheng, V. Nagarajan, S. B. Ogale, B. Liu, D. Viehland, V. Vaithyanathan, D. G. Schlom, U. V. Waghmare, N. A. Spaldin, K. M. Rabe, M. Wuttig, and R. Ramesh, *Science* 299, 1719 (2003).
- 51 T. Zhao, A. Scholl, F. Zavaliche, K. Lee, M. Barry, A. Doran, M. P. Cruz, Y. H. Chu, C. Ederer, N. A. Spaldin, R. R. Das, D. M. Kim, S. H. Baek, C. B. Eom, and R. Ramesh, *Nat. Mater.* 5, 823 (2006).
- 52 T. Choi, S. Lee, Y. J. Choi, V. Kiryukhin, and S.-W. Cheong, *Science* 324, 63 (2009).
- 53 T. Kimura, S. Kawamoto, I. Yamada, M. Azuma, M. Takano, and Y. Tokura, *Phys. Rev. B* 67, 180401 (2003).
- 54 A. Kumar, L. W. Martin, S. Denev, J. B. Kortright, Y. Suzuki, R. Ramesh, and V. Gopalan, *Phys. Rev. B* 75, 060101 (2007).
- 55 B. B. Van Aken, T. T. M. Palstra, A. Filippetti, and N. A. Spaldin, *Nat. Mater.* 3, 164 (2004).
- 56 E. J. W. Verwey and P. W. Haayman, *Physica* 8, 979 (1941).
- 57 D. V. Efremov, J. van den Brink, and D. I. Khomskii, *Nat. Mater.* 3, 853 (2004).
- 58 T. Goto, T. Kimura, G. Lawes, A. P. Ramirez, and Y. Tokura, *Phys. Rev. Lett.* 92, 257201 (2004).
- 59 N. Hur, S. Park, P. A. Sharma, J. S. Ahn, S. Guha, and S. W. Cheong, *Nature* 429, 392 (2004).
- 60 T. Kimura, T. Goto, H. Shintani, K. Ishizaka, T. Arima, and Y. Tokura, *Nature* 426, 55 (2003).
- 61 N. A. Hill, *J. Phys. Chem. B* 104, 6694 (2000).
- 62 P. Murugavel, D. Saurel, W. Prellier, C. Simon, and B. Raveau, *Appl. Phys. Lett.* 85, 4424 (2004).
- 63 M. P. Singh, W. Prellier, C. Simon, and B. Raveau, *Appl. Phys. Lett.* 87, 022505 (2005).
- 64 K. Ueda, H. Tabata, and T. Kawai, *Science* 280, 1064 (1998).
- 65 C.-W. Nan, G. Liu, Y. Lin, and H. Chen, *Phys. Rev. Lett.* 94, 197203 (2005).
- 66 N. Cai, C.-W. Nan, J. Zhai, and Y. Lin, *Appl. Phys. Lett.* 84, 3516 (2004).

- 67 G. Srinivasan, E. T. Rasmussen, B. J. Levin, and R. Hayes, *Phys. Rev. B* 65, 134402 (2002).
- 68 H. Zheng, J. Wang, S. E. Lofland, Z. Ma, L. Mohaddes-Ardabili, T. Zhao, L. Salamanca-Riba, S. R. Shinde, S. B. Ogale, F. Bai, D. Viehland, Y. Jia, D. G. Schlom, M. Wuttig, A. Roytburd, and R. Ramesh, *Science* 303, 661 (2004).
- 69 H. N. Lee, H. M. Christen, M. F. Chisholm, C. M. Rouleau, and D. H. Lowndes, *Nature* 433, 395 (2005).
- 70 R. Ramesh and N. A. Spaldin, *Nat. Mater.* 6, 21 (2007).
- 71 U. Ozgur, Y. I. Alivov, C. Liu, A. Teke, M. A. Reshchikov, S. Dogan, V. Avrutin, S. J. Cho, and H. Morkoc, *J. Appl. Phys.* 98, 041301 (2005).
- 72 T. Minami, H. Sato, H. Nanto, and S. Takata, *Jap. J. Appl. Phys. Part 2-Letters* 24, L781 (1985).
- 73 D. C. Look, J. W. Hemsky, and J. R. Sizelove, *Phys. Rev. Lett.* 82, 2552 (1999).
- 74 A. F. Kohan, G. Ceder, D. Morgan, and C. G. Van de Walle, *Phys. Rev. B* 61, 15019 (2000).
- 75 Y. M. Strzhemechny, H. L. Mosbacker, D. C. Look, D. C. Reynolds, C. W. Litton, N. Y. Garces, N. C. Giles, L. E. Halliburton, S. Niki, and L. J. Brillson, *Appl. Phys. Lett.* 84, 2545 (2004).
- 76 K. Ip, M. E. Overberg, Y. W. Heo, D. P. Norton, S. J. Pearton, S. O. Kucheyev, C. Jagadish, J. S. Williams, R. G. Wilson, and J. M. Zavada, *Appl. Phys. Lett.* 81, 3996 (2002).
- 77 S. Myong, S. Baik, C. Lee, W. Cho, and K. Lim, *Jap. J. Appl. Phys. Part 2-Letters* 36, L1078 (1997).
- 78 E.-C. Lee, Y. S. Kim, Y. G. Jin, and K. J. Chang, *Phys. Rev. B* 64, 085120 (2001).
- 79 D. C. Look, D. C. Reynolds, C. W. Litton, R. L. Jones, D. B. Eason, and G. Cantwell, *Appl. Phys. Lett.* 81, 1830 (2002).
- 80 X. Li, Y. Yan, T. A. Gessert, C. L. Perkins, D. Young, C. DeHart, M. Young, and T. J. Coutts, *J. Vac. Sci. Technol., A* 21, 1342 (2003).
- 81 H. S. Kim, S. J. Pearton, D. P. Norton, and F. Ren, *J. Appl. Phys.* 102, 104904 (2007).
- 82 K.-K. Kim, H.-S. Kim, D.-K. Hwang, J.-H. Lim, and S.-J. Park, *Appl. Phys. Lett.* 83, 63 (2003).

- 83 W.-J. Lee, J. Kang, and K. J. Chang, *Phys. Rev. B* 73, 024117 (2006).
- 84 S. Limpijumnong, S. B. Zhang, S.-H. Wei, and C. H. Park, *Phys. Rev. Lett.* 92, 155504 (2004).
- 85 C. Morhain, M. Teisseire, S. Vézian, F. Vigué, F. Raymond, P. Lorenzini, J. Guion, G. Neu, and J. P. Faurie, *Phys. Stat. Sol. (b)* 229, 881 (2002).
- 86 D. J. Chadi, *Phys. Rev. Lett.* 72, 534 (1994).
- 87 S. B. Zhang, S.-H. Wei, and A. Zunger, *J. Appl. Phys.* 83, 3192 (1998).
- 88 A. Zunger, *Appl. Phys. Lett.* 83, 57 (2003).
- 89 Y. I. Alivov, J. E. Van Nostrand, D. C. Look, M. V. Chukichev, and B. M. Ataev, *Appl. Phys. Lett.* 83, 2943 (2003).
- 90 H. Ohta, M. Hirano, K. Nakahara, H. Maruta, T. Tanabe, M. Kamiya, T. Kamiya, and H. Hosono, *Appl. Phys. Lett.* 83, 1029 (2003).
- 91 A. Tsukazaki, A. Ohtomo, T. Onuma, M. Ohtani, T. Makino, M. Sumiya, K. Ohtani, S. F. Chichibu, S. Fuke, Y. Segawa, H. Ohno, H. Koinuma, and M. Kawasaki, *Nat. Mater.* 4, 42 (2005).
- 92 J. H. Lim, C. K. Kang, K. K. Kim, I. K. Park, D. K. Hwang, and S. J. Park, *Advan. Mater.* 18, 2720 (2006).
- 93 J. Navarro, J. Nogués, J. S. Muñoz, and J. Fontcuberta, *Phys. Rev. B* 67, 174416 (2003).
- 94 J. Santiso, A. Figueras, and J. Fraxedas, *Surf. Interf. Anal.* 33, 676 (2002).
- 95 G. H. Bouchard and M. J. Sienko, *Inorg. Chem.* 7, 441 (1968).
- 96 H. J. V. Hook, *J. Phys. Chem.* 68, 3786 (1964).
- 97 J. Hombo, Y. Matsumoto, and T. Kawano, *Journal of Solid State Chemistry* 84, 138 (1990).
- 98 E. Taketani, T. Matsui, N. Fujimura, and K. Morii, *IEEE Trans. Mag.* 40, 2736 (2004).
- 99 J. Navarro, J. Nogués, J. S. Muñoz, and J. Fontcuberta, *Phys. Rev. Lett.* 67, 174416 (2003).
- 100 F. Matsukura, H. Ohno, A. Shen, and Y. Sugawara, *Phys. Rev. B* 57, R2037 (1998).

- 101 J. Kondo, in *Solid State Physics*, edited by David Turnbull Frederick Seitz and Ehrenreich Henry (Academic Press, 1970), Vol. Volume 23, pp. 183.
- 102 A. N. Pasupathy, R. C. Bialczak, J. Martinek, J. E. Grose, L. A. K. Donev, P. L. McEuen, and D. C. Ralph, *Science* 306, 86 (2004).
- 103 J. Zhang, Y. Xu, S. Cao, G. Cao, Y. Zhang, and C. Jing, *Phys. Rev. B* 72, 054410 (2005).
- 104 R. Karplus and J. M. Luttinger, *Phys. Rev.* 95, 1154 (1954).
- 105 W. Eerenstein, N. D. Mathur, and J. F. Scott, *Nature* 442, 759 (2006).
- 106 N. A. Spaldin and M. Fiebig, *Science* 309, 391 (2005).
- 107 S.-W. Cheong and M. Mostovoy, *Nat. Mater.* 6, 13 (2007).
- 108 W. Prellier, M. P. Singh, and P. Murugavel, *J. Phys.: Condens. Matter* 17, R803 (2005).
- 109 D. Khomskii, *Physics* 2, 1 (2009).
- 110 A. Krost, G. Bauer, and J. Woitok, *High Resolution X-Ray Diffraction, Optical Characterization of Epitaxial Semiconductor Layers*. (Springer-Verlag, Berlin ; New York, 1996), pp.xiv.
- 111 A. Grutter, F. Wong, E. Arenholz, M. Liberati, A. Vailionis, and Y. Suzuki, *Appl. Phys. Lett.* 96, 082509 (2010).
- 112 C. Thiele, K. Dörr, O. Bilani, J. Rödel, and L. Schultz, *Phys. Rev. B* 75, 054408 (2007).
- 113 C. L. Canedy, X. W. Li, and G. Xiao, *Phys. Rev. B* 62, 508 (2000).
- 114 P. Murugavel, M. P. Singh, W. Prellier, B. Mercey, C. Simon, and B. Raveau, *J. Appl. Phys.* 97, 103914 (2005).
- 115 R. Ranjith, U. Lüders, and W. Prellier, *J. Phys. Chem. Solids* 71, 1140 (2010).
- 116 M. P. Singh, W. Prellier, L. Mechin, C. Simon, and B. Raveau, *J. Appl. Phys.* 99, 024105 (2006).
- 117 Y. Lu, J. Klein, C. Höfener, B. Wiedenhorst, J. B. Philipp, F. Herbstritt, A. Marx, L. Alff, and R. Gross, *Phys. Rev. B* 62, 15806 (2000).
- 118 M. Izumi, Y. Ogimoto, Y. Okimoto, T. Manako, P. Ahmet, K. Nakajima, T. Chikyow, M. Kawasaki, and Y. Tokura, *Phys. Rev. B* 64, 064429 (2001).
- 119 D. C. Look, *Mater. Sci. Eng. B* 80, 383 (2001).

- 120 D. M. Bagnall, Y. F. Chen, Z. Zhu, T. Yao, S. Koyama, M. Y. Shen, and T. Goto, *Appl. Phys. Lett.* 70, 2230 (1997).
- 121 A. Janotti and C. G. Van de Walle, *Rep. Prog. Phys.* 72, 126501 (2009).
- 122 E. Fortunato, D. Ginley, H. Hosono, and D. C. Paine, *MRS Bulletin* 32, 242 (2007).
- 123 H. Kim, J. S. Horwitz, W. H. Kim, A. J. Mäkinen, Z. H. Kafafi, and D. B. Chrisey, *Thin Solid Films* 420–421, 539 (2002).
- 124 T. Minami, *Semi. Sci. Technol.* 20, S35 (2005).
- 125 K. Nomura, H. Ohta, A. Takagi, T. Kamiya, M. Hirano, and H. Hosono, *Nature* 432, 488 (2004).
- 126 Y. W. Heo, S. J. Park, K. Ip, S. J. Pearton, and D. P. Norton, *Appl. Phys. Lett.* 83, 1128 (2003).
- 127 E. Kumar, J. Chatterjee, N. Rama, N. DasGupta, and M. S. R. Rao, *ACS Appl. Mater. Interfaces* 3, 1974 (2011).
- 128 A. M. Michelle, H. Lee Joon, Z. Bi, and H. Wang, *J. Phys.: Condens. Matter* 24, 229501 (2012).
- 129 M. A. Thomas and J. B. Cui, *J. Phys.Chem. Lett.* 1, 1090 (2010).
- 130 W. Liu, F. Xiu, K. Sun, Y.-H. Xie, K. L. Wang, Y. Wang, J. Zou, Z. Yang, and J. Liu, *J. Am. Chem. Soc.* 132, 2498 (2010).
- 131 B. Chavillon, L. Cario, A. Renaud, F. Tessier, F. Cheviré, M. Boujtita, Y. Pellegrin, E. Blart, A. Smeigh, L. Hammarström, F. Odobel, and S. Jobic, *J. Am. Chem. Soc.* 134, 464 (2012).
- 132 H. D. Cho, A. S. Zakirov, S. U. Yuldashev, C. W. Ahn, Y. K. Yeo, and T. W. Kang, *Nanotechnology* 23, 115401 (2012).
- 133 J. Lee, S. Cha, J. Kim, H. Nam, S. Lee, W. Ko, K. L. Wang, J. Park, and J. Hong, *Advan. Mater.* 23, 4183 (2011).
- 134 H. S. Kim, F. Lugo, S. J. Pearton, D. P. Norton, Y.-L. Wang, and F. Ren, *Appl. Phys. Lett.* 92, 112108 (2008).
- 135 M.-T. Chen, M.-P. Lu, Y.-J. Wu, J. Song, C.-Y. Lee, M.-Y. Lu, Y.-C. Chang, L.-J. Chou, Z. L. Wang, and L.-J. Chen, *Nano Lett.* 10, 4387 (2010).
- 136 V. Avrutin, D. J. Silversmith, and H. Morkoc, *Proc. IEEE* 98, 1269 (2010).
- 137 M. D. McCluskey and S. J. Jokela, *J. Appl. Phys.* 106, 071101 (2009).

BIOGRAPHICAL SKETCH

After graduating from Susung High School in 1996, Kyeong-Won Kim attended Seoul National University. He received his Bachelor of Science and Master of Science in materials science and engineering in 2000 and 2002, respectively. During the master's studies, he conducted research on sintering and microstructure of lead zirconate titanate ceramics under the supervision of Dr. Doh-Yeon Kim. And then he joined Republic of Korea Air Force in 2003. After finishing three year service as a maintenance officer in 2006, he worked for LG Electronics Institute of Technology, where he conducted research on thin film solar cells. He chose to pursue his doctoral degree. He began his graduate studies at University of Florida in 2007 and also joined Dr. David Norton's research group. He received his Ph.D. from the University of Florida in the summer of 2012. His research interests include the synthesis of oxide thin films and heterostructures and doping in ZnO thin films for novel applications in electronics and photonics. When not in the lab, he enjoys reading, running, and playing and watching ball games.